# Thermoelectric Properties and Stability of Barium Copper Chalcogenides

by

Parisa Jafarzadeh

A thesis
presented to the University of Waterloo
in fulfillment of the
thesis requirement for the degree of
Doctor of Philosophy
in
Chemistry

Waterloo, Ontario, Canada, 2019

# Examining Committee Membership

The following served on the Examining Committee for this thesis. The decision of the Examining Committee is by majority vote.

| | |
|---|---|
| External Examiner | Venkataraman Thangadurai<br>Professor University of Calgary |
| Supervisor(s) | Holger Kleinke<br>Professor Chemistry |
| Internal Member | Germán Sciaini<br>Associate Professor Chemistry |
| | Eric Prouzet<br>Associate Professor Chemistry |
| Internal-external Member | Michael Pope<br>Assistant Professor Chemical Engineering |
| Other Member(s) | Kathryn Preuss<br>Professor University of Guelph |

# AUTHOR'S DECLARATION

I hereby declare that I am the sole author of this thesis. This is a true copy of the thesis, including any required final revisions, as accepted by my examiners.

I understand that my thesis may be made electronically available to the public.

# Abstract

The objective of this thesis was to study the thermoelectric properties of copper chalcogenide-based materials with mixed chalcogen atom sites. Herein, the effect of different concentrations of chalcogen atoms on the physical property measurements and the performance of the thermoelectric materials with two different crystal structures were investigated. In addition, stability studies of two materials with different chalcogen atoms (S and Se) surprisingly revealed substantially different behavior.

Due to the stability issues as a consequence of Cu ion conductivity at elevated temperatures, the thermoelectric application of $Cu_{2-x}S$ and $\beta$-$Cu_{2-x}Se$ is restricted at these temperatures. Taking that into consideration, quaternary copper chalcogenides with additional large atoms, Ba and Te, were synthesized. The quaternary barium copper selenide- tellurides, $Ba_3Cu_{16-x}Se_{11-y}Te_y$, were synthesized with different x and y values by a melting and slow cooling process. Measurement of the thermoelectric properties revealed changes during repeated measurements of the same samples. Further investigations including single crystal studies after the measurements proved that this is likely a consequence of Cu ion conductivity in these materials. The reproducibility of the data was investigated by varying the maximum temperature as well as the current density. As a result, decreasing the maximum temperature and current density led to full stability. Finally, their figure-of-merit, $zT$, only reached a maximum value of 0.49 at 690 K.

Furthermore, thermoelectric properties of the barium copper sulfide-tellurides, $Ba_3Cu_{16-x}S_{11-y}Te_y$, were studied. Among three different studied compositions, hot-pressed $Ba_3Cu_{15.3}S_{7.5}Te_{3.5}$ has the highest power factor, 4.6 $\mu$W cm$^{-1}$K$^{-2}$, which is almost 50% higher than that of the best cold-pressed sample, $Ba_3Cu_{16}S_9Te_2$ with 2.4 $\mu$W cm$^{-1}$K$^{-2}$ at 700 K. These quaternary sulfide-tellurides are bestowed with an extraordinarily low total thermal conductivity, which is below 0.6 W m$^{-1}$K$^{-1}$ throughout the entire studied temperature range. In contrast to the selenides, the sulfides are stable under the applied measurement conditions. In addition, their higher stability at elevated temperatures compared to $Cu_2S$ and $\beta$-$Cu_2Se$ with high *zT* values renders them more feasible for thermoelectric devices. Among the three studied materials, the one with the highest Te content, $Ba_3Cu_{15.3}S_{7.5}Te_{3.5}$, exhibited the lowest thermal conductivity and the highest electrical conductivity, which resulted in *zT* = 0.88 at 745 K. This *zT* value is also almost two times larger than the *zT* of $Ba_3Cu_{16-x}Se_{11-y}Te_y$.

The quaternary barium copper selenide-tellurides, $BaCu_{6-x}Se_{1-y}Te_{6+y}$ have been reported earlier to be *p*-type semiconductors, when x = 0.1 and y = 0. Here, we studied the properties after varying the Cu and the Se/Te concentrations. At first, materials with the same nominal Cu concentration, 5.9 Cu per formula unit, and different Se/Te ratios were prepared. The different thermoelectric properties indicated that the Se/Te ratio strongly affected the Cu deficiency, which is directly responsible for the charge carrier concentration. Single crystal structure data revealed the Cu amount to be less than 5.8 per formula unit when y = 0.4; therefore, a sample of nominal composition "$BaCu_{5.74}Se_{0.46}Te_{6.54}$" was also studied. This sample exhibited an electrical conductivity of 685 $\Omega^{-1}$cm$^{-1}$ at room temperature, which is

almost three times larger than in case of "$BaCu_{5.9}SeTe_6$", in accord with the lower Cu amount causing a larger hole concentration. The larger mass fluctuation on the Se/Te site resulted in a lower lattice thermal conductivity, but the decreased Seebeck coefficient mitigated a performance increase in form of a higher figure-of-merit. In contrast to the binary Cu chalcogenides, $Cu_{2-x}S$ and $\beta$-$Cu_{2-x}Se$, the data are stable under the measurement conditions.

# Acknowledgements

Foremost, I would like to express my sincere gratitude to my supervisor, Dr. Holger Kleinke. Not only did he guide me throughout my PhD to become a better scientist, but he also helped me develop as a human being. The most valuable thing I learned from him was to keep learning no matter what stage you are at, and to explore novel things every day. He also showed me that sometimes a little push is all you need to get back on track. I hope I can be like this in the future, and pass forth this acquired knowledge to others.

I would like to express my sincere gratitude to my parents and my sister for helping me to follow my dreams, even when they take me miles away from home. I also want to express my deep appreciation to the love of my life, Mathew VanZant. Thank you for all your help, support and patience through my PhD; and also for helping with my thesis.

I would like to thank my PhD advisory committee members, Dr. Germán Sciaini, and Dr. Kathryn Preuss for all their guidance duing my committee meetings. In particular, I would like to give a special thanks to my committee member Dr. Eric Prouzet. Thank you for all your help and support through my PhD; I learned a lot from you. I also want to thank my examiners, Dr. Venkataraman Thangadurai and Dr. Michael Pope for their time.

I would like to thank former colleagues, Katja Kleinke, Maegan Rodrigues, Dr. Mohamed Oudah, Dr. Nader Farahi, Mathew VanZant, Dr. Nhi Truong, Dr. Quansheng Guo, Dr. Nagaraj Nandihalli, Rafay Shams, and Xiaoyu Cheng; in addition to my current colleagues, Luke Menezes, Yixuan Shi, Dr. Leilane Macario, Daniel Ramirez, and Cheryl Sturm.

I would like to give a special thanks to our crystallographer, Dr. Abdeljalil Assoud, my former committee member Dr. Richard Oakley, and our great collaborators, Dr. Eckhard Müller from German Aerospace Center (DLR), Dr. Jan Kycia and Tianze Zou from Department of Physics & Astronomy at the University of Waterloo.

# Table of Contents

# List of Figures

# List of Tables

# List of Symbols and Abbreviations

## Symbols

| | |
|---|---|
| $\upsilon$ | average phonon velocity |
| $\overline{m}$ | average atomic mass |
| $\overline{ZT}$ | average figure-of-merit of the device |
| $\delta$ | atomic distances |
| $k_B$ | Boltzmann constant |
| $n$ | carrier concentration; number of the used reflections |
| $Q$ | carried heat by charges; mixed chalcogen atom site |
| $F_c$ | calculated structure factor |
| $J$ | current density |
| $I$ | electrical current |
| $l_e$ | electron mean free path for electrical conductivity |
| $l_t$ | electron mean free path for thermal conductivity |
| $zT$ | dimensionless figure-of-merit of the thermoelement |
| $m^*$ | density of states effective mass |
| $\rho_l$ | density of liquid |
| $\sigma$ | electrical conductivity |
| $\kappa_e$ | electronic thermal conductivity |
| $e$ | elementary charge |
| $E_F$ | Fermi energy |
| $f_i$ | fractional concentration of impurity mass |
| $\gamma$ | Grüneisen parameter |
| $C_V$ | heat capacity |
| $C_p$ | heat capacity |
| $V_H$ | Hall voltage |
| $R_H$ | Hall coefficient |

| | |
|---|---|
| $M_i$ | impurity mass |
| $R_{int}$ | internal residual value |
| $\kappa_L$ | lattice thermal conductivity |
| $L$ | Lorenz number; Lorentz effect; Lorentz force |
| $Lp$ | Lorentz-polarization factor |
| $\eta_{max}$ | maximum efficiency of a thermoelectric power generator |
| $\varphi_{max}$ | maximum efficiency of a thermoelectric refrigerator |
| $zT_{max}$ | maximum dimensionless figure-of-merit |
| $T_{max}$ | maximum measured temperature |
| $B$ | magnetic field |
| $\mu$ | mobility |
| $T_m$ | melting point |
| $T_H$ | mean temperature at the hot end |
| $T_C$ | mean temperature at the cold end |
| $N_{atom}$ | number of atoms per unit cell |
| $F_o$ | observed structure factor |
| $\pi$ | Peltier effect |
| $l$ | phonon mean free path |
| $p$ | polarization effect; number of refined parameters |
| $R$ | resistance |
| $\alpha$ | Seebeck coefficient |
| $\Gamma$ | strength of the phonon scattering |
| $F_{hkl}$ | scaling factor |
| $\lambda$ | thermal diffusivity; wavelength |
| $\tau$ | relaxation time |
| $\kappa$ | thermal conductivity |
| $T$ | absolute temperature |
| $\Delta T$ | temperature gradient |
| $\Delta V$ | voltage difference |

# Abbreviations

| | |
|---|---|
| ADP | atomic displacement parameter |
| BSE | back scattered electrons |
| CCD | charge-coupled device |
| DFT | density functional theory |
| DOS | density of states |
| DSC | differential scanning calorimetry |
| EDX | energy dispersive X-ray analysis |
| GOF | goodness of fit |
| HP | hot-pressing |
| IR | infrared |
| LAST | lead antimony silver telluride |
| MWCNT | multi-wall carbon nanotubes |
| PGEC | phonon-glass electron-crystal |
| PLEC | phonon-liquid electron-crystal |
| PF | power factor |
| PXRD | powder X-ray diffraction |
| PSM | potential-Seebeck-microprobe |
| RTG | radioisotope thermoelectric generator |
| SEM | scanning electron microscopy |
| SPS | spark plasma sintering |
| SE-MS-SPS | single-element - melt-spinning - spark-plasma-sintering |
| SPB | single parabolic band |
| SE | secondary electrons |
| TG | thermal gravimetry |
| XRD | X-ray diffraction |

# 1. Introduction

## 1.1 Thermoelectric Phenomena

In todays' society, energy plays a vital role as it is a necessity for everyday life. Fossil fuels are a natural resource that our society is heavily dependent on for energy production. However, more than half of the energy manufactured is wasted as heat. Also, fossil fuels are non-renewable and their cost is ever-increasing due to their depletion.[1] Therefore, converting this heat into useful energy with inexpensive materials could prove to be very beneficial to society. Thermoelectric materials can help solve this issue as they can directly generate useful electricity from waste heat.

One fundamental aspect of thermoelectrics is the Seebeck effect. In 1821 Thomas Seebeck noticed a deviation in a compass needle in a loop with a temperature difference between the two dissimilar materials in vicinity of it. Although he falsely related this phenomenon to the magnetism at the beginning, he studied this effect in a multiple number of materials, *i.e.* metals and semiconductors later on. This so-called Seebeck effect is in essence the fundamental of thermoelectrics, which has been used in thermoelectric series to generate electricity from heat for several decades.[2] The Seebeck coefficient ($\alpha$) is the voltage difference ($\Delta V$) caused by an applied temperature gradient ($\Delta T$) at a thermoelectric junction (Equation 1.1). The automotive industry intends to use this effect by converting waste heat generated from gasoline engines into useful energy.[3–6] Dongfeng Trucks,[7] Gentherm Incorporated,[8]

SANGO Co., Ltd.,[9] Tenneco Inc.,[10] and Valeo[11] are examples of companies that have tested thermoelectric devices in the automotive industry. The Seebeck effect has also been proven to be useful in the space industry.[6,12] For example, by utilizing the Radioisotope Thermoelectric Generators (RTG) in missions such as Apollo, Viking and Voyager, the heat caused by the natural decay of Plutonium-238 was successfully converted into electricity.[12]

$$\alpha = \frac{\Delta V}{\Delta T} \tag{1.1}$$

The opposite effect of the Seebeck, with the application in cooling systems, is called the Peltier effect. Almost a decade after the discovery of the Seebeck effect, Peltier discovered that the difference in voltage at a thermoelectric junction would result in a temperature difference at that junction. This in fact is a result of the generation or absorption of heat while the current is passing the junction of two different materials. The Peltier effect, $\pi$, is computed from Equation 1.2, where $Q$ is the heat carried by charges and $I$ is the current across the junction. Few examples of the commercialized applications of Peltier effect include car seats, coolers and referigerators.[13] Companies such as European Thermodynamics[14] and II-VI Marlow[15] have utilized the Peltier effect in some of their products.

$$\pi = \frac{Q}{I} \tag{1.2}$$

In 1851, Lord Kelvin (William Thomson) correlated the Seebeck and Peltier effect

thermodynamically. In this effect which is known as the Thomson effect, the absorption or production of heat is explained based on the direction of the passing current to the thermal gradient (Equation 1.3).[2] In order, $\alpha$, $\pi$, and $T$ are the Seebeck coefficient, the Peltier effect, and the absolute temperature in this equation.

$$\alpha = \frac{\pi}{T} \tag{1.3}$$

## 1.2 Thermoelectric Efficiency and Dimensionless Figure-of-Merit

The dimensionless figure-of-merit, $zT$, of a thermoelectric material is defined in Equation 1.4.[16]

$$zT = \frac{\alpha^2 \sigma}{\kappa} T \tag{1.4}$$

In the equation above, thermal conductivity, $\kappa$, is inversely related to the figure-of-merit. The power factor of a thermoelectric material, $\alpha^2\sigma$, is the product of the square of the Seebeck coefficient, $\alpha$, and electrical conductivity, $\sigma$, and thereby a measure for the electrical performance of the thermoelectric material.

The power generator[6] and the cooling refrigerator's maximum efficiency[17] denoted as $\eta_{max}$ and $\varphi_{max}$ respectively, are shown in Equation 1.5 and Equation 1.6.

$$\eta_{\max} = \frac{T_H - T_C}{T_H} \frac{\sqrt{1+\overline{ZT}}-1}{\sqrt{1+\overline{ZT}}+\frac{T_C}{T_H}} \quad (1.5)$$

$$\varphi_{\max} = \frac{T_C}{T_H - T_C} \frac{\sqrt{1+\overline{ZT}}-\frac{T_H}{T_C}}{\sqrt{1+\overline{ZT}}+1} \quad (1.6)$$

In both equations, $\overline{ZT}$ is the average figure-of-merit of the device, which is at best the average of the $zT$ values of the *p*-type and *n*-type materials, averaged over the applied temperature range. In order, $T_H$ and $T_C$ refer to the mean temperature at the hot end and the cold end. Thus, improving the $zT$ values of the thermoelectric materials is one of the most important areas of thermoelectric studies. Indeed, this is very challenging as all the parameters which define the material's $zT$ are interrelated.

## 1.3 Thermoelectric Properties Interdependence

In order for a material to achieve larger $zT$ values, the electrical conductivity and the Seebeck coefficient should increase, and the thermal conductivity should decrease. However, optimizing one parameter typically precludes the optimization of others.

Excluding lattice thermal conductivity, $\kappa_L$, the rest of the thermoelectric key properties are related to the charge carrier density or charge carrier concentration, *n*, which is expressed in Equations 1.7 to 1.10.

$$\sigma = n\, e\, \mu \quad (1.7)$$

$$\kappa = \kappa_L + \kappa_e \quad (1.8)$$

$$\kappa_e = L_0 \, \sigma T \quad (1.9)$$

$$\kappa = \kappa_L + L_0 \, n \, e \, \mu \, T \quad (1.10)$$

Where $\sigma$ is the electrical conductivity, $e$ is the elementary charge ($1.602 \times 10^{-19}$ C), $n$ is the carrier concentration and $\mu$ is the charge carrier mobility. In order, $\kappa$, $\kappa_L$ and $\kappa_e$ are thermal conductivity, lattice thermal conductivity and electronic thermal conductivity. In the equations above, $T$ is the absolute temperature and $L_0$ is the Lorenz number. Equation 1.9 is known as the Wiedemann-Franz relation.[18] Based on the equations above, increasing $n$ causes $\sigma$ and $\kappa$ to increase. In order for a material to be considered as an effective thermoelectric, the carrier concentration should range between $10^{19}$ $cm^{-3}$ - $10^{21}$ $cm^{-3}$ (typical heavily doped semiconductors).[19] Tuning carrier concentration *via* doping a compound with electron donors or acceptors is the most popular way to effectively optimize $n$ in that compound.

The number of the available states that could be occupied by electrons at each energy level in a material is known as density of states (*DOS*). Electrical conductivity increases proportionally to the available density of states near the Fermi level, *DOS*(*E*) (Equation 1.11). On the other hand, the Seebeck coefficient is directly related to the first derivative of *DOS*(*E*), and inversely proportional to *DOS*(*E*) (Equation 1.12).[20]

$$\sigma \propto DOS(E)|_{E = E_F} \quad (1.11)$$

$$\alpha \propto \frac{1}{DOS(E)} \frac{dDOS(E)}{dE}\Big|_{E=E_F} \quad (1.12)$$

Therefore, a large *DOS* at the Fermi level with a positive impact on the electrical transport properties would potentially enhance the efficiency of the thermoelectric material. In general, a material that possesses a band structure with concurrent flat bands (larger effective mass and larger $\alpha$) and parabolic bands (larger electron mobility, larger $\sigma$) are the most ideal for thermoelectric performance. In most thermoelectric materials with complexity in their band structures, high *DOS*(*E*) does not occur with a high electrical conductivity at the same time. In contrast, a large Seebeck coefficient attributed to a large number of spikes close to the Fermi level is expected. In addition, high complexity of the crystal structure and the band structure is favorable for the material to achieve a low thermal conductivity.

According to the Equation 1.8, the thermal conductivity of a thermoelectric material is a sum of the electronic, $\kappa_e$, and the lattice, $\kappa_L$, thermal conductivity. The contribution of the electronic thermal conductivity to the thermal conductivity in heavily doped semiconductors with a large number of charge carriers is noteworthy. This in part affects the thermoelectric properties adversely.

The ratio of $\kappa/(\sigma T)$, known as Lorenz number, *L*, was first calculated theoretically by Drude; applying the ideal gas law in Equation 1.13.

$$\kappa = \frac{1}{3} l v C_V = \frac{1}{3} v^2 \tau C_V \qquad (1.13)$$

Where $l$ is the phonon mean free path, $v$ is the average phonon velocity and $C_V$ is the volume heat capacity. The phonon mean free path is a product of $\tau$, the relaxation time, and $v$. Finally, Drude found the ratio of $\kappa/\sigma$ based on the assumptions for the kinetic energy and the heat capacity calculated from the kinetic energy ($\frac{1}{2} m v^2 = \frac{3}{2} k_B T$) and heat capacity ($\frac{3}{2} k_B n$) with $n$ being number of the electrons per unit volume (Equation 1.14).[21]

$$\frac{\kappa}{\sigma T} = \frac{\frac{1}{3} C_V m v^2}{n e^2 T} = L = \frac{3}{2}\left(\frac{k_B}{e}\right)^2 = 1.11 \times 10^{-8}\ \mathrm{W\Omega\ K^{-2}} \qquad (1.14)$$

The $L$ value from Drude's model is calculated as $1.11 \times 10^{-8}$ WΩ K$^{-2}$. However, this is less than half of the accepted value used nowadays. Based on the Fermi-Dirac statistics for a free electron, $L$ is calculated as per Equation 1.15; which was initially presented by Sommerfeld.[22]

$$L_0 = \frac{\pi^2}{3}\left(\frac{k_B}{e}\right)^2 = 2.44 \times 10^{-8}\ \mathrm{W\Omega\ K^{-2}} \qquad (1.15)$$

Here, the applied heat capacity is lower than the heat capacity of the ideal gas in Drude's calculation by a factor of $\frac{\pi^2}{3}\left(\frac{k_B}{E_F} T\right)$, as it is shown in (Equation 1.16).

$$C_V = \frac{\pi^2}{2}\left(\frac{k_B}{E_F}T\right)nk_B \qquad (1.16)$$

In addition, equation 1.15 is based on the corrected estimation of the classical mean square velocity, $\upsilon$, by a factor of $E_F/k_BT$.

The Lorenz number is expressed as $L_0$ if the electrons are highly degenerate, which typically occurs at very low temperatures in metals. However, depending on the type of scattering mechanisms in electrical and thermal conductions, $L$ might become smaller or larger than $L_0$. At lower temperatures, the electron mean free path is equal for electrical and thermal conductivity, $l_e$ and $l_t$, respectively. These values are equal because only elastic scattering occurs at low temperatures. As a result, $L = L_0 = 2.44 \times 10^{-8}$ WΩ K$^{-2}$ in Equation 1.17.

$$L = L_0\left(\frac{l_t}{l_e}\right)^2 \qquad (1.17)$$

At higher temperatures where the scattering process is inelastic, $l_t \neq l_e$ and therefore $L \neq L_0$.[23] Similar to metals and alloys, deviations from $L_0$ in heavily doped semiconductors mainly depend on the temperature of the temperature dependent scattering mechanisms, and the level of doping. The value of $L$ for semiconductors is in the range of $1.50 \times 10^{-8}$ WΩ K$^{-2}$ (non-degenerate limit) and $2.44 \times 10^{-8}$ WΩ K$^{-2}$ (Sommerfeld value; degenerate limit).

## 1.4 Strategies to Reduce the Lattice Thermal Conductivity

Lattice thermal conductivity can be decreased in several ways. According to the theory proposed by Slack,[24] which relates $\kappa_L$ to crystallographic results, Equation 1.18 is deduced.

$$\kappa_L \propto \frac{\sqrt[3]{T_m}\,\delta^4}{\sqrt{\bar{m}}\,\gamma^2 (N_{atom})^{2/3}} \qquad (1.18)$$

Based on the Equation 1.18, low melting point ($T_m$), short atomic distances ($\delta$), large average masses ($\bar{m}$) and a large number of atoms per unit cell ($N_{atom}$) could assertively suppress the lattice thermal conductivity. In this equation, $\gamma$ is the Grüneisen parameter, which relates the phonon frequency to volume variation in crystals.[25] In general, most efforts to reduce $\kappa_L$ involve shortening the phonon mean free path. As such, any mechanism of scattering, which affects phonons more than electrons, would decrease $\kappa_L$ more than the electrical conductivity. The term PGEC (Phonon-Glass Electron-Crystal) refers to an ideal thermoelectric material, which behaves as glass towards phonons and behaves as crystal with respect to electrons.[26] To follow up with this concept and according to Equation 1.18, some of the approaches to achieve a low $\kappa_L$ are listed as follows: utilization of materials with the rattling effect, large mass fluctuations, heavier atoms, complex crystal structures, larger lattice defects and fine-grained materials for scattering phonons through grain boundaries. Moreover, the extension of PGEC, so-called PLEC (Phonon-Liquid Electron-Crystal) which is a result of eliminating all vibrational modes, has an outstanding impact on minimizing $\kappa_L$.[27]

### 1.4.1 Rattling Effect

Type I inorganic clathrates and filled skutterudites are well-known for their low lattice thermal conductivity due to the rattling motion of atoms inside cage-like structures. This is referred to as the rattling effect. This in turn leads to high thermoelectric performance of these materials at elevated temperatures.[28,29]

Type I clathrates with the general formula of $A_8E_{46}$ ($A$ = group I or II elements, $E$ = group XIII and XIV elements) are classified as Zintl compounds.[30] The structure of these compounds is composed of a cage-like framework formed by covalent bonding of the host atoms, which is filled with a non-bonded ionic so-called "rattling" guest atom.[31] The rattling atom with a large anisotropic atomic displacement parameter (ADP), scatters the phonons and lowers $\kappa_L$ accordingly.[32] The crystal structure of cubic $Ba_8Ga_{16}Si_{30}$ is displayed in Figure 1.1.

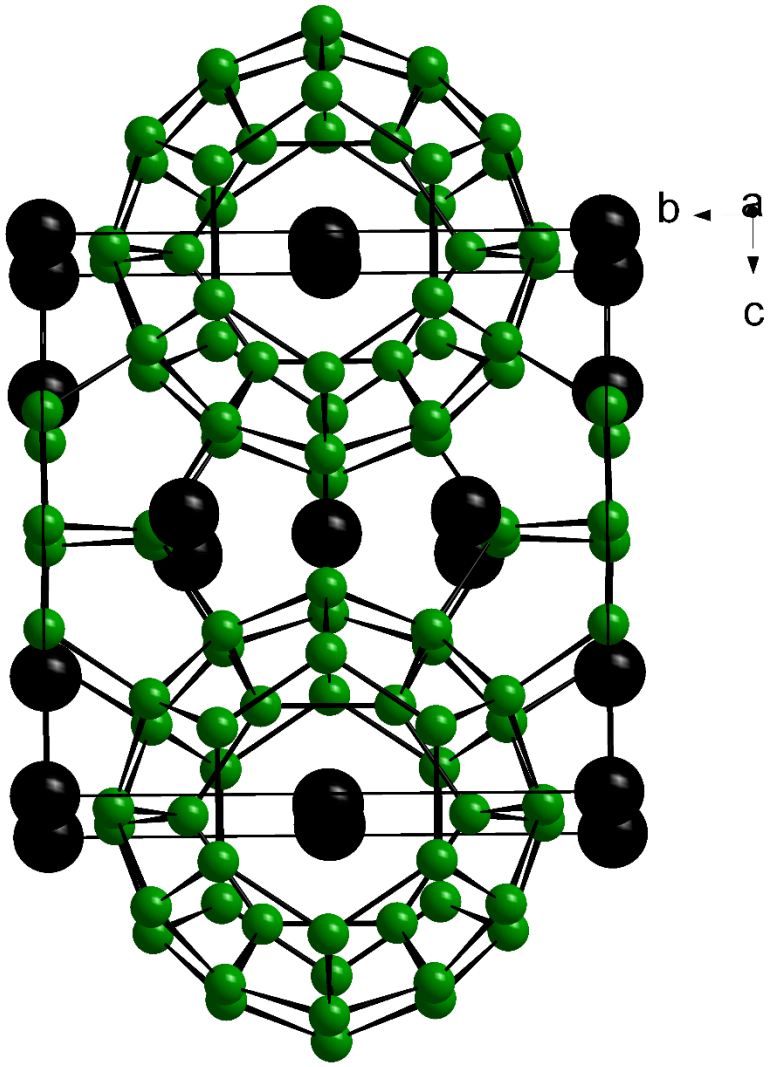


Figure 1.1 Crystal structure of $Ba_8Ga_{16}Si_{30}$. Space group: cubic $Pm\bar{3}n$.

Ba atoms are in black, Ga/Si atoms are in green.[33]

Two types of cages, pentagonal dodecahedra and tetrakaidecahedra, can be found in clathrates I (Figure 1.2). The pentagonal dodecahedral cage contains the atom *A*1 while the

larger tetrakaidecahedron with two hexagonal and twelve pentagonal faces includes the atom *A*2. Hence, *A*1 and *A*2 possess very large coordination numbers of 22 and 24, respectively.

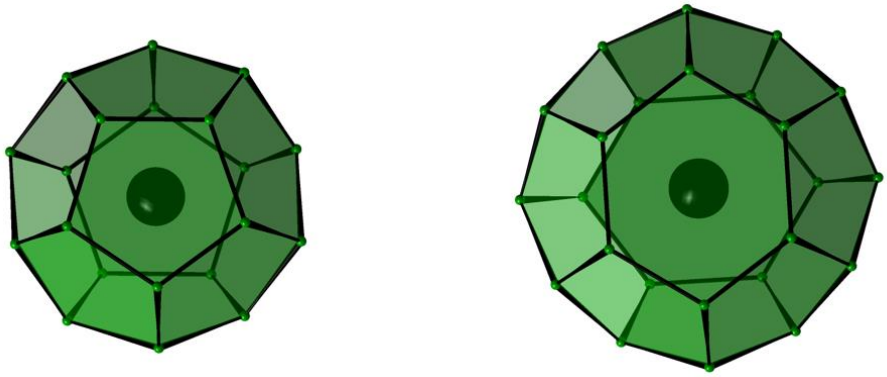

Figure 1.2 Ba1-centered dodecahedron (left), Ba2-centered tetrakaidecahedron (right).

Ga/Si atoms are in green.

The electropositive atom, *A*, donates valence electrons to the *E* atoms. The *A* and *E* atoms are also referred to as the "guest atoms" and the "host atoms" respectively. In this structure, each *E* atom is connected to another four *E* atoms in a three-dimensional anionic framework.[34] Valence-balanced semiconducting clathrates such as $Ba_8Ga_{16}(Si,Ge)_{30}$ contain 184 total valence electrons, which are assigned to the host atoms. Since mixed occupied sites of *E* = Ga/(Si,Ge) are present in these structures, the reduced formal balance for all of the *E* anions is one per bond; allowing a valence balanced formula to be achieved.[30] Clathrates contain free charge carriers as a consequence of valence-imbalance. By varying the concentration of the host atoms, these materials can adopt different properties. For example, $Ba_8Ga_{16-x}Ge_{30+x}$ behaves as a *p*-type semiconductor when $x > 0$ and *n*-type when $x < 0$. The

experimentally obtained lattice thermal conductivity of both *n*-type and *p*-type materials is ~ 1.0 W $m^{-1}K^{-1}$.[35] As mentioned earlier, the relatively low thermal conductivity of clathrates is a consequence of the rattling guest atom, thereby the heat-carrying phonons interact with the vibrational modes of the rattling atoms to lower the lattice thermal conductivity to around that of the glass-like thermal conductivity.[36,37]

Skutterudites, another example of materials with rattling atoms, crystallize in a cubic $ReO_3$-related crystal structure with a space group of $Im\bar{3}$. In contrast to $ReO_3$, the $MQ_3$ (*M* = transition metals of groups 8 - 10 and *Q* = pnicogen atoms) octahedra are tilted. As a result of the existence of the distorted octahedra, skutterudites are comprised of planar $Q_4$ units and two $Q_{12}$ icosahedra in one unit cell.[34] These $Q_{12}$ icosahedra could be treated similar to the host cages in clathrates. In the filled skutterudites, these polyhedra may be either filled with alkaline or rare earth elements. The filled skutterudites with the general formula of $RM'_xM_{4-x}Q_{12}$ (*R* = rare earth group,) have a low thermal conductivity due to the existence of the rattling atoms *R*. The crystal structure of the first filled antimonide skutterudite ($LaFe_4Sb_{12}$) and the $LaSb_{12}$ icosahedron are depicted in Figure 1.3.

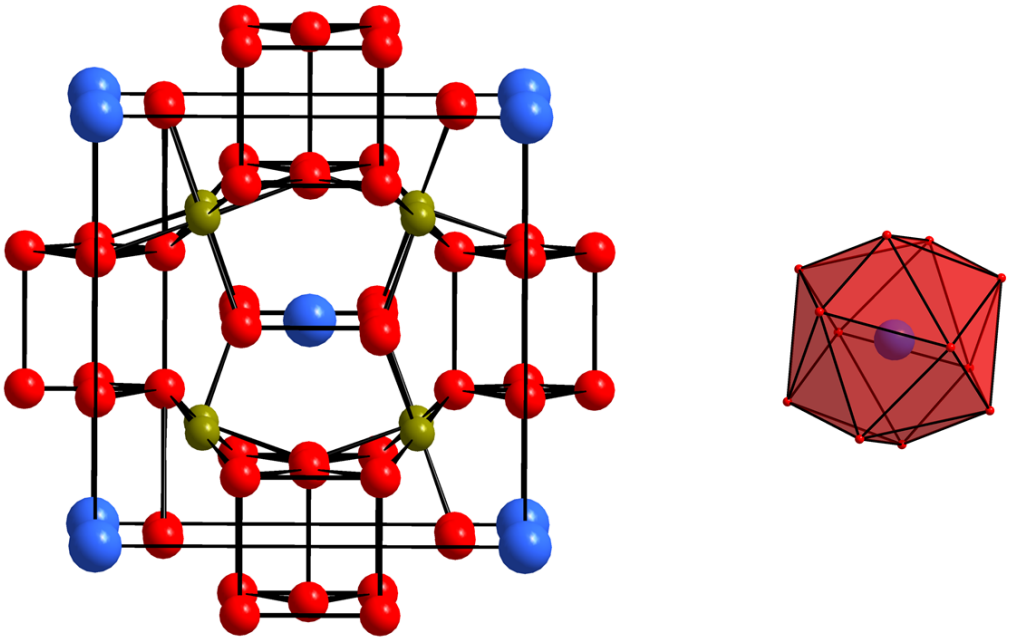

Figure 1.3 Crystal structure of cubic $LaFe_4Sb_{12}$. Space group: cubic $Im\bar{3}$. (La = blue, Fe = green and Sb = red) (left), $LaSb_{12}$ icosahedron (right).[38]

### 1.4.2 Materials with Complex Structures

Materials with complex crystal structures have smaller phonon mean free paths, and lower lattice thermal conductivity values. In addition, a low mobility of the charge carriers leads to a smaller electrical conductivity of these materials.[31,34]

$\beta$-$Zn_4Sb_3$ crystallizes in a rhombohedral crystal structure (space group $R\bar{3}c$). This structure is composed of $ZnSb_4$ tetrahedral units. It is also composed of linear chains of Sb atoms with distances of 2.82 Å and 3.38 Å. The occupancies of three out of four Zn sites, were refined as 4% - 6%; and the occupancy factor of the remaining Zn site was refined as 90%

(also deficient). Therefore, the formula was refined as $Zn_{3.83}Sb_3$.[39] Since Sb atoms are in the form of isolated anions ($Sb^{3-}$) and pairs ($Sb_4^{2-}$), using the Zn site with the largest occupancy, namely Zn1, and ignoring the three other Zn deficient sites, the crystallographic formula $(Zn1)_6(Sb1)_3(Sb2)_2$ is deduced. Therefore, the charge-balanced formula based on the assigned charges is $(Zn^{2+})_{6.5}(Sb^{3-})_3(Sb)_2^{4-}$ for $Zn_{3.9}Sb_3$. Thus, the refined formula of $Zn_{3.83}Sb_3$ is Zn-deficient. As a result, $\beta$-$Zn_4Sb_3$ with a band gap of 0.3 – 0.4 eV is a *p*-type semiconductor.[40,41] A very low lattice thermal conductivity of 0.65 W $m^{-1}K^{-1}$ at room temperature could be mainly attributed to a complex structure as well as the presence of many disordered Zn sites and vibrations within the Sb atom chains.[39,42] A *zT* of 1.3 at 670 K was attained mostly because this material possesses low thermal conductivity.[43,44]

$Yb_{14}MnSb_{11}$ is another example of a material with complexity in its crystal structure. This compound crystallizes in a $Ca_{14}AlSb_{11}$ type structure (space group *I*41/*acd*).[45] This structure is composed of $MnSb_4$ tetrahedral units and a linear $Sb_3^{7-}$ unit with a single bond distance of 3.20 Å between Sb atoms (Figure 1.4). A low thermal conductivity of 0.9 - 0.7 W $m^{-1}K^{-1}$ in a temperature range of 300 K – 1275 K allows this material to perform well at elevated temperatures with a peak *zT* of 1.1 at 1275 K.[46]

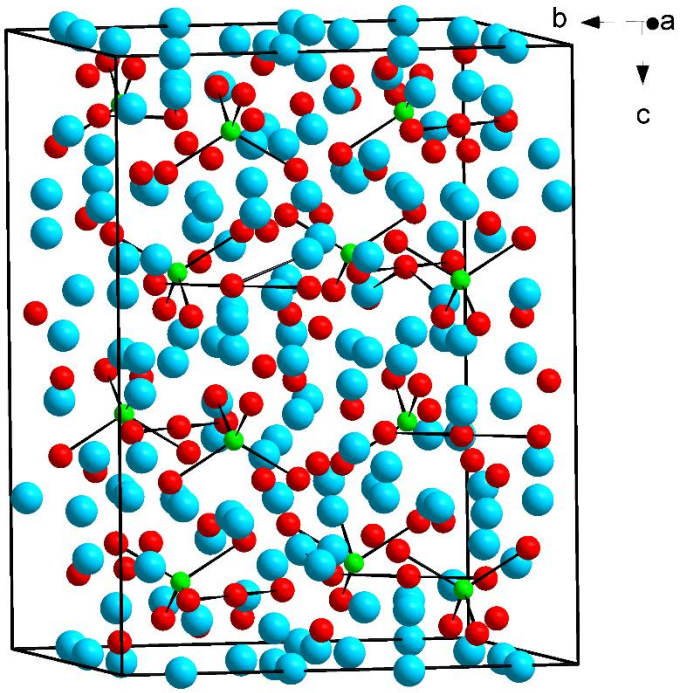


Figure 1.4 Crystal structure of $Yb_{14}MnSb_{11}$. Space group: *I*41/*acd*. Yb atoms are in blue, Mn atoms are in green, and Sb atoms are in red. Only Mn–Sb and Sb–Sb bonds are shown.[45]

### 1.4.3 Heavy Element Containing Materials

Two of the most famous conventional bulk thermoelectric materials used in thermoelectric industries are lead telluride (PbTe) and bismuth telluride ($Bi_2Te_3$). PbTe crystallizes in the simple cubic rock salt structure. Undoped PbTe with a band gap of 0.32 eV and melting point of 1197 K at 300 K serves as a typical semiconductor.[47] According to Equation 1.18, a low lattice thermal conductivity of ~ 2.0 W $m^{-1}K^{-1}$ can be explained by a large average mass of 167.4 g $mol^{-1}$ for this material. Therefore, carrier concentration optimization through one of the commonly used methods, doping, in conjunction with the

relatively low $\kappa_L$ led to a large $zT$. Hence, the *n*-type $PbTe_{1-x}I_x$ and *p*-type $Na_xPb_{1-x}Te$ revealed a $zT$ value of 1.4 at 750 K.[48,49] The isostructural PbSe also performs as an outstanding thermoelectric material at elevated temperatures. This again is in part a result of the surprisingly low $\kappa_L$ of PbSe, which resulted in a $zT$ of 1.2 at 850 K in case of $Na_{0.007}Pb_{0.993}Se$.[50] The lower $\kappa_L$ of PbSe as compared to PbTe is related to larger anharmonic vibrations of the PbSe lattice.[51] Recently, layered SnSe, which crystallizes in a three-dimensionally distorted NaCl structure, was revealed to possess a remarkably low $\kappa_L < 0.4$ W $m^{-1}K^{-1}$ at 923 K. This material's low lattice thermal conductivity was attributed to large phonon-phonon scattering due to a large anharmonicity.[52] The proportionality constant that relates the atom displacement to the potential energy is called the spring constant. In this case with large anharmonicity, increasing atom displacements from equilibrium causes a variation in spring constant and an enhancement of the phonon-phonon scattering accordingly. Consequently, a $zT$ of 2.3 for the undoped SnSe along the *b*-axis at 923 K was achieved.[53]

$Bi_2Te_3$-based materials are still known as one of the state-of-the art materials with substantial thermoelectric properties around room temperatures and above. $Bi_2Te_3$ crystallizes in a layered rhombohedral structure with layer orders of …Te-Bi-Te-Bi-Te… along the crystallographic *c*-direction. Therein, each Te atom is coordinated by six Bi atoms, and each Bi atom is similarly coordinated by six Te atoms (Figure 1.5). At the outside of this 5-layer package, each Te atom is surrounded by only three Bi atoms. Due to the anisotropic crystal structure, the physical properties are also anisotropic. For example, the value of the thermal

conductivity measured perpendicular to the *c*-axis is 1.5 W $m^{-1}K^{-1}$, which is over two times larger than the one along the *c*-axis, 0.7 W $m^{-1}K^{-1}$.[54]

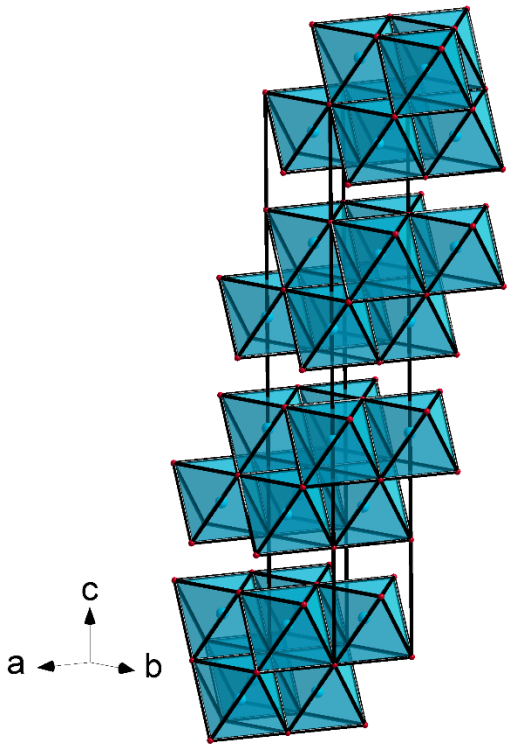


Figure 1.5 Layered crystal structure of $Bi_2Te_3$; octahedral $BiTe_6$ polyhedra are highlighted.[54]

### 1.4.4 Mass Difference (Mass Fluctuation)

Mass difference scattering, which is also known as mass fluctuation scattering, is one of the most important phonon scattering mechanisms. The strength of the phonon scattering caused by the mass fluctuation is expressed by

$$\Gamma = \sum f_i \left(1 - \frac{M_i}{\bar{M}}\right)^2 \qquad (1.19)$$

Where Γ is the strength of the phonon scattering, $f_i$ is the fractional concentration of the impurity mass, $M_i$ is the impurity mass and $\bar{M} = \sum f_i M_i$ is known as the mean atomic mass. Here, impurities are atoms with a different size and mass than that of the host atoms.[55] Further reductions to the lattice thermal conductivity of $Bi_2Te_3$ were accomplished by the formation of the solid solutions such as $Bi_2(Te_xSe_{1-x})_3$ and $(Bi_{1-x}Sb_x)_2Te_3$, which crystallize in the rhombohedral structure. By reducing the lattice thermal conductivity due to the mass fluctuation (alloy disorder), a maximum *zT* of 1.0 at 300 K for *n*-type $Bi_2Te_{2.7}Se_{0.3}$ and *p*-type $Bi_{0.5}Sb_{1.5}Te_3$ was achieved. [54]

Silicon-germanium alloy, $Si_{1-x}Ge_x$, could be utilized in thermoelectric applications at temperatures greater than 800 K with no significant deterioration. These alloys possess remarkably lower lattice thermal conductivity, namely 10 W $m^{-1}K^{-1}$ for $Si_{0.7}Ge_{0.3}$, than elemental Si, 150 W $m^{-1}K^{-1}$, and Ge, 63 W $m^{-1}K^{-1}$.[56] The largest *zT* of around 1.0 was reached for the *n*-type $Si_{0.8}Ge_{0.2}$ at 900 K, whereas the so far maximum *zT* value of the *p*-type $Si_{1-x}Ge_x$ materials is only 0.6.[57]

The materials studied in chapters 3 and 4 of this thesis, $Ba_3Cu_{16-x}Se_{11-y}Te_y$ and $Ba_3Cu_{16-x}S_{11-y}Te_y$, possess low lattice thermal conductivities as a result of mass fluctuation and complex structures.

### 1.4.5 Nanomodifications

Nanostructuring is a proven technique to improve the ratio of the electrical transport properties to thermal conductivity. Ideally, this technique decreases the short to medium phonon mean free paths due to scattering *via* grain boundaries, thereby effectively reduces the lattice thermal conductivity. Furthermore, enhancement of the Seebeck coefficient through energy filtering while the electrical conductivity chiefly remains unchanged, improves the ratio of the electrical transport properties to the thermal conductivity. A scheme of the effect of different nanoparticles and interfaces on mean free paths of the phonons and electrons is presented in Figure 1.6.[58–60]

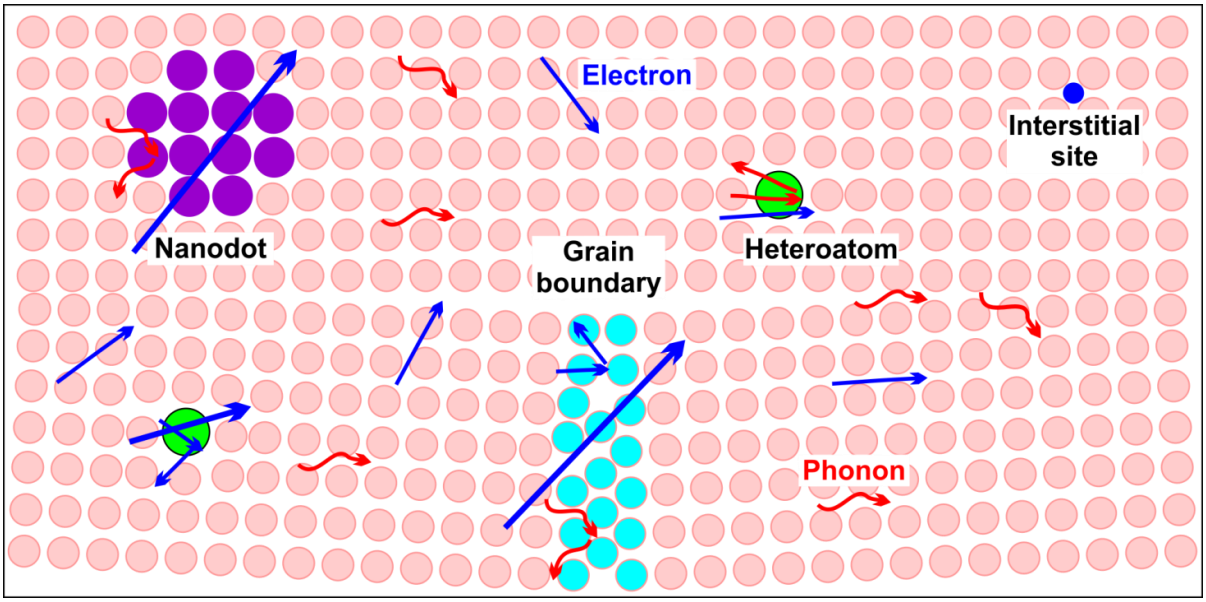


Figure 1.6 Effect of particles and interfaces on mean free paths of phonons and electrons. Reprinted with permission from ref.[61] Copyright 2019 Elsevier.

Further suppression of very low lattice thermal conductivities through nanomodifications is often unsuccessful, for instance in SnSe. In this example, the larger size of the grain boundaries as compared to the heat carrier phonons with smaller mean free path precluded the effective contribution of nanostructuring in reducing the lattice thermal conductivity.[52]

Nanomodifications of the state-of-the-art materials PbTe and $Bi_2Te_3$ lowered the lattice thermal conductivity and drastically increased the *zT* values. The LAST materials (Lead Antimony Silver Telluride) with the general formula of $AgPb_mSbTe_{m+2}$ are known for their remarkably low thermal conductivity due to the existence of Ag-Sb-rich nanodomains in an Ag-Sb-poor matrix.[62] These materials are solid solutions between $AgSbTe_2$ and PbTe with the cubic structure. Evidently, the nanodomains minimized the thermal conductivity to around 1.0 W $m^{-1}K^{-1}$ at 800 K for $AgPb_{18}SbTe_{20}$ with a peak *zT* of 2.2, which in fact outperforms the other thermoelectric materials at this temperature.

$Bi_2Te_3$/MWCNT nanocomposite, which was formed by adding 0 to 0.25 wt-% MWCNT (multi-wall carbon nanotubes), obtained a *zT* of 1.5 at 350 K. This showed an increase of about 50% in the *zT* value as compared to the bulk $Bi_2Te_3$ at the same temperature.[63] To date, the highest attained *zT* corresponding to $Bi_2Te_3/Sb_2Te_3$ superlattice is 2.4 at 300 K.[64] Another example of nanostructuring $Bi_2Te_3$-based materials includes nanostructuring of $(Bi_{1-x}Sb_x)_2Te_3$ through a method called SE-MS-SPS (single-element - melt-spinning - spark-plasma-sintering).[65] The nanostructured sample, which was synthesized through this fairly fast

synthetic process, exhibited a lower $\kappa_L$ = 0.40 W $m^{-1}K^{-1}$ compared to the commercial ingot with $\kappa_L$ = 0.70 W $m^{-1}K^{-1}$ above 300 K. Due to a larger Seebeck coefficient, lower thermal conductivity, and a nearly identical electrical conductivity, the nanostructured material exhibited a maximum *zT* of 1.5 at 390 K. This *zT* value is ~ 60% higher than the reported *zT* value for the bulk $(Bi_{1-x}Sb_x)_2Te_3$ at this temperature.

### 1.4.6 PLEC (Phonon-Liquid Electron-Crystal)

#### 1.4.6.1 Binary Copper Chalcogenides, $Cu_2Q$ (*Q* = S, Se, Te)

In binary copper chalcogenides, $Cu_2Q$ (*Q* = S, Se, Te), $\kappa_L$ decreases drastically by eliminating some of the vibrational modes. In typical solids, the heat capacity reaches or passes the Dulong-Petit limit, 3 $Nk_B$ (*N* is the number of the atoms and $k_B$ is the Boltzmann constant).[27] In contrast to most solids, the heat capacity of the $Cu_2Q$ compounds is very close to the liquid limit, 2 $Nk_B$ - 2.5 $Nk_B$, explaining the liquid-like behavior of these materials at high temperatures.

Copper selenide, $Cu_2Se$, experiences two phase transformations. The low temperature monoclinic $\alpha$ phase transforms to the high temperature cubic anti-fluorite $\beta$ phase above 410 K. The Cu ions are more ordered in the $\alpha$ phase, and they exhibit more disorder at high temperature $\beta$ phase. The high temperature $\beta$ phase is composed of two sublattices: the $Se^{2-}$ anions form a face-centered cubic sublattice, whereas the $Cu^+$ ions flow between the interstitial sites exhibiting superionic behavior. Therefore, liquid-like migration of the Cu ions causes the

reduction of the heat capacity to 2 $Nk_B$ - 2.5 $Nk_B$.[66,67] As a consequence of the superionic behavior of the Cu ions in the high temperature structures of the $Cu_2Q$ compounds, large $zT$ values of 1.0, 1.5 and 1.7 for copper telluride ($Cu_2Te$), $Cu_2Se$ and copper sulfide ($Cu_{1.97}S$) were achieved at 1000 K respectively.[68] Further suppression of the lattice thermal conductivity was achieved by the formation of $Cu_2S$ and $Cu_2Se$ solid solutions.[69] Hence, a decrease in thermal conductivity was established in slightly S-substituted $Cu_2Se$, $Cu_2S_{0.08}Se_{0.92}$, due to larger phonon scattering *via* alloy disorder. A smaller copper vacancy also occurred, since the ionic bonds of Cu–S are stronger than those in Cu–Se. Ultimately, a $zT$ value of 2.0 at 1000 K was attained.[70]

$Cu_2Te$ has the most phase transformations among all $Cu_2Q$ and the smallest $zT$ compared to the rest of the $Cu_2Q$ materials. Undoped $Cu_2Te$ achieved a peak $zT$ of 0.29 at 900 K while doping this material with Ag, increased the $zT$ to 1.0 at the same temperature.[71] Tellurides have larger copper vacancies than sulfides or selenides. This is a result of a smaller electronegativity difference between Cu and Te atoms, and more covalent behavior of Cu–Te bonds. Furthermore, formation of $Cu_2S$/Se-$Cu_2Te$ alloys not only reduced $\kappa_L$ of the high temperature disordered phase, but it also tuned the charge carrier density to the optimal values. By applying the nanoscale concept of mosaicity, the electrical transport properties and thermal conductivity of the mosaic bulk $Cu_2$(S,Te) surpassed those of the high temperature $Cu_2S$ and $Cu_2Te$.[72] Due to nearly identical orientations of mosaic crystals inside the bulk mosaics, in contrast to the typical polycrystalline compounds, these mosaic blocks behave as single crystals. Therefore, great electrical properties were resulted due to the consistency of the

lattice. On the other hand, phonon scattering due to the existence of grain boundaries led to a low thermal conductivity (*i.e.* ~ 0.4 W $m^{-1}K^{-1}$ at 1000 K for $Cu_2S_{0.52}Te_{0.48}$). Meanwhile, a large power factor of ~ 9.0 $\mu$W $cm^{-1}K^{-2}$ at this temperature allowed a *zT* value of 2.1 to be achieved. Nanostructuring of $Cu_2Se$ through ball milling followed by spark plasma sintering (SPS) introduced a variety of defects as well as a larger number of grains; thereby resulting in a very low thermal conductivity of 0.34 W $m^{-1}K^{-1}$. With this *zT* of 2.1 at 973 K, nanostructured $Cu_2Se$ outperforms other thermoelectric materials at this temperature.[73]

### 1.4.6.2 Ternary Copper Chalcogenides

$CuCrSe_2$ has a layered structure composed of $CrSe_2^-$ layers and mobile $Cu^+$ ions between these layers. As a result of Cu ion migration, this material is a superionic conductor with a large *zT* value of 1.0 at 773 K.[74] Further enhancement of the *zT* value was accomplished in a $(AgCrSe_2)_{0.5}(CuCrSe_2)_{0.5}$ nanocomposite. A very low thermal conductivity of 0.2 at 773 K resulted in a *zT* of 1.4 at this temperature for this material.[75]

High temperature bornite, $Cu_5FeS_4$, crystallizes in the $\alpha$-$Cu_2S$ structure.[76] Comprising disordered Cu, Fe atoms and vacancies at elevated temperatures, $Cu_5FeS_4$ exhibits a very low lattice thermal conductivity of around 0.5 W $m^{-1}K^{-1}$. Optimizing an electrical conductivity while retaining a high Seebeck coefficient, a maximal *zT* value of 1.2 at 900 K for a solid solution, $0.8CuS_4$-$0.2Cu_5FeS_4$, was attained.

$Cu_8GeSe_6$ possesses a very low thermal conductivity of ~ 0.3 W $m^{-1}K^{-1}$ at 750 K and a $zT$ of 0.5 at this temperature.[77] The low thermal conductivity in this example was understood as a result of the weak bonding between the Cu ions and [$GeSe_6$] sublattice. Benefiting from alloying of Cu/Ag and Se/Te, the low $\kappa_L$ was preserved while the electrical conductivity was significantly enhanced. This was attributed to larger Cu deficiency which was caused by weaker Cu–Te bonds as compared to Cu–Se bonds.

## 1.5 Stability of the Copper Chalcogenides

Thermoelectric materials must be thermally and mechanically stable in order for them to be successfully employed in thermoelectric devices.

Cu ion migration in $\beta$-$Cu_2Se$ has a detrimental effect on thermoelectric properties of this material at higher temperatures, because applying a large current through the material at 1200 K resulted in device deterioration. This degradation was proven by the observation of a Cu gradient between two ends of a measured bar of $Cu_2Se$. Finally, evaporation of Se and precipitation of Cu, degraded the material. To further investigate the stability issue, an electromigration experiment was designed by using a modified Seebeck apparatus (operation was allowed with applied current). After applying current through a specimen for 24 hours with the Cu ion direction being opposite to temperature gradient, optical observation proved deformation in the measured sample.[78]

In addition, the stability issue in $\beta$-$Cu_{2-x}S$ (prepared through the melt-solidification technique) was illustrated through non-reproducible thermoelectric physical property measurements.[79] This stability issue was observed in other ionic conducting materials such as ternary copper chalcogenides, $Cu_7PSe_6$.[80] After an order-disorder phase transition above 300 K, an unrestricted Cu ion migration occurs in this material. Stability investigations through cycling the thermoelectric properties for six cycles revealed non-reproducibility between consecutive measurements. Sample decomposition and darker areas related to decomposed products were observed on sides of the measured pellet. In conclusion, materials that may be ionically conducting should be tested prior to thermoelectric applications to prevent devices from deforming due to ion migration.

In order to make highly ionic conductive materials more applicable for thermoelectric purposes, long range movement of ions should be restricted. In copper chalcogenides, improving the stability of $Cu_{2-x}S$ and $Cu_{2-x}Se$ continues to be in the focus of many researchers.

In $Cu_2Se/CuInSe_2$ nanocomposites, the long-range phonon path was successfully shortened.[81] Although, $Cu_2Se$ and $CuInSe_2$ both crystallize in a cubic structure, statistical distributions of cations and vacancies over interstitial sites are not the same. Hence, a minimal solubility between the two compounds occurs. In this work, the best thermoelectric performance was reported to be a $zT = 2.6$ for a sample that contained 1 mole-% In at 850 K. Adding 1 mole-% In, resulted in more than 50% increase of the electrical conductivity. As mentioned by the authors, this is possibly a result of incorporating In atoms into the $Cu_2Se$

lattice by filling under-occupied Cu sites in $Cu_2Se$. In contrast to $Cu_2Se$ (which physically deformed by applying approximately ten times less current density), the stability of $Cu_2Se/CuInSe_2$ was successfully demonstrated by applying a current density of 100 A $cm^{-2}$ to a sample with 1 mole-% In for 24 hours.

Introducing different concentrations of elements such as Sn to $Cu_2Se$, $Cu_{2(1-x)}Sn_xSe$ was formed.[82] This material then was shown to be effectively impeding the phonon propagation. As demonstrated, the sample $Cu_{1.98}Sn_{0.01}Se$ exhibited the lowest lattice thermal conductivity, *i.e.* 0.49 W $m^{-1}K^{-1}$ at 825 K, among all other samples with different Sn concentrations. The isolated SnSe secondary phase scatters lower frequency phonons more effectively in $Cu_{1.98}Sn_{0.01}Se$ than the other materials with higher Sn concentrations.[83] Indeed, the secondary phase is more developed in the samples with more doped Sn than $Cu_{1.98}Sn_{0.01}Se$ which in part prevents parts of $Cu_2Se$ from scattering phonons. Finally, possessing a $zT$ = 1.0 at 823 K, $Cu_{1.98}Sn_{0.01}Se$ performed better than $Cu_2Se$. Performing stress tests on $Cu_{2(1-x)}Sn_xSe$ at 773 K, revealed the role of the Sn dopant in reducing the density loss as compared to $Cu_2Se$. However, as an issue with the Cu precipitation and Se evaporation exists for $Cu_{1.90}Sn_{0.05}Se$, these materials are not quite feasible for thermoelectric applications.

In another report, Li-doped $Cu_2Se$, $Li_{0.09}Cu_{1.9}Se$, was shown to be more stable than the undoped $Cu_2Se$.[84] The larger stability of the doped sample was demonstrated based on the higher activation energy for ion conduction in these materials as compared to $Cu_2Se$. A fixed Li atom sublattice, which is formed due to a large degree of hybridization between the *s* orbitals

of Li with *p* orbitals of Se, suppressed the mobility of Li atoms. Therefore, the presence of the not mobile Li atoms in a path of tetrahedral and octahedral interstitial sites, impeded a long-range movement of Cu ions, thereby brought about more stability compared to the undoped material. Moreover, $Li_{0.09}Cu_{1.9}Se$ with its $zT > 1.4$ at 1000 K, matches the $Cu_2Se$ performance at the same temperature.[85]

As mentioned earlier, high temperature $Cu_5FeS_4$ has a similar crystal structure to $\alpha$-$Cu_2S$. In contrast to $Cu_2S$ structure, in $Cu_5FeS_4$, two of the Cu sites are vacancies, whereas one out of eight Cu sites are occupied by Fe atoms. Although high deficiency can potentially increase the Cu ion conduction, the Fe atoms restrict the ion conduction. Therefore, this material is a good example of a copper chalcogenide stable at high temperatures.[76,86]

In addition to the attempts to chemically improve the stability of the copper chalcogenide, it was recently shown that utilizing ion-blocking interfaces in device legs can increase the stability.[87] In this work, the importance of chemical diffusion difference in decomposition of the thermoelectric legs was discussed. Ultimately, it was concluded that in order to prevent Cu atoms from precipitating, the chemical potential difference must be adjusted to remain below the decomposition threshold. Hence, ion-blocking interfaces that still conduct electrons were introduced to the device segments.

## 1.6 Barium Copper Chalcogenides

Benefiting from the large cation, $Ba^{2+}$, barium copper chalcogenides should presumably have a low lattice thermal conductivity. This physical property could further decrease in the case of tellurides. On the other hand, in materials with mixed chalcogen atom sites, the mass fluctuation on these sites may even further reduce the lattice thermal conductivity.

The first such reports concerned the ternary barium copper chalcogenide $\beta$-$BaCu_2S_2$, which crystallizes in the $ThCr_2Si_2$-type layered structure with a space group of *I*4/*mmm*. This structure is composed of a two dimensional anti-PbO $[Cu_2S_2]^{2-}$ framework, which is sandwiched by Ba sheets.[88] The room temperature thermal conductivity for $\beta$-$BaCu_2S_2$ was reported to be 0.86 W $m^{-1}K^{-1}$ and around 0.60 W $m^{-1}K^{-1}$ at 867 K,[89] which is for instance smaller than the thermal conductivity of the state-of-the-art TAGS, $(GeTe)_{1-x}(AgSbTe_2)_x$, at these temperatures. Doping $\beta$-$BaCu_2S_2$ with potassium increased the charge carrier concentration tenfold and resulted in a higher *zT* value of 0.23 for $\beta$-$K_{0.05}Ba_{0.95}Cu_2S_2$, compared to the *zT* of 0.17 for the undoped material at 820 K.[89]

$\beta$-$BaCu_2Se_2$ crystallizes in the same structure as $\beta$-$BaCu_2S_2$ with a band gap of 1.8 eV.[90] Using sodium as a dopant, the carrier concentration with holes as dominant carriers was increased from $1.7 \times 10^{18}$ $cm^{-3}$ for the undoped material to $2.6 \times 10^{20}$ $cm^{-3}$ for $Ba_{0.9}Na_{0.1}Cu_2Se_2$.[91] A huge enhancement in the electrical conductivity in the measured

temperature range occurred as a result of the increase in the charge carrier concentration. Thereby, a maximal *zT* of 1.0 was reached by $Ba_{0.925}Na_{0.075}Cu_2Se_2$ at 773 K.

In contrast to the above-mentioned barium copper chalcogenides, $BaCu_2Te_2$ crystallizes in the $\alpha$-$BaCu_2S_2$ type structure, an orthorhombic crystal structure with the space group *Pnma*. The structure of $BaCu_2Te_2$ is composed of a three dimensional $[Cu_2Te_2]^{2-}$ framework. Connecting tetrahedral $CuTe_4$ units *via* sharing edges and vertices results in a channel-like anionic framework with $Ba^{2+}$ cations located inside the channel.[92] Due to a low thermal conductivity and moderate electrical transport properties, a *zT* of 0.72 was achieved by $BaCu_2Te_2$ at 823 K. Recently, an improvement in the performance of $BaCu_2Te_2$ by partially alloying this material was demonstrated.[93] As expected in $BaCu_{2-x}Ag_xTe_2$, replacing Cu atoms with Ag led to a reduction in the density of holes, thereby increasing the carrier mobility. In addition, using the SPB (single parabolic band) model, $BaCu_{2-x}Ag_xTe_2$ was shown to have a larger effective mass ($m^*$) than the undoped material, which is related to an enhanced density of states close to the Fermi level. As a result of a concurrent decrease and increase in the mobility, total mobility did not change noticeably. Finally, decreasing $\kappa_L$ by increasing the amount of Ag, increased the *zT* of the material $BaCu_{1.9}Ag_{0.1}Te_2$ to 1.08 at 823 K.

The investigation into ternary and quaternary barium copper chalcogenides in our group began over a decade ago.[94–101] The discovered copper chalcogenides typically possess complex crystal structures and low lattice thermal conductivity. Some of these materials

contain nonclassical Cu–Cu bonds with under-occupied Cu atom sites which may result in a movement of $Cu^{+}$ ions in the entire material.

$Ba_3Cu_{14-x}Te_{12}$ crystallizes in a monoclinic structure with a space group of $P2_1/m$. In this structure, Cu atoms are tetrahedrally coordinated.[94] The corner-, edge- and face-sharing $CuTe_4$ units are connected through relatively planer $CuTe_3$ units. Such planar units were also observed in $Ba_2Cu_{6-x}STe_4$.[97] In this structure, $Te_2^{2-}$ dumbbells with a 2.9 Å bond distance between Te atoms as well as $Te^{2-}$ anions are present. A short distance < 3 Å between Cu atoms, results in a formation of Cu–Cu bonds and a cluster composed of 20 Cu atoms. Meanwhile, 6 Cu sites out of the 19 total Cu sites with site occupancies between 15% and 92% are deficient. The electronic structure calculation showed a band gap of 0.1 eV for the electron-precise compound $(Ba^{2+})_3(Cu^{+})_{14}(Te_2^{2-})_2(Te^{2-})_8$. $Ba_3Cu_{13.88}Te_{12}$ was shown to possess a moderate electrical conductivity of 190 $\Omega^{-1}cm^{-1}$, a Seebeck of +30 $\mu$V $K^{-1}$ at room temperature, and a low thermal conductivity around 1.0 W $m^{-1}K^{-1}$ at 300 K. This material could potentially have a fairly good performance at elevated temperatures. Once properties are measured at high temperatures, sample stability in the measurement range will also require testing.

## 1.7 State-of-the-art Thermoelectrics

Some of the *p*-type state-of-the-art thermoelectric materials with low thermal conductivities and high performances at elevated temperatures are listed in Table 1.1. Although all the listed materials possess fairly low thermal conductivities, the high figure-of-merit in some of these materials is a result of the optimization of the electrical transport properties.

Table 1.1 Selected state-of-the-art *p*-type thermoelectric materials.

| Material | $\kappa$ (W m$^{-1}$K$^{-1}$) | $zT_{max}$ at $T$ | Reference |
|---|---|---|---|
| $\beta$-$Cu_2Se$* | 0.38-0.74 | 1.5-2.1 at 1000 K | [27,73,102] |
| $Cu_{1.97}S$ | 0.49 | 1.7 at 1000 K | [68] |
| $Cu_2Se/CuInSe_2$ | 0.41 | 2.6 at 850 K | [81] |
| Ag-doped $Cu_2Te$ | 1.4 | 1.0 at 900 K | [103] |
| $Cu_2S_{0.08}Se_{0.92}$ | 0.55 | 2.0 at 1000 K | [70] |
| $Cu_2S_{0.2}Se_{0.8}$ | 0.42 | 1.7 at 950 K | [69] |
| $Cu_{1.94}S_{0.5}Se_{0.5}$ | 0.57 | 2.3 at 1000 K | [104] |
| $Cu_2S_{0.52}Te_{0.48}$ | 0.31 | 2.1 at 1000 K | [72] |
| $CuGaTe_2$ | 0.78 | 1.4 at 950 K | [105] |
| $CuInTe_2$ | 0.59 | 1.2 at 850 K | [106] |
| $Cu_{4.972}Fe_{0.968}S_4$ | 0.31 | 0.79 at 550 K | [107] |
| CuAgSe | 0.47 | 0.95 at 623 K | [108] |
| $BaCu_{5.9}SeTe_6$ | 0.46 | 0.81 at 600 K | [109] |
| $Cu_2Sn_{0.90}In_{0.10}Se_3$ | 0.78 | 1.1 at 850 K | [110] |
| $Cu_3Sn_{0.10}Sb_{0.88}Bi_{0.02}Se_4$ | 0.98 | 1.3 at 650 K | [111] |
| $Cu_{11}MnSb_4S_{13}$ | 0.20 | 1.1 at 575 K | [112] |
| $Cu_{26}Ta_2Sn_{5.5}S_{32}$ | 0.54 | 1.0 at 670 K | [113] |
| $Cu_{26}Nb_2Ge_6S_{32}$ | 0.54 | 1.0 at 670 K | [113] |
| $AgSb_{0.99}Sn_{0.01}Se_2$ | 0.44 | 1.2 at 660 K | [114] |
| LAST-*m* | 1.1 | 2.2 at 800 K | [62,115] |

| | | | |
|---|---|---|---|
| TAGS-80 | 1.5 | 1.8 at 773 K | [116] |
| $\beta$-$Zn_4Sb_3$ | 0.70 | 1.3 at 670 K | [43] |
| SnSe (along the *b*-axis) | 0.34 | 2.3 at 923 K | [53] |
| $Na_{0.007}Pb_{0.993}Se$ | 1.1 | 1.2 at 850 K | [50] |
| $Pb_{0.975}Na_{0.025}S$ + SrS (3.0 at-%) | 0.72 | 1.2 at 923 K | [117] |
| $Pb_{0.98}$ $Na_{0.02}Te$ + SrTe (4.0 mol%) | 0.96 | 2.2 at 915 K | [118] |
| $Tl_9BiTe_6$ | 0.34 | 0.96 at 500 K | [119,120] |
| $Tl_{8.05}Sn_{1.95}Te_6$ | 0.41 | 1.3 at 685 K | [121] |
| $Tl_{8.10}Pb_{1.90}Te_6$ | 0.45 | 1.5 at 685 K | [121] |
| $Tl_2Ag_{12}Te_{7.4}$ | 0.26 | 1.1 at 520 K | [122] |
| $Tl_{0.02}Pb_{0.98}Te$ | 0.96 | 1.8 at 770 K | [123] |
| $TlAg_9Te_5$ | 0.22 | 1.2 at 700 K | [124] |
| $Ba_8Ni_{0.31}Zn_{0.52}Ga_{13.06}Ge_{32.2}$ | 1.3 | 1.2 at 1000 K | [125] |
| $Yb_{14}MnSb_{11}$ | 0.70 | 1.1 at 1275 K | [46] |
| $Yb_{14}Mn_{0.4}Al_{0.6}Sb_{11}$ | 0.62 | 1.3 at 1200 K | [126] |
| Textured $Bi_{0.875}Ba_{0.125}CuSeO$ | 0.6 | 1.4 at 923 K | [127,128] |

**zT* increases with nano structuring and based on the different methods of synthesis.

## 1.8 Scope of This Thesis

As mentioned earlier, the copper chalcogenides $Cu_{2-x}S$ and $\beta$-$Cu_{2-x}Se$ are known for their excellent thermoelectric performances. However, their application in thermoelectric devices at elevated temperatures remains problematic for their poor stability due to the Cu ion

migration at these temperatures. As a solution to this issue, incorporating larger elements such as Ba and Te was considered as a strategy in the last decade in the Kleinke group to reduce the Cu ion migration. Accordingly, new materials, $Ba_3Cu_{16-x}Se_{11-y}Te_y$[99], $Ba_3Cu_{16-x}S_{11-y}Te_y$[101] and $BaCu_{6-x}Se_{1-y}Te_{6+y}$[98] were uncovered. The challenge of this thesis was to investigate in how far these materials can be optimized to exhibit advanced thermoelectric performance combined with superior stability, in contrast to $Cu_{2-x}S$ and $\beta$ -$Cu_{2-x}Se$.

# 2. Synthesis and Characterization Methods

## 2.1 Syntheses

All compounds in this thesis were formed by a melting and slow cooling process. To avoid samples from getting oxidized, all sample preparation steps were carried out in an argon-filled MBRAUN glove box with oxygen and water levels below 0.1 ppm. Stoichiometric amounts of each element were weighed, loaded in fused silica tubes, and transferred to a vacuum line connected to an Edwards Rotary oil pump (RV8 model). After reaching a pressure of around $10^{-4}$ mbar, the tubes were sealed using a $H_2/O_2$ torch. The syntheses took place in programmable furnaces (Lindberg/Blue, 1373 K Box Furnace, BF51800 series), where different steps of the reactions were programmed. In all cases, a hard solid was formed as a product, which was ground to a fine powder for characterization by powder XRD (PXRD). In some cases, samples were annealed further in manual furnaces (Barnstead International, models: 1373 K FB1300 & FB1400) to obtain higher homogeneity and purity.

## 2.2 Characterization and Measurements

### 2.2.1 X-ray Diffraction

Electromagnetic radiation with short wavelength in the range of 0.1 Å – 10 Å, known as X-rays, were initially produced and discovered by the German physicist, Wilhem

Röntgen.[129] By exploring the diffraction of the beams by crystals, Max von Laue in 1912 introduced X-rays as a useful method to learn more about crystal lattices.[130]

Using the same analogy with diffracted light, Laue proposed the formulae shown in Equation 2.1. In these equations, *a*/*b*/*c* are rows of atoms with regular spacings, and $\mu$ and $\upsilon$ are incident and reflected beams, respectively.

$$\text{a) } h\lambda = a\ (\cos\upsilon_1 + \cos\mu_1) \qquad \text{b) } k\lambda = b\ (\cos\upsilon_2 + \cos\mu_2) \qquad \text{c) } l\lambda = c\ (\cos\upsilon_3 + \cos\mu_3) \tag{2.1}$$

The mentioned parameters in Equation 2.1 are illustrated in Figure 2.1. Emitted waves of photons from different blocks of a crystalline material with repeating units could constructively interfere only in the Laue cone.

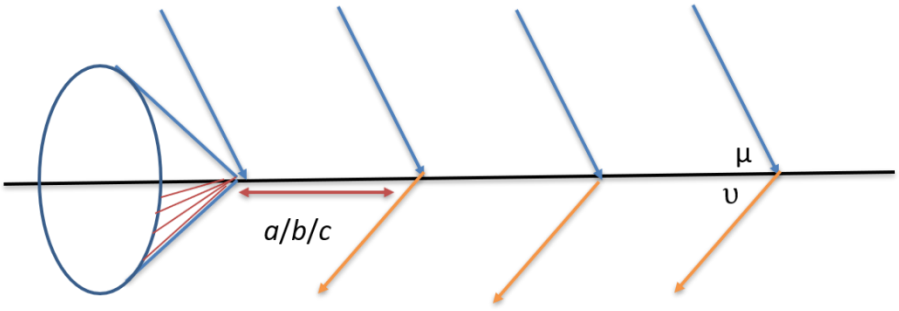


Figure 2.1 Constructive interference of the beams in the Laue cone.

Thereafter, father and son William Henry and William Lawrence Bragg proposed a simplified form of the Equation 2.1 which is also known as Bragg's law (Equation 2.2).[131,132] A schematic representation of the Bragg's law is illustrated in Figure 2.2. As per this equation, interferences are constructive only when the right side of the equation equals to the multiplication of an integer ($n$) by the wavelength ($\lambda$).

$$n\lambda = 2dsin\theta \qquad (2.2)$$

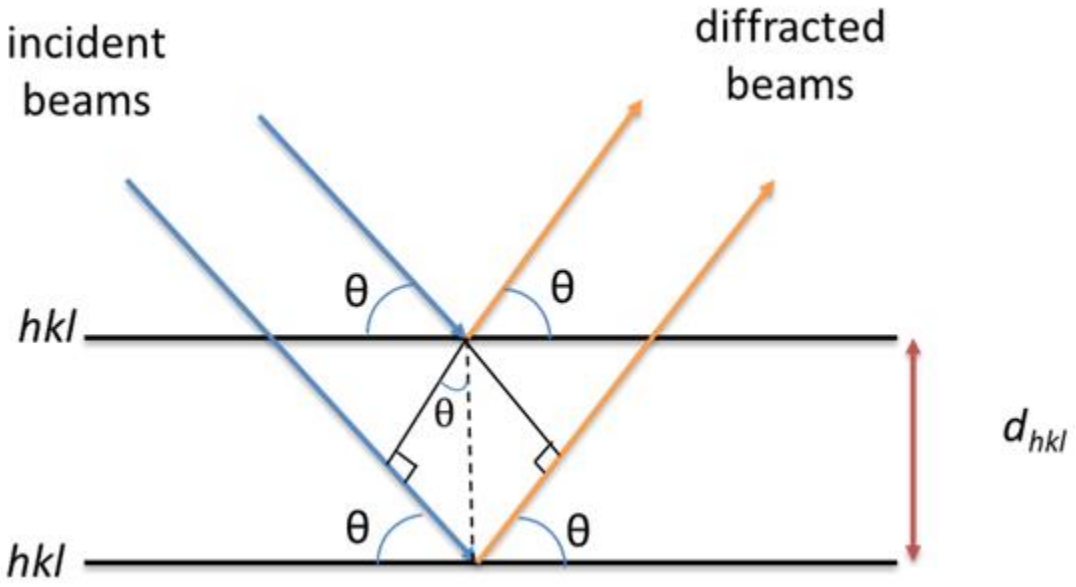


Figure 2.2 Constructive interference of beams according to Bragg's law.

Phase purities of the synthesized compounds were confirmed by performing PXRD on an INEL powder XRD instrument equipped with a position-sensitive detector employing Cu-$K_{\alpha 1}$ radiation ($\lambda$ = 1.540598 Å). This instrument operates by heating a tungsten filament

(cathode) in order to emit electrons. These electrons flow towards a copper target (anode) by the applied accelerated voltage. Finally, the accelerated electrons collide with the anode, resulting in the formation of X-rays (Bremsstrahlung). Moreover, electrons with sufficient energy remove electrons from the inner shells of the target material (here: copper) and the electrons from outer shells fill the vacancies inside the inner shells. Concurrently, X-rays with the same energy as the energy difference between the inner and outer shell electrons are produced (characteristic X-rays). The characteristic X-ray spectrum is comprosed of two components, $K_\alpha$ (which consists of $K_{\alpha1}$ and $K_{\alpha2}$) and $K_\beta$, where $K_\alpha$ is more intense than $K_\beta$. Therefore, the more intense $K_\alpha$ is utilized in X-ray characterization. Here, Cu-$K_{\alpha1}$ radiation ($\lambda$ = 1.540598 Å) was produced by using a germanium single crystal monochromator.

### 2.2.2 Single Crystal X-ray Diffraction

A Bruker Kappa Apex II instrument equipped with a CCD (charge-coupled device) detector which utilizes Mo-$K_\alpha$ radiation ($\lambda$ = 0.71073 Å) was used for data collection in this thesis. For a complete dataset ω scans were employed in different sets of frames to collect the data. After the data collection, the raw X-ray intensity of the reflections were corrected for Lorentz ($L$) and polarization ($p$) effects, since their intensities were reduced with a $Lp$ Lorentz-polarization factor to ($I_{hkl}$) (Equation 2.3 and 2.4) using APEX II suite.[133]

$$I_{hkl} = KLp.F_{hkl}^2 \qquad (2.3)$$

$$Lp = \frac{1+ cos^2 2\theta}{2Sin2\theta} \qquad (2.4)$$

In Equation 2.3, $K$ is a scaling factor and $F_{hkl}$ is the structure factor. $F_{hkl}$ is a parameter based on the scattered waves by all atoms of a unit cell for the *hkl* reflection. As was displayed in Equation 2.3, the square of this parameter is proportional to $I_{hkl}$. In addition, the observed structure factor ($F_o$) and the difference between $F_o$ and the calculated structure factor ($F_c$) directly affect the quality of the data collection and data refinement. A large similarity between $F_o$ and $F_c$ ensures an acceptable refinement. Finally, absorption corrections were applied by utilizing the empirical (multi-scan) method SADABS.[133]

All structure solutions and refinements were performed with the APEX II package (SHELXTL).[134] The structure solutions in this thesis were based on the direct methods, because most atoms used here have similar numbers of electrons. Platon program was used to standardize the atomic coordinates using the Tidy command and to check for any missing symmetry elements.[135]

The quality of the data collection was evaluated by the internal residual value ($R_{int}$) (Equation 2.5).

$$R_{int} = \frac{\sum|F_o^2 - F_{mean}^2|}{\sum F_o^2} \qquad (2.5)$$

Lastly, the positional parameters of the atoms (x, y, z), (anisotropic) thermal parameters, and site occupation factors (in case of mixed site occupancies/deficiencies) were

refined. A satisfactory refinement is achieved when the difference between $F_o$ and $F_c$ is small enough to result in *R* values below 5% (Equation 2.6 and Equation 2.7).

$$R_1 = \frac{\sum(|F_o| - |F_c|)}{\sum|F_o|} \qquad (2.6)$$

$$wR_2 = \sqrt{\frac{\sum w(F_o^2 - F_c^2)^2}{\sum w(F_o^2)^2}} \qquad (2.7)$$

In the Equation 2.7, *w* is the weighing parameter and $wR_2$ is the weighted *R* value. Goodness of fit (*GOF*) is also relevant to the difference of the observed and calculated structure factors. This parameter relates this difference between the number of the used reflections (*n*) and the number of refined parameters (*p*). An acceptable *GOF* is around unity (*GOF* ~ 1) (Equation 2.8).

$$GOF = \sqrt{\frac{\sum w(F_0^2 - F_c^2)^2}{n - p}} \qquad (2.8)$$

## 2.3 Scanning Electron Microscope

Incident electrons undergo an energy loss when they interact with electrons and atoms of a specimen.[136] The energy loss occurs because an extensive amount of energy is transferred from these incident electrons to the atoms. This energy loss is related to different parameters such as binding energies of the specimens' electrons. The excitation of the specimens'

electrons causes a generation of secondary electrons (SE). The secondary electrons with small energies, 3 eV - 5 eV, escape from the surface of the sample (a few nanometers from the surface) and provide topographic and compositional information about the sample. Secondary electrons are caused from inelastic scattering and have energies < 50 eV. The process of transferring a large amount of energy to atoms of a target material when the incident electrons interact with target material's electrons is known as inelastic scattering. However, elastic scattering of the incident electrons results in a generation of back scattered electrons (BSE) with energies > 50 eV. The occurrence of elastic scattering is due to a deflection of the incident electrons by the atomic nucleus or by the valence electrons of the sample. The generated electrons through elastic scattering bounce back in a variety of angles with many electrons bouncing back to their source. However, the back scattered electrons are elastically scattered in angles larger than 90°. Elements possessing a large number of electrons (large atomic numbers) have larger back scattered signals. Since back scattered electrons have more energy compared to secondary electrons, and due to a low amount of absorption of these electrons by the sample, BSE signals are not restricted to a small region of the specimen. Hence, the quality of the produced image from BSE is worse than SE. However, BSE provides valuable information about deeper surfaces of the sample since a wide range of escape depth is possible. In addition, BSE images are also useful for gaining more insight into compositions of the measured samples. In summary, valuable topographic and compositional information from both SE and BSE can be obtained.

Energy Dispersive X-ray Spectroscopy (EDS or EDX) is a microanalytical technique which is utilized for elemental analysis. This technique reveals quantitative information about measured samples based on the formation of characteristic X-rays; as previously explained in section 2.2.1. In this thesis, QuantaFeg 250/Oxford instrument x-act Scanning Electron Microscopy/Energy-Dispersive X-ray analysis (SEM/EDX) was utilized to learn more about composition, homogeneity and possible changes in samples after synthesis and after physical property measurements.

## 2.4 Sample Densification

In order to measure physical properties, phase pure samples should be densified. In this thesis, hot-pressing (HP) utilized as a consolidation technique. Sintering is a process of shaping polycrystalline materials by heating below melting point. Applying pressure to the heated powder leads to a diffusion of powder particles and thus densification. Here, pure powders were transferred to cylindrical graphite dies with a dimension of 12.7 mm. This was followed by sintering at a certain temperature while applying pressure under an $Ar/H_2$ atmosphere to restrict the occurrence of oxidization. The Oxy-Gon FR-210-30T-ASA-160-EVC hot-press furnace system was used to consolidate all powderized samples.

Another technique of consolidation through sintering includes spark plasma sintering (SPS).[137] In SPS, powder is directly placed into a graphite die which is surrounded with two punches. A high DC pulsed current passes through the electrodes and the powder to generate

sparks and high temperature among the powder particles. A concurrent applied pressure while sintering, allows the powder to shape into a densified pellet. To prevent oxidation, sintering is performed under an argon atmosphere, similar to HP. The densification process is shorter in SPS compared to HP as a result of high heating rates due to internal heating. Thus, it only takes a few minutes for a sample to be sintered in SPS, while it might take a few hours for a sample to be sintered utilizing HP. Typically, the longer the sintering time, the greater the probability of forming side products. However, compounds synthesized in this thesis showed better homogeneity when sintering times were increased. Therefore, HP was utilized to consolidate all powder samples.

## 2.5 Physical Properties Measurements

### 2.5.1 Thermal Conductivity Determination

Density of the hot-pressed pellets were determined using the Archimedes' method. A Sartorius YDK01 density determination kit was employed for the density measurement. Experimental density was calculated using Equation 2.9.

$$\rho_d = \frac{w_a(\rho_l - 0.0012\ gcm^{-3})}{0.99983(w_a - w_l)} + 0.0012\ gcm^{-3} \qquad (2.9)$$

In Equation 2.9, $w_a$ is the weight of the sample in air, and $w_l$ the weight in water or ethanol. Based on the measured temperature of the liquid, its density was recorded ($\rho_l$). To correct errors caused by air buoyancy, the density of air at standard conditions, 0.0012 g cm$^{-3}$

is added to the formula. A value of 0.99983 is also included to the formula since it lessens the error caused by the depth of the immersion of the sample in ethanol or water.

Pellets with 98% - 99% of the theoretical maximum density were utilized to obtain thermal conductivity values. Thermal conductivity of a material can be calculated using Equation 2.10.

$$\kappa = \lambda \rho_{\mathrm{d}} C_{\mathrm{p}} \qquad (2.10)$$

Where $\lambda$ is thermal diffusivity, $\rho_{\mathrm{d}}$ is experimental density and $C_{\mathrm{p}}$ is heat capacity. The Dulong-Petit approximation was used to calculate $C_{\mathrm{p}}$.[138]

Thermal diffusivity was measured using a flash method.[139,140] In this method, a pulsed light source (either laser or xenon flash lamp) is irradiated to one surface of a disk or a square-shaped thin sample (bottom surface). An InSb infrared (IR) detector detects a temperature rise on the rear side of the sample (top surface). Data are recorded as a plot of temperature increase versus time. Thermal diffusivity was obtained from the Equation 2.11, initially proposed by Parker in 1961.[141]

$$\lambda = 0.1388 \frac{l^2}{t_{0.5}} \qquad (2.11)$$

Therefore, $\lambda$ is dependent on the thickness of the sample ($l$) and the time which takes for the top surface to reach half of the maximum temperature increase ($t_{0.5}$). Thermal diffusivity measurements were carried out on graphite coated samples. The graphite coating ensures a uniform heat absorption during the measurement. Thermal diffusivity measurements were performed on the Anter Flashline 3000 and TA Instruments DLF 1200 (Kleinke group, University of Waterloo), NETZSCH LFA 427 and NETZSCH LFA 467 (German Aerospace Center, DLR). To avoid any oxidation of the samples, measurements were carried out under a constant argon flow. A flash method is schematically presented in Figure 2.3. The experimental errors for all the utilized instruments are estimated as ±5%.

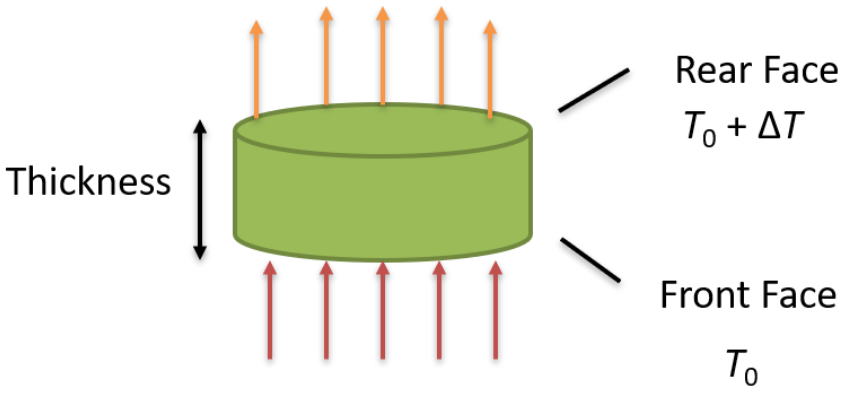


Figure 2.3 Schematic representation of a flash method.

### 2.5.2 Electrical Conductivity and Seebeck Coefficient Measurements

Electrical conductivity and Seebeck coefficient were measured at or above room temperature using the ZEM-3 (ULVAC-RIKO) under helium atmosphere.[142] This apparatus

works by passing a current through a sample that is sandwiched between two Ni electrodes. Voltage is then measured with two side R-type (Pt/Rh) thermocouples which are well-suited for high temperature applications. Samples with either rectangular or cylindrical geometry can be measured. However, only rectangular bars were measured in this thesis. Both the top and the bottom of the measured samples should be flat. In addition, the faces of the bars should be parallel. Then, proper contact between the sample and the electrodes results in an ohmic contact. as a constant current passes through the sample, the voltage is measured by the R-type electrodes, and the material's resistance is calculated with Ohm's law (Equation 2.12).

$$\Delta V = R.I \qquad (2.12)$$

Ultimately, by using the resistance of the sample ($R$), the restricted length between the thermocouples ($l$) and the cross-sectional area ($A$), electrical conductivity of the sample, $\sigma$, was calculated (Equation 2.13). The experimental errors are estimated as ±5%.

$$\sigma = \frac{l}{R.A} \qquad (2.13)$$

Seebeck coefficient, $\alpha$, is a measurement of the voltage difference between the side probes as a result of a temperature gradient, $\Delta T$, between these probes at $T_1$ and $T_2$ (Equation 2.14). The experimental errors are estimated as ±3%. The measurement setup is represented in Figure 2.4 schematically.

$$\alpha = \frac{\Delta V}{\Delta T} \qquad (2.14)$$

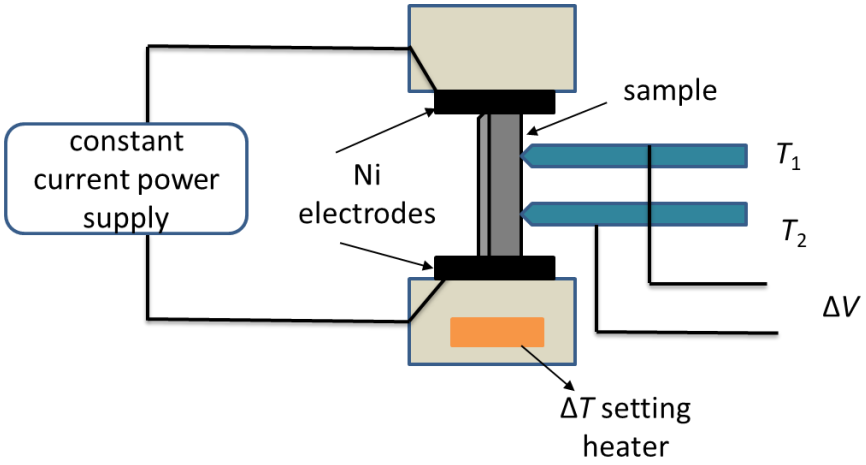


Figure 2.4 Schematic illustration of ULVAC ZEM-3 four-probe measurement.

The electrical transport properties were also measured using the HT-S-σ setup at DLR.[143] This setup can also perform as a high temperature four-probe electrical conductivity measurement, equipped with two temperature gradient heaters. The electrical transport properties were measured under an inert atmosphere with estimated errors of less than 4%.

## 2.6 Hall Measurement

Measuring charge carrier concentration is possible through a Hall measurement, which was introduced by Edwin Herbert Hall in 1879.[144] In this measurement, a current, *I*, passes through the length of a rectangular bar (along the x-axis), whereas a magnetic field, *B*, is

applied perpendicular to the current passage (along the z-axis). A Lorentz force caused by the magnetic field prevents the carriers from moving straight and pushes them towards the sides of the bar (y-axis).[145] Therefore, the resulting Hall voltage, $V_H$, can be measured. The Hall voltage and the Hall coefficient ($R_H$) are displayed in order in Equation 2.15 and 2.16.

$$V_H = \frac{IB}{net} \qquad (2.15)$$

$$R_H = \frac{1}{ne} = \frac{V_H t}{IB} \qquad (2.16)$$

Where, $n$, $e$ and $t$ are carrier concentration, elementary charge ($1.602 \times 10^{-19}$ C) and thickness of the sample, respectively. The Hall voltage properly defines the type of dominant carriers inside a conductor. If $V_H$ and subsequently $R_H$ are positive, then the majority of the carriers are holes. On the other hand, if both properties have negative signs, electrons are the dominant charge carriers. A schematic representation of the Hall effect is depicted in Figure 2.5.

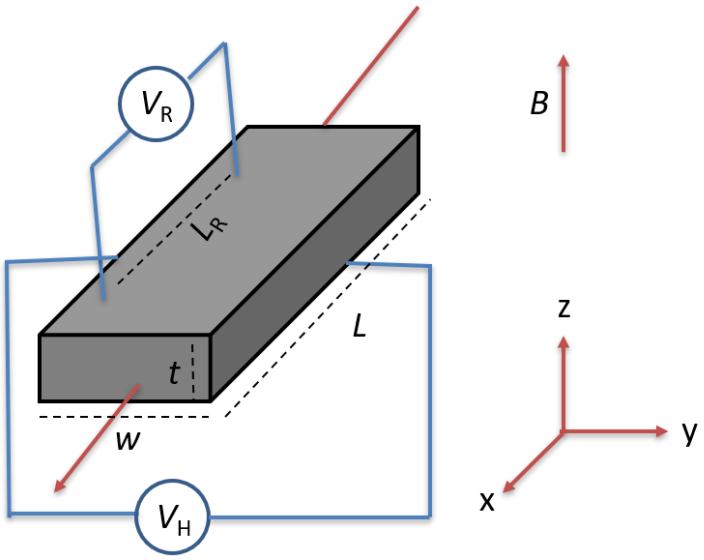


Figure 2.5 Schematic representation of Hall effect.

Hall measurements on the materials in this thesis were all carried out at the Department of Physics & Astronomy at University of Waterloo (Kycia group). All measurements were carried out at room temperature on bars with dimensions of ~ 8 × 2.5 × 1 mm. A 5 mA or lower current passed through the samples, and a magnetic field of 0.5 T was exerted. An error of ±1% related to the measurement of the Hall voltage was estimated. In addition, a systematic uncertainty of ±3% was a result of different errors in the measurements such as the bar dimensions and the errors in the measured Hall voltage. A material electrical conductivity was also calculated by measuring the voltage drop, $V_R$, through the length of the sample and by applying Ohm's law. Conductivity is calculated using Equation 2.17.

$$\sigma = \frac{IL_R}{V_R wt} \qquad (2.17)$$

Here, $\sigma$ is the electrical conductivity, $w$ is the width of the sample and $L_R$ is the distance between the voltage, $V_R$, probes. Lastly, mobility, $\mu$, was calculated from Equation 2.18.

$$\mu = \frac{\sigma}{ne} \qquad (2.18)$$

## 2.7 Differential Scanning Calorimetry

Differential Scanning Calorimetry (DSC) was utilized to learn further about physical and chemical changes in materials for various reasons. A NETZSCH STA 409 PC Luxx was used to study phase transformations and thermal stability.[146] The utilized DSC instrument is a heat-flux type, where a reference (with a known heat capacity) and a sample are placed in the same furnace chamber. A heat-flow path (*i.e.* silver) connects the reference and the sample for distributing the heat uniformly. A variation in enthalpy or specific heat compared to the reference results in a temperature difference ($\Delta T$) between the sample and the reference. The recorded $\Delta T$, which was measured as a voltage through chromel thermocouples, converts to the heat flow rate ($\Phi$) through calibration experiments with unique internal calibration files for NETZSCH (Equation 2.19). $\Phi$ is usually given in mW or $\mu$W, and $k$ is a constant. DSC combined with thermal gravimetry (TG) was used to determine sample stability, phase transformations, and mass changes upon heating or cooling the samples.

$$\phi = -k\Delta T \qquad (2.19)$$

# 3. Thermoelectric Properties and Stability of $Ba_3Cu_{16-x}Se_{11-y}Te_y$

## 3.1 Introduction

$Ba_3Cu_{16-x}Se_{11-y}Te_y$ only forms when mixed occupied chalcogen sites are present. According to density functional theory (DFT) calculations,[99] the electron-precise material with exactly 16 Cu atoms per formula unit, $(Ba^{2+})_3(Cu^{+})_{16}(Q^{2-})_{11}$ (with $Q$ = Se, Te), behaves as a semiconductor. The calculated band gap of 0.02 eV, along with the Cu atom deficiency results in a heavily doped *p*-type semiconductor.

The first article about these chalcogenides introduced the crystal structure, electronic structure and electrical properties (determined on a cold-pressed bar).[99] The full thermoelectric properties as well as the stability investigation of $Ba_3Cu_{16-x}Se_{11-y}Te_y$ is presented in this chapter and was published in 2019.[147]

## 3.2 Experimental Procedure

Samples with the nominal composition of $Ba_3Cu_{16-x}Se_{11-y}Te_y$ (x = 1.3, 1.6; y = 2.5, 2.8, 3) were synthesized from the elements (Ba pieces, 99.7%, Strem Chemicals; Cu powder, 99.5%, Alfa Aesar; Se pellets, 99.9%, Alfa Aesar; Te broken ingots, 99.99%, Strem

Chemicals). These values for x and y are well within the phase range ($1 < x < 2$; $2 < y < 4$). Reactions took place inside C-coated silica tubes in programmable box resistance furnaces. The tubes were heated up to 1023 K in twelve hours. Samples were kept at this temperature for ten hours followed by cooling to 873 K in 20 hours and annealing at this temperature for 100 hours. Thereafter, the furnace was switched off to allow for fast cooling down to room temperature.

The phase purity of the synthesized compounds was verified through powder X-ray diffraction analyses. The X-ray diffraction patterns of the phase pure samples are depicted in Figure 3.1.

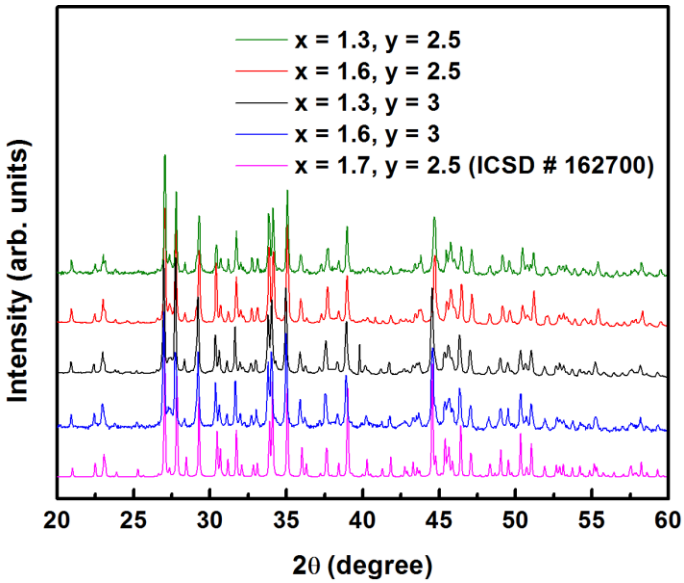


Figure 3.1 Room temperature X-ray powder patterns of $Ba_3Cu_{16-x}Se_{11-y}Te_y$.

Differential scanning calorimetry (DSC) and thermal gravimetry (TG) analyses were performed on a sample with the largest amount of Te, $Ba_3Cu_{14.4}Se_8Te_3$, under argon with a heating rate of 10 K $min^{-1}$ (Figure 3.2). There is no observation of a phase transformation aside from melting at 1008 K.

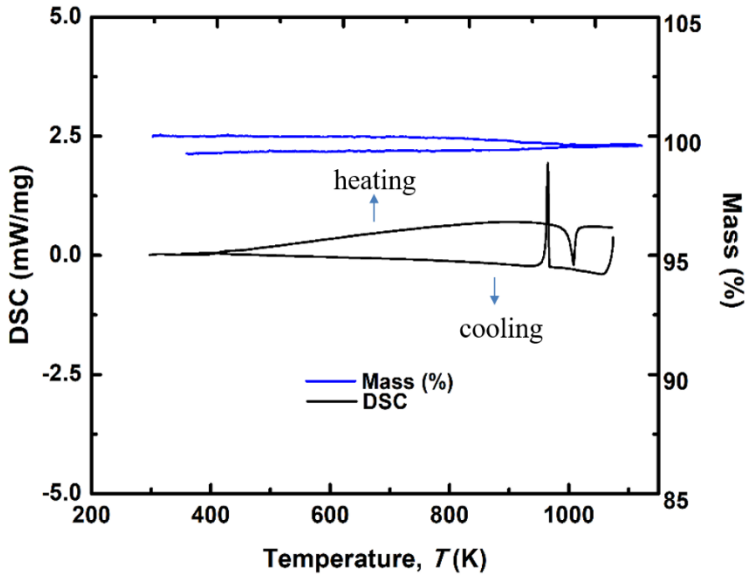


Figure 3.2 DSC/TG of $Ba_3Cu_{14.4}Se_8Te_3$. (heating rate of 10 K $min^{-1}$ under Ar atmosphere).

The ground pure samples were hot-pressed at 60 MPa at 800 K for 120 minutes. A density of almost 100% of the theoretical maximal values was achieved. For the physical property measurements, each hot-pressed sample was cut into half, resulting in two cylindrical pellets each with almost 2 g of weight. The thermal diffusivity measurement was performed on one of these pellets, while the other pellet was cut into a rectangular bar to perform the

electrical transport property measurements. This ensures that any changes during one measurement would have no impact on the other one.

The single crystals for single crystal analyses were selected under an optical microscope with all edges < 70 $\mu$m after crushing the polycrystalline samples. A Bruker Kappa Apex II CCD that employs Mo-*K*α radiation was utilized for the data collection on black block-like crystals. Using the search strategy of the APEX II suite, ω scans were performed in different sets of frames for full data coverage. The exposure time was 30 seconds per frame. The collected data were treated for Lorentz and polarization effects and absorption corrections.[133]

To check for a possible inhomogeneity after the electrical transport measurements, a potential-Seebeck-microprobe (PSM)[148] was utilized on a bar of nominal composition $Ba_3Cu_{14.7}Se_{8.2}Te_{2.8}$ with dimensions of 10 × 2 × 1.6 mm at room temperature. The PSM is a measurement of the local Seebeck coefficient of a semiconductor or a metal. In this measurement, the Seebeck coefficient is measured by moving a heated probe tip from point to point across the surface of the sample. The temperature of the probe and the sample is measured by a T-type thermocouple (Cu-CuNi). As a result of the heat flow between the probe tip and the sample, a local temperature gradient around the tip occurs. Finally, a voltage drop is measured by combining the thermocouple wires, and the Seebeck coefficient of the different points is obtained. Thereby, the PSM provides a two-dimensional image of the Seebeck values of the whole sample.

## 3.3 Results and Discussion

### 3.3.1 Crystal Structure and Crystallographic Data

$Ba_3Cu_{16-x}Se_{11-y}Te_y$ crystallizes in a rhombohedral structure (space group $R\bar{3}m$). The crystal structure of $Ba_3Cu_{16-x}Se_{11-y}Te_y$ is composed of $CuQ_4$ tetrahedral units (with shared chalcogen atom sites ($Q$ = Se, Te) that construct a three-dimensional network *via* corner-, face- and edge-sharing (Figure 3.3). Of the five crystallographically independent $Q$ sites, two are always two Se sites, one a Te site, one a mixed Se/Te site, and one an Se with up to 10% Te. The one Ba site is surrounded by eight $Q$ atoms in form of a bi-capped trigonal prism.

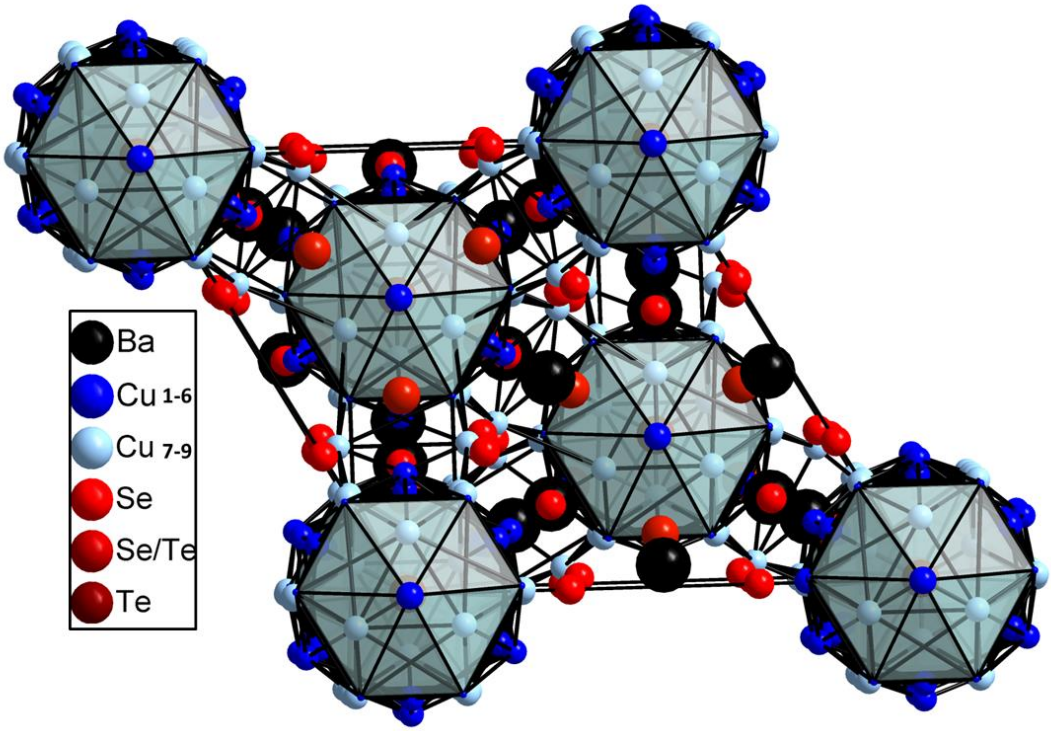


Figure 3.3 Crystal structure of $Ba_3Cu_{16-x}Se_{11-y}Te_y$ in a projection onto the *a,b* plane. The Cu atom clusters are highlighted as polyhedra.

In this structure, formally $d^{10}$–$d^{10}$ closed-shell interactions between the Cu atoms occur due to the hybridization of the filled *d* orbitals with the empty *s* and *p* orbitals.[149,150] The occurrence of such bonds in coinage chalcogenides is not rare; other examples include $BaCu_{6-x}Se_{1-y}Te_{6+y}$,[98] $Ba_3Cu_{14-x}Te_{12}$,[94] $Tl_2Ag_{12}Se_7$[151] and $Tl_2Ag_{12}Te_{7+x}$.[152] These Cu–Cu bonds, all shorter than 3 Å, not only result in the formation of Cu clusters with 26 Cu atoms, but also bond these clusters in three dimensions. As a consequence of the Cu deficient sites combined with the three-dimensional clusters, about 7% of the Cu ions could be successfully replaced at room temperature with Ag atoms, indicative of substantial Cu atom mobility.[99]

To further investigate the Cu ion mobility, room temperature X-ray single crystal analyses were performed on a single crystal of $Ba_3Cu_{14.7}Se_{8.5}Te_{2.5}$ before hot-pressing and after the electrical transport property measurements. The refinement[134] of the single crystal data from the sample of the nominal composition $Ba_3Cu_{14.7}Se_{8.5}Te_{2.5}$ before hot-pressing the sample with six Cu atom sites using the published model of $Ba_3Cu_{16-x}Se_{11-y}Te_y$ in the space group $R\bar{3}m$ resulted in $R(F_o) = 0.071$.[99] Large electron densities remained, namely 10.8 e Å$^{-3}$, 8.5 e Å$^{-3}$ and 4.5 e Å$^{-3}$, respectively. The positions of these three high residual electron densities were all surrounded by four chalcogen atoms at the appropriate Cu–Se/Te distances. Including these three positions as additional Cu7, Cu8 and Cu9 positions decreased the highest peaks in the difference Fourier map to acceptable values < 3 e Å$^{-3}$, and lowered $R(F_o)$ to 0.047. The refined occupancies of Cu7 – Cu9 were 0.26(1), 0.21(1), and 0.067(8), respectively. The formula was thus refined to be $Ba_3Cu_{14.59(8)}Se_{8.96(5)}Te_{2.04}$.

The refinement of the data of single crystal of the same sample after the electrical transport property measurements with the initial six Cu atom sites resulted in even larger residual electron densities of 25.9 e $Å^{-3}$, 24.7 e $Å^{-3}$ and 24.3 e $Å^{-3}$, and an unacceptable $R(F_o)$ = 0.148. Again, refining these as Cu-deficient sites yielded a final value of $R(F_o)$ = 0.033, with larger occupancies of 0.448(7), 0.339(7), and 0.309(4) for Cu7, Cu8 and Cu9, compared to the crystal before the property measurement, and the largest remaining electron density being 4.6 e $Å^{-3}$. The obtained formula of $Ba_3Cu_{14.60(2)}Se_{8.97(5)}Te_{2.03}$ is equal within one standard deviation to the one from before the property measurements, while the distribution of the Cu atoms changed significantly, with Cu1 – Cu5 showing smaller occupancies and Cu7 – Cu9 showing larger occupancies. The different distribution implies an irreversible movement of the Cu atoms either under the electric field or under the temperature gradient applied during the measurements. Table 3.1 and 3.2 contain the crystallographic details, fractional atomic coordinates, equivalent isotropic displacement parameters and site occupancies for these two data sets.

Table 3.1 Crystallographic details of the refinement of "$Ba_3Cu_{14.7}Se_{8.5}Te_{2.5}$"; I) before hot pressing: II) after the electrical transport property measurements.

| Refined formula | I) $Ba_3Cu_{14.59(8)}Se_{8.96(5)}Te_{2.04}$ | II) $Ba_3Cu_{14.60(2)}Se_{8.97(5)}Te_{2.03}$ |
|---|---|---|
| Formula weight | 2384.21 | 2382.21 |
| $T$ [K] | 296(2) | 296(2) |
| λ [Å] | 0.71073 | 0.71073 |
| Crystal system | Rhombohedral | Rhombohedral |
| Space group | $R\bar{3}m$ (no. 166) | $R\bar{3}m$ (no. 166) |
| $a$, $c$ [Å] | 12.1457(9), 28.165(2) | 12.108(1), 28.045(3) |
| $V$ [Å$^3$] | 3598.2(6) | 3560.4(9) |
| $Z$ | 6 | 6 |
| $R(Fo)$,[a] $R_w(Fo^2)$,[b] GOF (obs. data) | 0.047, 0.095, 1.15 | 0.033, 0.072, 1.04 |
| Min., max. residual electron density [e Å$^{-3}$] | -2.55, 2.92 | -2.74, 4.62 |

[a] $R(F_o) = \Sigma||F_o|-|F_c|| / \Sigma|F_o|$; [b] $R_w(F_o^2) = [\ \Sigma[w(F_o^2 - F_c^2)^2] / \Sigma[w(F_o^2)^2]\ ]^{1/2}$, with $F_o$ and $F_c$ being the observed and calculated structure factors, respectively.

Table 3.2 Fractional atomic coordinates and equivalent isotropic displacement parameters and occupancies of "$Ba_3Cu_{14.7}Se_{8.5}Te_{2.5}$"; I) before hot pressing; II) after the electrical transport property measurements.

| | x | y | z | I) $U_{eq}$/Å$^2$ | I) occ. | II) $U_{eq}$/Å$^2$ | II) occ. |
|---|---|---|---|---|---|---|---|
| Ba1 | 0.47623(6) | 0.52377(6) | 0.08614(3) | 0.0192(3) | 1 | 0.0195(2) | 1 |
| Cu1 | 0.2299(5) | 0.0171(3) | 0.1367(1) | 0.054(2) | 0.66(1) | 0.064(1) | 0.476(6) |
| Cu2 | 0.4317(2) | 0.5682(2) | 0.3509(1) | 0.042(1) | 0.97(1) | 0.0333(5) | 0.976(7) |
| Cu3 | 0.5310(1) | 0.4691(1) | 0.27998(8) | 0.0243(9) | 0.87(1) | 0.0221(6) | 0.663(6) |
| Cu4 | 0.5494(2) | 0.4506(2) | 0.3826(2) | 0.047(2) | 0.74(1) | 0.061(2) | 0.552(8) |
| Cu5 | 0 | 0 | 0.1713(4) | 0.058(6) | 0.41(2) | 0.28(2) | 0.28(2) |
| Cu6 | 0 | 0 | 0.2638(3) | 0.035(3) | 0.65(2) | 0.033(1) | 0.68(1) |
| Cu7 | 0.0699(8) | 0.1399(2) | 0.1566(6) | 0.138(9) | 0.26(1) | 0.038(1) | 0.448(7) |
| Cu8 | 0.380(1) | 0 | 0.5 | 0.10(2) | 0.21(2) | 0.032(2) | 0.339(7) |
| Cu9 | 0.440(8) | 0.341(4) | 0.4140(2) | 0.138(7) | 0.067(8) | 0.0231(9) | 0.309(4) |
| Q1(Se, Te) | 0.77642(7) | 0.22358(7) | 0.11211(5) | 0.0150(4) | 0.69(2), 0.31(2) | 0.0159(3) | 0.67(1), 0.33(1) |
| Te2 | 0 | 0 | 0.07952(7) | 0.0187(4) | 1 | 0.0160(2) | 1 |
| Se3 | 0.31791(1) | 0 | 0 | 0.0143(4) | 1 | 0.0138(2) | 1 |
| Q4(Se, Te) | 0 | 0 | 0.3573(1) | 0.019(1) | 0.92(3), 0.08(3) | 0.0168(5) | 0.97(2), 0.03(2) |
| Se5 | 0.47824(9) | 0.52176(9) | 0.20428(6) | 0.0205(4) | 1 | 0.0181(2) | 1 |

$Ba_3Cu_{16-x}Se_{11-y}Te_y$, is composed of the three-dimensional Cu clusters and the Cu deficient sites (Figure 3.4). The occupancy of three sites out of the nine occupied sites denoted as Cu7, Cu8 and Cu9, are 26%, 21%, and 7% before the electrical transport property measurements and 45%, 34%, and 31% after the measurements, respectively.

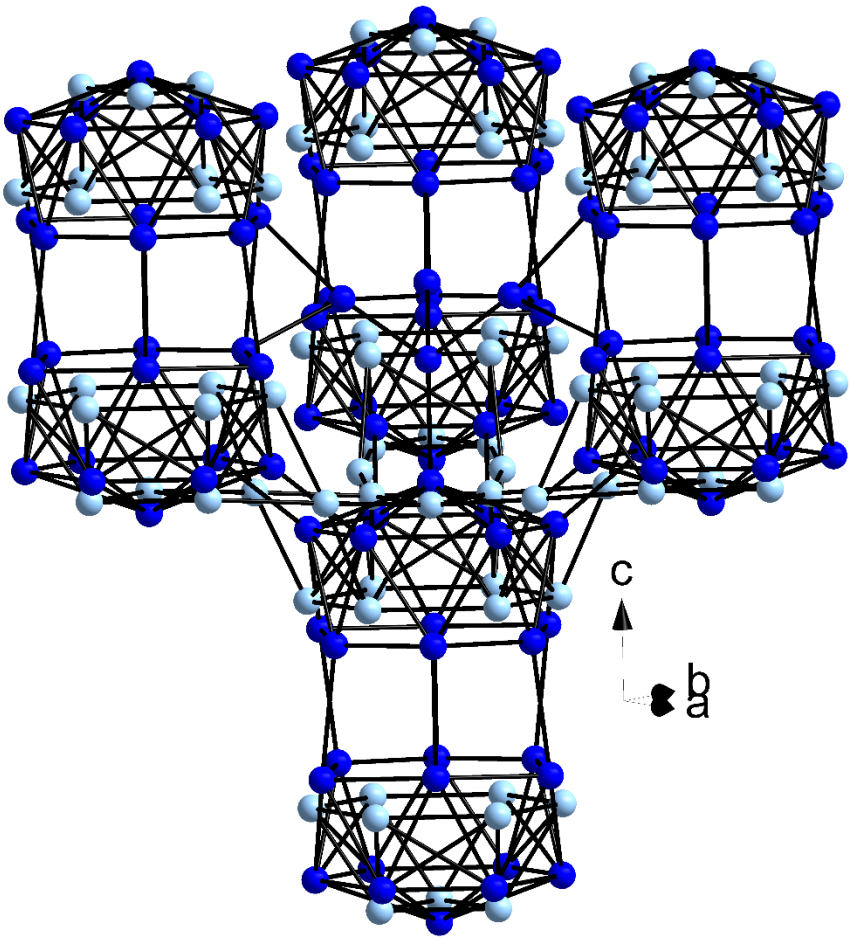


Figure 3.4 Three-dimensional network of Cu clusters in the structure of $Ba_3Cu_{16-x}Se_{11-y}Te_y$. Cu7, Cu8 and Cu9 are in bright blue, and the other Cu sites in dark blue.

### 3.3.2 Thermoelectric Properties

The temperature dependent electrical conductivity, $\sigma$, of the measured samples, (x = 1.3, 1.6 and y = 2.5, 3) upon heating and cooling is shown in Figure 3.5. As can be seen in all heating measurement plots, $\sigma$ initially decreases with increasing temperature. This behavior is typical for extrinsic semiconductors, caused by the decrease in electron mobility, $\mu$, with

increasing temperature, while the (extrinsic) carrier concentration remains largely unchanged. $\sigma$ then begins to increase around 580 K – 600 K, potentially because of the change in the occupancies of the Cu atom sites. With the estimated relative error of ±5%, samples with the same amount of y exhibit the same $\sigma$ within the measured temperature range. This can be explained by the different covalent character; the higher covalency of the Ba–Te and Cu–Te bonds as compared to Ba–Se and Cu–Se occurs with a higher carrier mobility for the materials with higher Te concentration. Correspondingly, the $\sigma$ values for the samples with x = 1.6 and y = 3 (*i.e.*, 3 Te per formula unit) range from 385 $\Omega^{-1}cm^{-1}$ at 299 K to 280 $\Omega^{-1}cm^{-1}$ at 695 K, while the ones with y = 2.5 vary from 338 $\Omega^{-1}cm^{-1}$ to 264 $\Omega^{-1}cm^{-1}$.

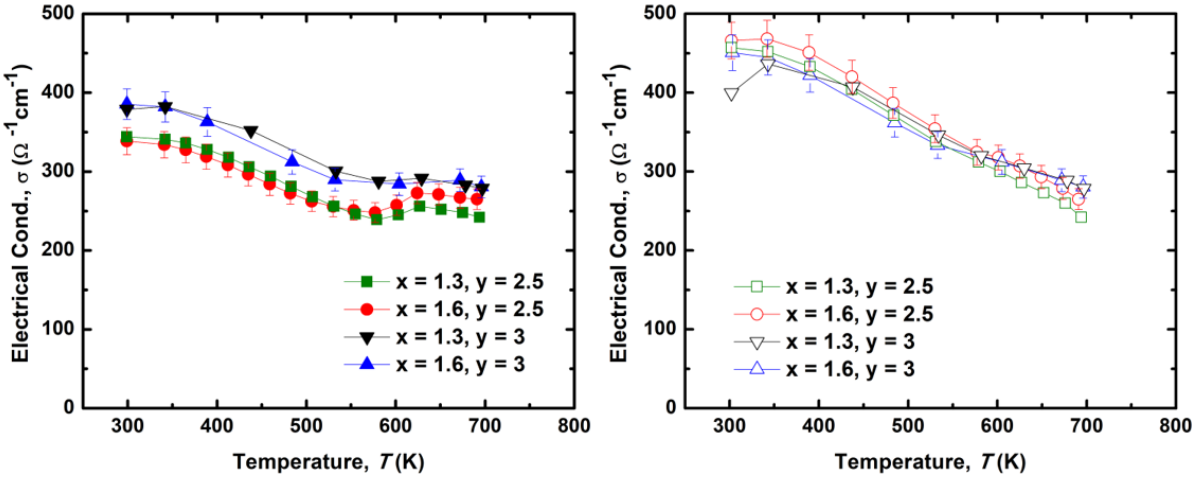


Figure 3.5 Electrical conductivity of the heating (left) and cooling (right) measurements of $Ba_3Cu_{16-x}Se_{11-y}Te_y$ in dependence on temperature.

The measurements result in different values when repeated. In all the measured cases, cooling (open symbols) yields larger values of $\sigma$ compared to heating (closed symbols). Larger mismatch between the heating and cooling data up to ~ 40% can be observed at lower temperatures. The measured electrical conductivity of the cooling process constantly decreases with increasing temperature with a maximum of 466 $\Omega^{-1}cm^{-1}$ for $Ba_3Cu_{14.4}Se_{8.5}Te_{2.5}$ at 300 K and a minimum of 242 $\Omega^{-1}cm^{-1}$ for $Ba_3Cu_{14.7}Se_{8.5}Te_{2.5}$ at 695 K. The larger electrical conductivity during the cooling measurement compared to the numbers at the same temperatures during heating is likely a consequence of Cu ion movement causing irreversible changes in this material, as also observed in the cases of $Cu_2S$ and $Cu_2Se$.

To investigate whether the electrical conductivity would continue to change from measurement to measurement, we repeated these electrical transport measurements twice in case of $Ba_3Cu_{14.7}Se_{8.5}Te_{2.5}$. The electrical conductivity values did not change noticeably after the first measurement (Figure 3.6), indicating that a steady state was reached, and the materials remain stable after the first cycle.

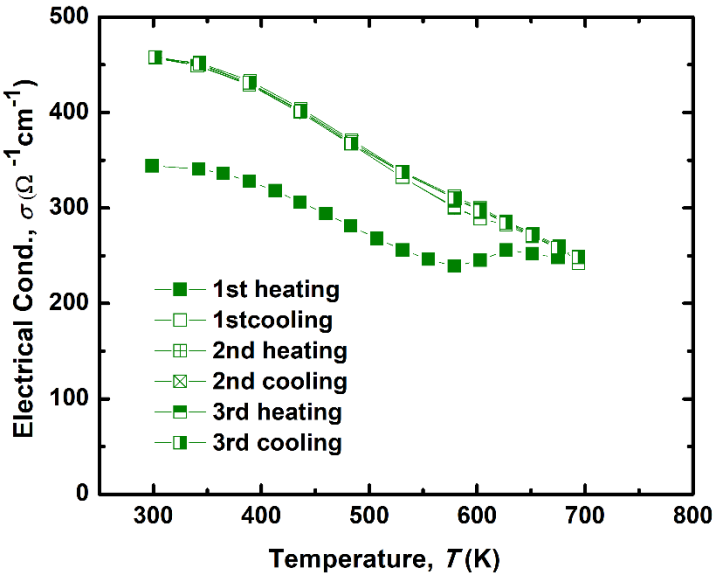


Figure 3.6 Repeat measurements of the temperature dependent electrical conductivity of $Ba_3Cu_{14.7}Se_{8.5}Te_{2.5}$.

However, in some cases, the steady state was reached later, *e.g.* after three or four cycles, or not at all during the first four cycles, as demonstrated for the slightly more Te-rich $Ba_3Cu_{14.7}Se_{8.2}Te_{2.8}$ (Figure 3.7).

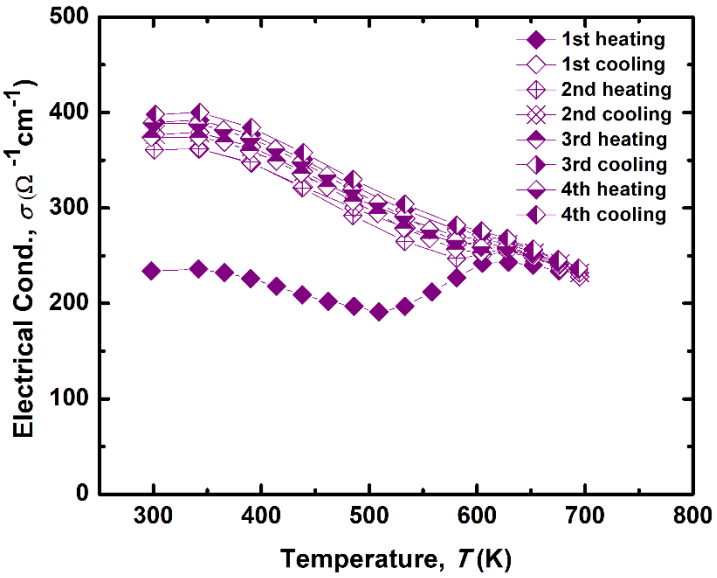


Figure 3.7 Repeat measurements of the temperature dependent electrical conductivity of $Ba_3Cu_{14.7}Se_{8.2}Te_{2.8}$.

In order to investigate whether this is an annealing effect, a hot-pressed bar of a sample of nominal composition $Ba_3Cu_{14.4}Se_{8.5}Te_{2.5}$ was annealed for three weeks prior to any physical property measurements at 700 K. Similar to the data before annealing, the electrical transport properties after three weeks of annealing revealed a lack of stability after the first heating measurement (Figure 3.8). The electrical conductivity at 300 K was measured to be 334 $\Omega^{-1}cm^{-1}$ at the beginning and 384 $\Omega^{-1}cm^{-1}$ at the end of the first measurement cycle, corresponding to an increase of 15%. This implies that the larger electrical conductivity after the first heating is not simply a consequence of an annealing effect, but caused by the measurement conditions, *i.e*. either by the voltage or the temperature gradient.

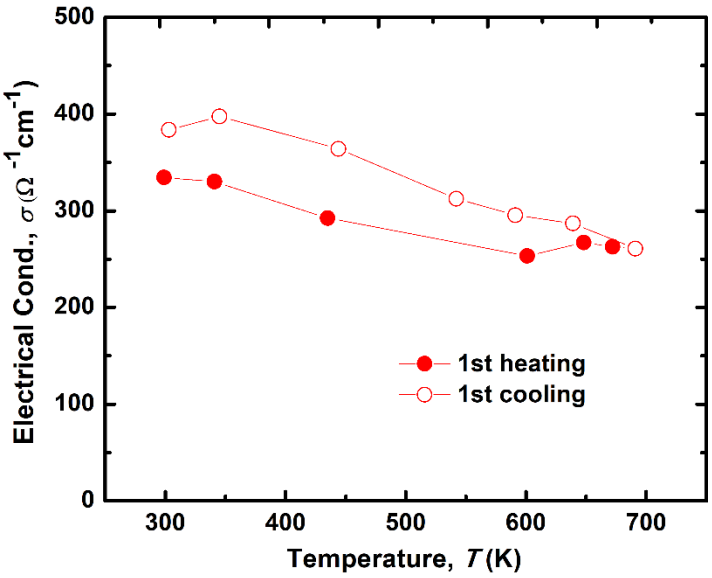


Figure 3.8 Temperature dependent electrical conductivity of $Ba_3Cu_{14.4}Se_{8.5}Te_{2.5}$ after annealing for three weeks before the measurement.

To investigate the cause for the variation of the $\sigma$ values during these measurements, room temperature Hall measurements were done on the samples of $Ba_3Cu_{14.4}Se_{8.5}Te_{2.5}$ and $Ba_3Cu_{14.4}Se_8Te_3$. In each case, two different bars from the same hot-pressed pellet were measured. The Hall measurement on the first bar was done directly after hot-pressing, while the second bar was measured after the electrical transport property measurements. The positive $R_H$ in all cases is indicative of the *p*-type semiconducting behavior of these materials with holes as dominant charge carriers. The electrical conductivity values increased from 325 $\Omega^{-1}cm^{-1}$ to 456 $\Omega^{-1}cm^{-1}$ for $Ba_3Cu_{14.4}Se_{8.5}Te_{2.5}$ and from 370 $\Omega^{-1}cm^{-1}$ to 449 $\Omega^{-1}cm^{-1}$ for $Ba_3Cu_{14.4}Se_8Te_3$, *i.e.*, by 40% and 21%, respectively, comparing the data from before and after the property measurements. This compares well with the data from the ZEM apparatus: there,

the room temperature electrical conductivity of these samples increased from 338 $\Omega^{-1}cm^{-1}$ to 466 $\Omega^{-1}cm^{-1}$ for $Ba_3Cu_{14.4}Se_{8.5}Te_{2.5}$ and from 385 $\Omega^{-1}cm^{-1}$ to 451 $\Omega^{-1}cm^{-1}$ for $Ba_3Cu_{14.4}Se_8Te_3$ at the beginning vs. the end of the first measurement cycle (*i.e.*, by 38% and 17%).

The charge carrier concentrations increased also, namely from $3.3 \times 10^{20}$ $cm^{-3}$ to $4.0 \times 10^{20}$ $cm^{-3}$ for $Ba_3Cu_{14.4}Se_{8.5}Te_{2.5}$, and from $3.2 \times 10^{20}$ $cm^{-3}$ to $4.7 \times 10^{20}$ $cm^{-3}$ for $Ba_3Cu_{14.4}Se_8Te_3$, respectively. On the other hand, the carrier mobility changed differently in the two samples, with one increasing from 6.4 $cm^2V^{-1}s^{-1}$ to 7.3 $cm^2V^{-1}s^{-1}$ ($Ba_3Cu_{14.4}Se_{8.5}Te_{2.5}$), and one decreasing from 7.5 $cm^2V^{-1}s^{-1}$ to 6.0 $cm^2V^{-1}s^{-1}$ ($Ba_3Cu_{14.4}Se_8Te_3$). The latter may be a consequence of the more significantly increased carrier concentration resulting in enhanced carrier-carrier scattering.

The temperature dependences of the Seebeck coefficient, $\alpha$, of the measured samples are depicted in Figure 3.9. The general increase of the positive Seebeck coefficient values through the entire temperature range is indicative of heavily doped *p*-type semiconductors. As in case of the electrical conductivity, the cooling data differ from the heating data. For instance, the $\alpha$ values for the first heating measurement of $Ba_3Cu_{14.7}Se_{8.5}Te_{2.5}$ range from 65 $\mu V\ K^{-1}$ at 300 K to 136 $\mu V\ K^{-1}$ at 695 K, while the $\alpha$ value measured during cooling is 55 $\mu V\ K^{-1}$ at 300 K, corresponding to a decrease of 18%. It is noted that these changes generally appear to be relatively smaller than in case of the electrical conductivity.

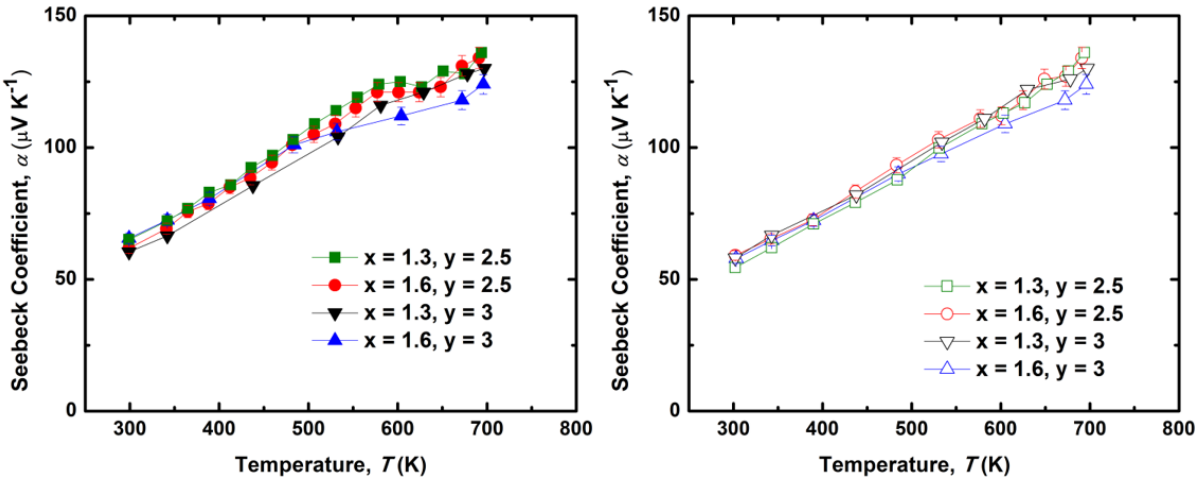


Figure 3.9 Seebeck coefficient of the heating (left) and cooling (right) measurements of $Ba_3Cu_{16-x}Se_{11-y}Te_y$ in dependence on temperature.

The heating and cooling measurements repeated for two more times revealed no more noticeable changes, as was also observed in case of the electrical conductivity (Figure 3.10).

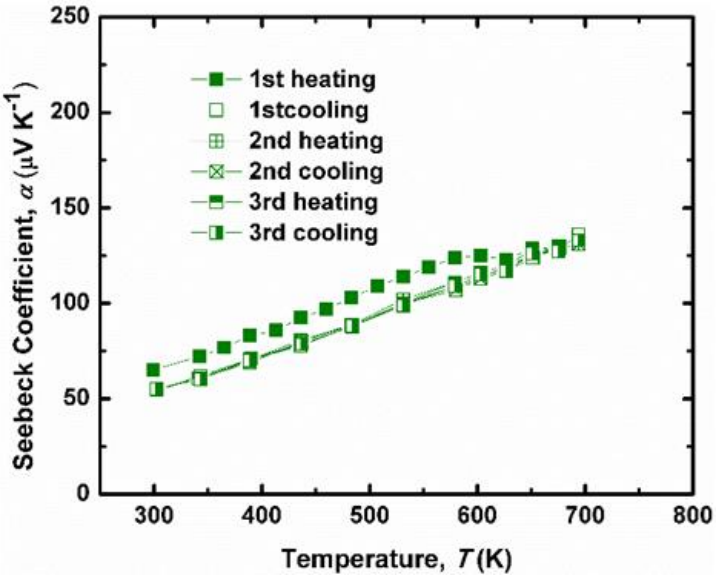


Figure 3.10 Repeat measurements of the temperature dependent Seebeck coefficient of $Ba_3Cu_{14.7}Se_{8.5}Te_{2.5}$.

As was observed for the repeating electrical conductivity of $Ba_3Cu_{14.7}Se_{8.2}Te_{2.8}$, the steady state was reached later for the Seebeck measurements (Figure 3.11)

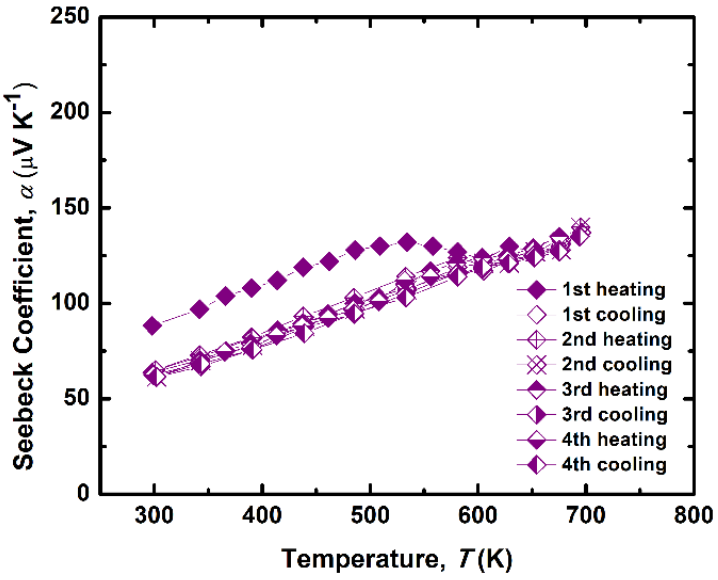


Figure 3.11 Repeat measurements of the temperature dependent Seebeck coefficient of $Ba_3Cu_{14.7}Se_{8.2}Te_{2.8}$.

In order to investigate the stability range of $Ba_3Cu_{16-x}Se_{11-y}Te_y$, different current densities and maximum temperatures were applied during the electrical transport measurements. For this purpose, a 4 gram sample of $Ba_3Cu_{14.7}Se_{8.5}Te_{2.5}$ was prepared, consolidated into a pellet, then cut into several bars. During the measurements, the current flow alternated direction; however, using a fixed current flow from top to bottom resulted in qualitatively equivalent data. During the Seebeck measurement, the applied temperature gradient always went from bottom to top, with a maximum $\Delta T$ = 4 K. As a starting point, the same conditions as for the data shown in Figure 3.5 ($J$ = 0.084 A cm$^{-2}$) were applied. With the same maximum temperature but a lower current density of $J$ = 0.024 A cm$^{-2}$ at room temperature, a similar lack of stability was still observed. Lowering the maximum temperature

to 630 K with the same current density of 0.024 A $cm^{-2}$ still did not readily result in reproducible data, not even with a lower current density of 0.005 A $cm^{-2}$. When decreasing the maximum temperature to 580 K and using that low current density, reproducible data were finally obtained (Figure 3.12), likely because the Cu atom mobility is significantly less at 580 K than at 630 K, let alone at 690 K. This is a consequence of the thermal activation of the Cu atom mobility. We note that 580 K is the temperature where the first irregularities occurred during the electrical conductivity measurements described above. The different applied conditions for evaluating the stability of these materials are listed in Table 3.3.

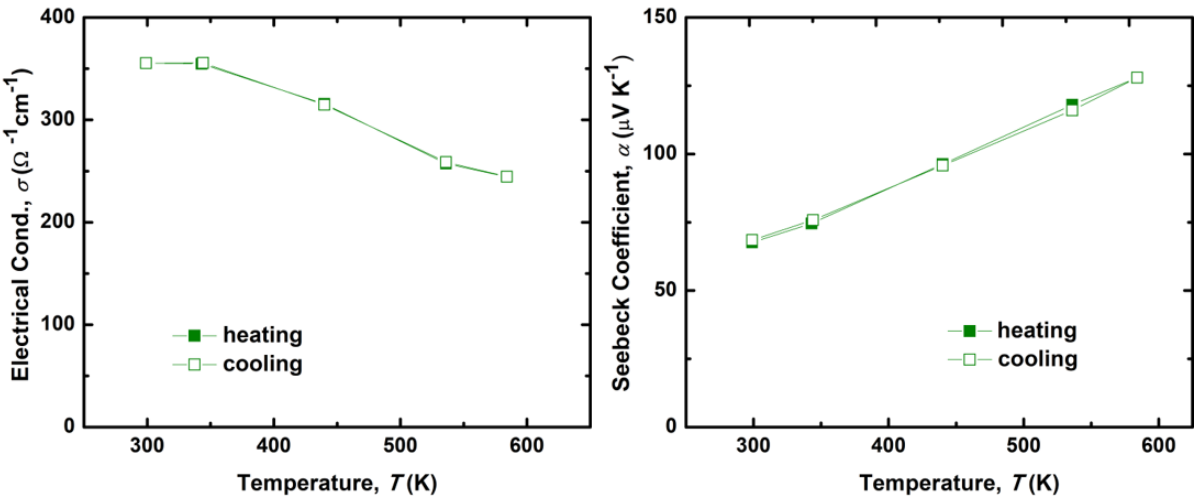


Figure 3.12 Stability of the electrical transport properties of $Ba_3Cu_{14.7}Se_{8.5}Te_{2.5}$.

Table 3.3 Different applied conditions to investigate the stability of $Ba_3Cu_{14.7}Se_{8.5}Te_{2.5}$.

| Chemical formula | $T_{max}$ (K) | $J$ (A cm$^{-2}$) |
|---|---|---|
| $Ba_3Cu_{14.7}Se_{8.5}Te_{2.5}$ | 690 | 0.084 |
| $Ba_3Cu_{14.7}Se_{8.5}Te_{2.5}$ | 690 | 0.024 |
| $Ba_3Cu_{14.7}Se_{8.5}Te_{2.5}$ | 630 | 0.024 |
| $Ba_3Cu_{14.7}Se_{8.5}Te_{2.5}$ | 630 | 0.005 |
| $Ba_3Cu_{14.7}Se_{8.5}Te_{2.5}$ | 580 | 0.005 |

In order to see whether an irreversible Cu ion movement occurred during the measurements, the elemental atomic-% of Cu after three measurements of a bar of nominal composition $Ba_3Cu_{14.7}Se_{8.5}Te_{2.5}$ with a maximum measured temperature of 690 K and $J$ = 0.084 A cm$^{-2}$ was determined at two different locations *via* SEM/EDX measurements. The bottom of the bar, which was closer to the heater and thus warmer, showed 44 atomic-% for copper, while the top of the bar had 50 at-% of copper. This gradient implies an in part irreproducible movement of Cu ions from the bottom to the top of the bar, which corresponds to a movement from the hot to the cold side during the Seebeck measurement (while the current direction alternated).

Additionally, we performed a PSM measurement on a bar of nominal composition $Ba_3Cu_{14.7}Se_{8.2}Te_{2.8}$, using a $\Delta T$ = 5 K at room temperature, which underwent an electrical transport property measurement using the HT-S-σ setup at DLR.[143] This measurement also revealed inhomogeneities in accord with the changes in Cu concentration (Figure 3.13).

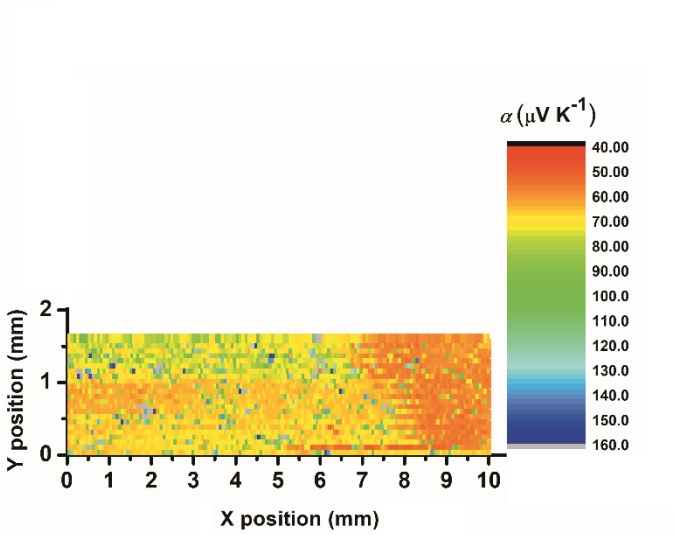


Figure 3.13 Spatial resolution of the Seebeck coefficient of $Ba_3Cu_{14.7}Se_{8.2}Te_{2.8}$.

The thermal conductivity, $\kappa$, data of the measured samples for both heating and cooling process are depicted in Figure 3.14. In both cases, the thermal conductivity values of all samples are rather low ($\kappa$ < 0.8 W $m^{-1}K^{-1}$). $\kappa$ shows an increase at lower temperatures of the cooling measurement compared to that temperature in the heating process. For example, in $Ba_3Cu_{14.7}Se_{8.5}Te_{2.5}$, the room temperature value of the first heating measurement is 0.64 W $m^{-1}K^{-1}$, and 0.69 W $m^{-1}K^{-1}$ after cooling, corresponding to a relatively small increase of 8%, compared to the changes in the electrical properties.

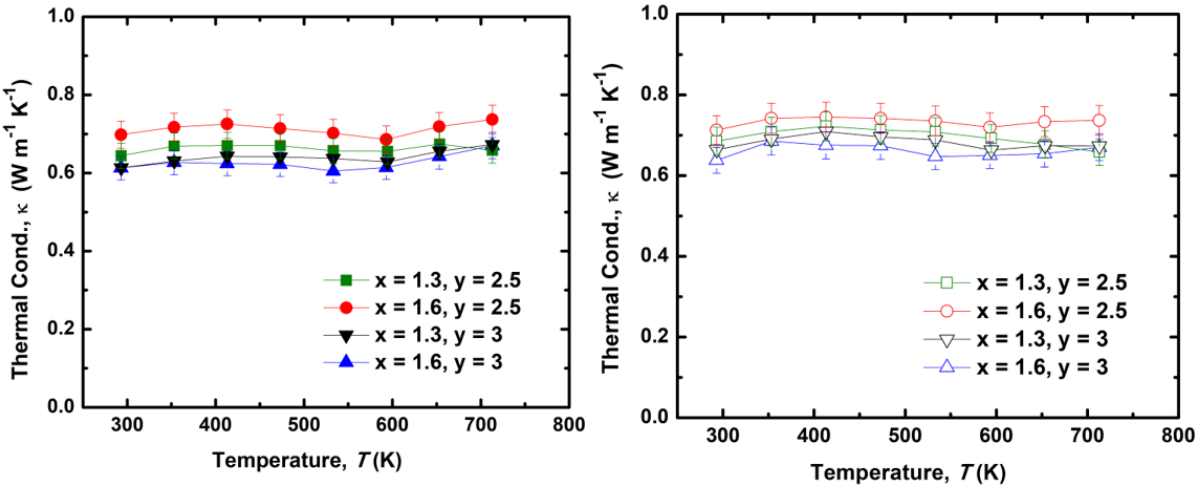


Figure 3.14 Thermal conductivity of the heating (left) and cooling (right) measurements of $Ba_3Cu_{16-x}Se_{11-y}Te_y$ in dependence on temperature.

A lack of stability – albeit with a smaller change – is thus also observed during the thermal diffusivity measurements, as a noticeable temperature gradient is also applied in the flash method. As in case of the electrical data, repeated cycling leads sooner or later to reproducible values (Figure 3.15).

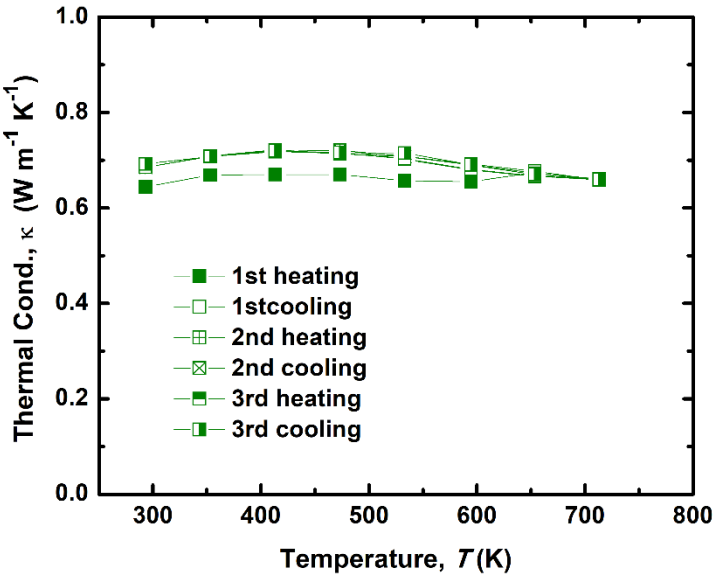


Figure 3.15 Repeat measurements of the temperature dependent thermal conductivity of $Ba_3Cu_{14.7}Se_{8.5}Te_{2.5}$.

Samples with the larger amount of Te atoms exhibit lower $\kappa$, with the same values within experimental error for $Ba_3Cu_{14.4}Se_8Te_3$ and $Ba_3Cu_{14.7}Se_8Te_3$, with $\kappa$ = 0.61 W $m^{-1}K^{-1}$ at the beginning of the data collection. This observation is in correlation with the larger mass fluctuation for the samples with the larger Te concentration.

The lower thermal conductivity of these materials is comparable with some of the well-known materials with low lattice thermal conductivity at elevated temperatures up to 800 K. Some of these materials include $Ag_nPb_mM_nTe_{m+2n}$ ($M$ = Sb or Bi) and more specifically $AgPb_{10}SbTe_{12}$ ($\kappa_L$ ~ 1 W $m^{-1}K^{-1}$ at 650 K),[62] the filled skutterudites,[153] $\beta$-Zn4Sb3[39,154] and $Ag_2Te$.[155]

As discussed in the introduction, the thermal conductivity, $\kappa$, is the sum of the electronic thermal conductivity, $\kappa_e$, and the lattice thermal conductivity, $\kappa_L$. To gain further insight into the effect of the mass fluctuation on the lattice thermal conductivity, $\kappa_L$, was calculated *via* $\kappa_L = \kappa - \kappa_e$. Here, $\kappa_e$ was estimated from the Wiedemann-Franz law, $\kappa_e = L\sigma T$. The Lorenz number $L$ was computed by applying the proposed Equation 3.1 under the assumption of acoustic phonons, which was reported to be in good agreement with the single parabolic band (SPB) model.[156]

$$L = (1.5 + \exp\left[\frac{-|\alpha|}{116\mu V/K}\right])\ 10^{-8}\ V^2K^{-2} \qquad (3.1)$$

We refrained from calculating $\kappa_e$ from the cooling data, as the electrical conductivity changed more significantly than the thermal data. Therefore, only the heating data can be provided for the lattice thermal conductivity (Figure 3.16).

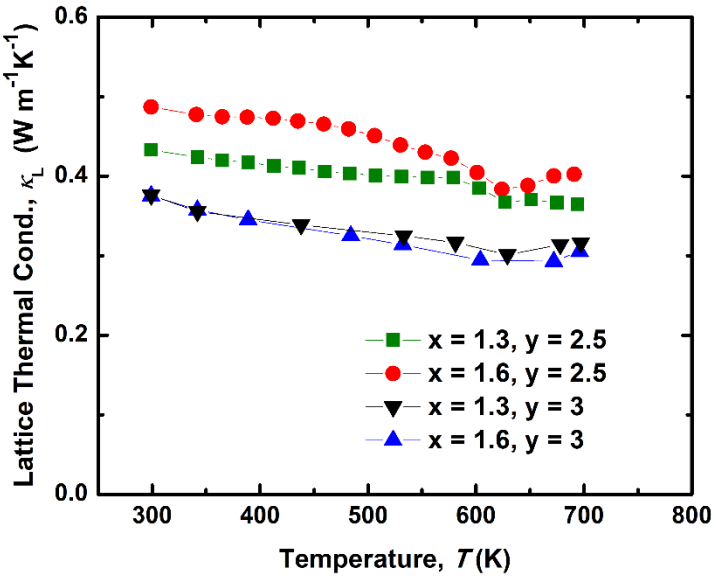


Figure 3.16 Lattice thermal conductivity of the heating measurements of $Ba_3Cu_{16-x}Se_{11-y}Te_y$ in dependence on temperature.

Consistently, all samples possess very low $\kappa_L$ values, namely below 0.6 W m$^{-1}$K$^{-1}$. Samples with the larger mass fluctuation showed similar values to each other, and lower values than the other measured samples (*e.g.*, 0.38 W m$^{-1}$K$^{-1}$ at 299 K and 0.31 W m$^{-1}$K$^{-1}$ for x = 1.6 and y = 3). Since $\kappa_L$ is calculated from $\kappa_L = \kappa - \kappa_e$, *i.e.* from two experimentally determined properties with errors of 5% or higher, the almost 10% difference between the calculated lattice thermal conductivity of $Ba_3Cu_{14.4}Se_{8.5}Te_{2.5}$ and $Ba_3Cu_{14.7}Se_{8.5}Te_{2.5}$ is at the border of significance.

Ultimately, the figure-of-merit was obtained from the fit of the power factor, $\alpha^2\sigma$, and the measured thermal conductivity values. It should be noted that a $zT$ calculation here has an additional error arising from the different changes in the electrical properties, compared to the

thermal ones. An overall increase in the *zT* curves was observed in the entire measured temperature range for both heating and cooling measured values, caused by generally decreasing electrical conductivity and increasing Seebeck coefficient with temperature, and a mostly temperature independent thermal conductivity. The maximum computed *zT* value is obtained for $Ba_3Cu_{14.7}Se_8Te_3$ with $zT = 0.49$ at 695 K, while the other samples' $zT_{max}$ values are equivalent within ±10% error (Figure 3.17).

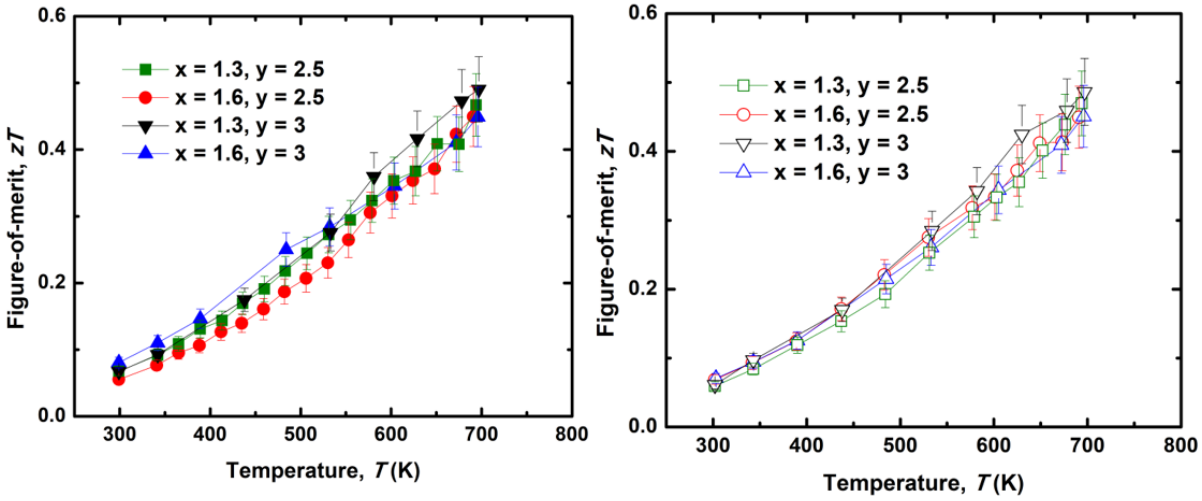


Figure 3.17 Thermoelectric figure-of-merit *zT* of the heating (left) and cooling (right) measurements of $Ba_3Cu_{16-x}Se_{11-y}Te_y$ in dependence on temperature.

## 3.4 Conclusions

Polycrystalline copper chalcogenides, $Ba_3Cu_{16-x}Se_{11-y}Te_y$ (x = 1.3, 1.6 and y = 2.5, 2.8 and 3), have been synthesized. The physical properties of the hot-pressed samples with relative densities of almost 100% of the theoretical maximal values were determined. A lack of stability

of the transport properties when measured up to 630 K or higher was observed. Limiting the measurements of the electrical transport properties up to 580 K revealed a good stability of these materials.

Based on room temperature X-ray single crystal data, the distribution of the Cu atoms across the nine Cu sites changed during the electrical property measurements, which is indicative of an irreversible Cu ion movement during these measurements. The irreversible Cu ion movement was verified after the electrical property measurements through SEM/EDX measurements. The 6% difference between the at-% of copper of the bottom and top of the measured bar corresponds to a movement of Cu ions from the hot end to the cold end due to the temperature gradient during the Seebeck measurement. As a result of the irreversible Cu ion movement in these materials, the electrical conductivity and the Seebeck coefficient of the first cooling measurement compared to the same temperature during the first heating exhibited larger and smaller values, respectively. Ultimately, after the first measurement cycle of $Ba_3Cu_{14.7}Se_{8.5}Te_{2.5}$, and in some cases later, a steady state was reached, meaning the electrical properties remained unchanged during subsequent measurements. Similarly, a lack of stability was observed during the thermal diffusivity measurements, as a noticeable temperature gradient was also applied in the flash method.

Finally, the calculated dimensionless thermoelectric figure-of-merit values range from $zT = 0.44$ to $zT = 0.49$ for all the measured samples around 690 K. As a result, $Ba_3Cu_{16-x}Se_{11-y}Te_y$ is not suggested to be used in thermoelectric devices.

# 4. Thermoelectric Properties of $Ba_3Cu_{16-x}S_{11-y}Te_y$

## 4.1 Introduction

The quaternary copper chalcogenides studied in this chapter, $Ba_3Cu_{16-x}S_{11-y}Te_y$, crystallize in either a rhombohedral or a cubic structure. The S/Te ratio dictates either a rhombohedral or a cubic symmetry. In order for the rhombohedral variants of $Ba_3Cu_{16-x}S_{11-y}Te_y$ to form, y must be smaller than 5.5.[157] Here we analyze only the rhombohedral samples, as the cubic ones exhibited less promise due to their low Seebeck coefficient.

Prior to the presented work, the cold-pressed $Ba_3Cu_{16}S_9Te_2$ with an experimental density of 85% of the theoretical density showed an electrical conductivity of 20 $\Omega^{-1}cm^{-1}$ at room temperature, which increased with temperature as expected for slightly doped semiconductors, to reach 163 $\Omega^{-1}cm^{-1}$ at 700 K. Thermal conductivity was not determined, and Seebeck values exhibited an overall decrease from +226 $\mu$V $K^{-1}$ at room temperature to +166 $\mu$V $K^{-1}$ at 700 K, indicative of predominantly *p*-type conduction.[157]

Aiming to achieve higher efficiency of these narrow band gap *p*-type semiconductors, some parameters needed to be modified. In this regard, lowering the Cu content in order to increase the Cu deficiency and thus the charge carrier concentration was considered. Additionally, we improved the relative density of the $Ba_3Cu_{16-x}S_{11-y}Te_y$ to almost 100%

through hot-pressing. Thermoelectric properties of these materials, along with first stability studies are discussed in this chapter, and was published in 2018.[158]

## 4.2 Experimental Procedure

All compounds were synthesized from the elements (Ba pieces, 99.7%, Strem Chemicals; Cu powder, 99.5%, Alfa Aesar; S flakes, 99.8%, Aldrich; Te broken ingots, 99.99%, Strem Chemicals) in C-coated silica tubes, evacuated and placed in programmable furnaces. Trying different conditions of synthesis in order to shorten the reaction time always resulted in side products, mainly the binaries of Cu chalcogenides. Only solid-state reactions with slow cooling resulted in pure compounds.[157] Therefore, evacuated tubes were heated up to 1023 K in 12 hours, then the furnace was cooled down to 873 K in 20 hours, followed by annealing for 100 hours at 873 K and lastly cooling to room temperature.

Phase purity of the synthesized compounds (x = 0.7, 0.9 and y = 2, 2.5, 3.5) was checked *via* powder X-ray diffraction at room temperature. Figure 4.1 confirms that phase pure samples were obtained.

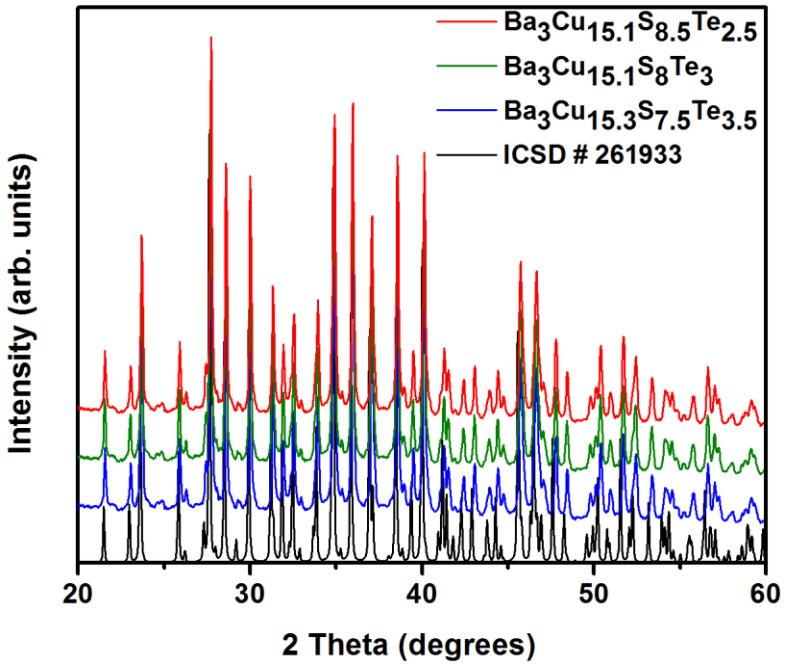


Figure 4.1 Room temperature powder XRD patterns of $Ba_3Cu_{16-x}S_{11-y}Te_y$.

These phase pure samples were pelletized through hot-pressing at an applied pressure of 60 MPa and a dwell temperature of 800 K for 2 hours, which led to an almost 100% density.

Electrical properties were measured perpendicular to the pressing direction, whereas thermal conductivity was measured parallel to it. To check whether the properties are isotropic, as may be expected based on the three-dimensional crystal structure despite the rhombohedral symmetry, we measured the electrical conductivity on the same selected bar both parallel and perpendicular to the pressing direction. The results were equivalent within experimental error. For instance, for a measured bar of $Ba_3Cu_{15.1}S_{8.5}Te_{2.5}$, the values of the electrical conductivity for perpendicular and parallel directions at room temperature were 120 $\Omega^{-1}cm^{-1}$ and 130

$\Omega^{-1}cm^{-1}$ respectively. To measure the parallel electrical conductivity a four-probe home-made setup based on a Keithy 2400 sourcemeter was used while the electrical property on a perpendicular direction was measured by ULVAC-ZEM-3 instrument. The 7% difference between the electrical property measurements at 302 K may rise from the different dimensions of the samples and different probe distances between the two measured samples.

The homogeneity of the samples was investigated through SEM/EDX on the surface of the pellets after hot-pressing. An applied acceleration voltage of 20 kV was used to determine the concentration as well as the distribution of the elements on five different areas of the pellet. For instance, the determined atomic ratio of Ba : Cu : S : Te in $Ba_3Cu_{15.1}S_8Te_3$ was as follows: 10.6(4) : 50(2) : 27(2) : 10.0(2). These elemental percentages are in a reasonable agreement with the expected theoretical values of 10.3 : 51.9 : 27.5 : 10.3. The EDX results confirmed that the hot-press and property measurement conditions did not cause any noticeable decay such as loss of sulfur during the process of heating up the samples. Figure 4.2 demonstrates the homogeneous distribution of the elements.

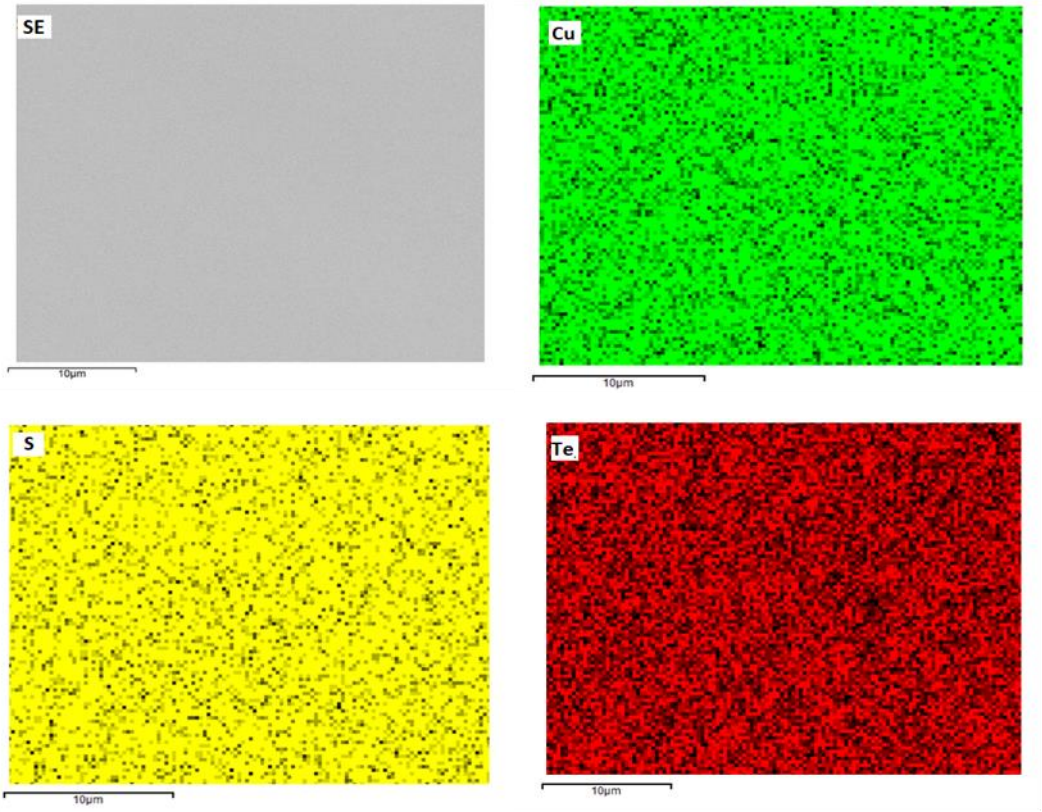


Figure 4.2 EDX maps of $Ba_3Cu_{15.1}S_8Te_3$. Top left: secondary electron image; top right: Cu map; bottom left: S map; bottom right: Te map.

Thermal stability of $Ba_3Cu_{15.3}S_{7.5}Te_{3.5}$ was investigated by combined DSC and TG under argon, with a heating rate of 10 K $min^{-1}$. No phase transitions were observed aside from melting at 970 K while heating and a delayed crystallization while heating. A small weight loss was noticeable above 800 K, restricting our property measurements to a maximum temperature of 750 K (Figure 4.3).

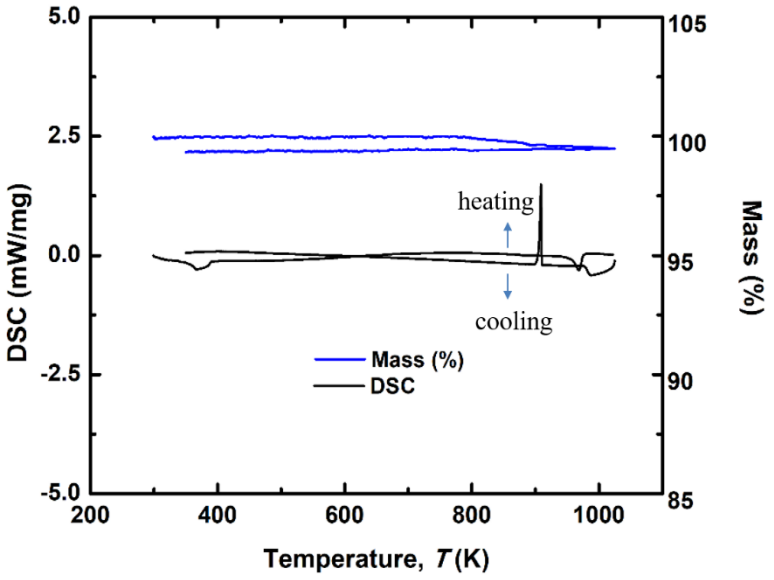


Figure 4.3 DSC/TG of $Ba_3Cu_{15.3}S_{7.5}Te_{3.5}$. (heating rate of 10 K $min^{-1}$ under Ar atmosphere).

## 4.3 Results and Discussion

### 4.3.1 Crystal Structure and Crystallographic Data

As is the case in the selenides, extended Cu–Cu contacts with different distances below 3 Å result in clusters of 26 Cu atoms in the structure of the sulfides with rhombohedral structure. These clusters are interconnected *via* $d^{10}$–$d^{10}$ nonclassical Cu–Cu bonds to a three-dimensional network (Figure 4.4).

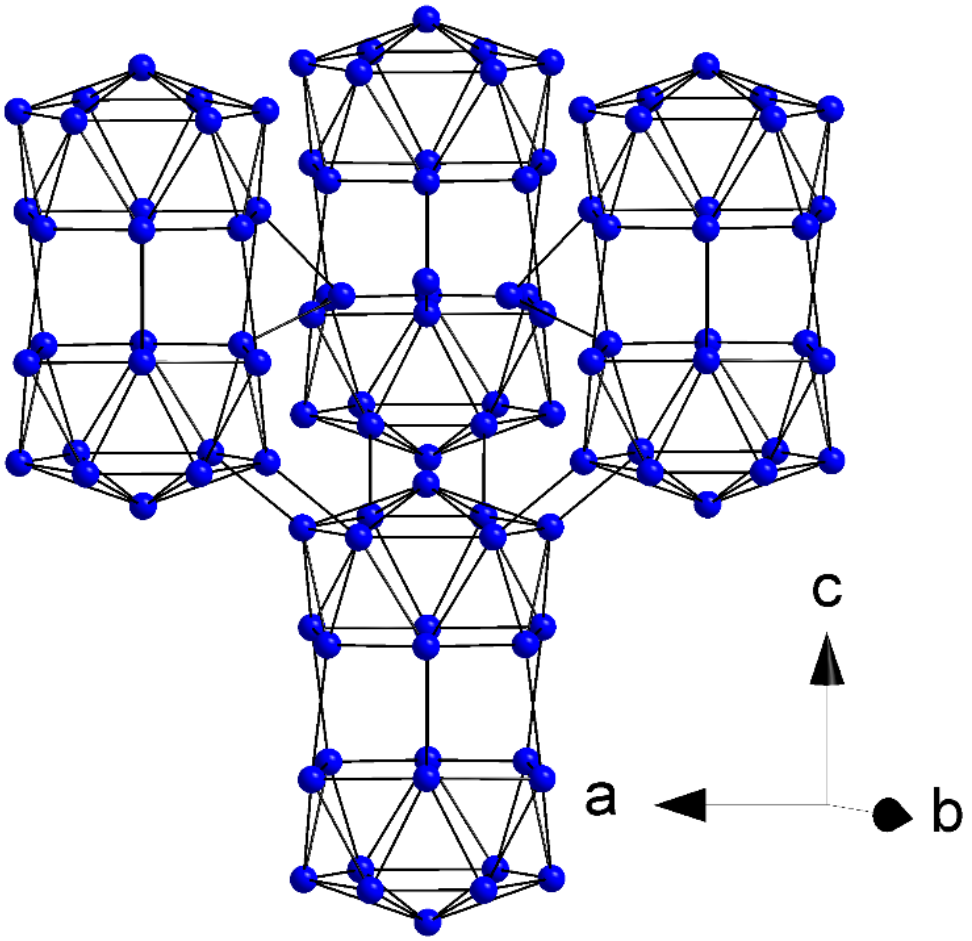


Figure 4.4 Three-dimensional network of $Cu_{26}$ clusters in the structure of $Ba_3Cu_{16-x}S_{11-y}Te_y$.

As was observed in the selenides, Cu deficient sites combined with the direct contacts between the Cu atoms might cause the Cu ions to be mobile throughout the whole material. However, X-ray single crystallography data from before and after the electrical property measurements confirmed the larger stability of the sulfides as compared to the selenides. As opposed to the selenides, discussed in chapter 3, the refinement of the sulfides was completed with six Cu sites (before and after the electrical transport property measurements). For

example, the completed refinement of the nominal composition of $Ba_3Cu_{15.1}S_{8.5}Te_{2.5}$ resulted in an acceptable $R(F_o) = 0.038$ and a maximum residual electron density of 4.3 e $Å^{-3}$. Therefore, fewer occupied sites result in a smaller disorder and a larger stability of the sulfides as compared to the selenides. The crystallographic information of the refinement of $Ba_3Cu_{15.1}S_{8.5}Te_{2.5}$ is exhibited in Table 4.1. Fractional atomic coordinates, equivalent isotropic displacement parameters and site occupancies for the data before and after the physical property measurements are illustrated in Table 4.2. This information is indicative of no considerable changes between the refined occupancies before and after the property measurements.

Table 4.1 Crystallographic details of the refinement of "$Ba_3Cu_{15.1}S_{8.5}Te_{2.5}$"; I) before hot pressing: II) after the electrical transport property measurements.

| Refined formula | I) $Ba_3Cu_{15.26(7)}S_{8.31(1)}Te_{2.69}$ | II) $Ba_3Cu_{15.38(7)}S_{8.35(1)}Te_{2.6}$ |
|---|---|---|
| Formula weight | 1991.67 | 1994.36 |
| $T$ [K] | 296(2) | 296(2) |
| λ [Å] | 0.71073 | 0.71073 |
| Crystal system | Rhombohedral | Rhombohedral |
| Space group | $R\bar{3}m$ (no. 166) | $R\bar{3}m$ (no. 166) |
| $a$, $c$ [Å] | 11.901(1), 27.433(2) | 11.899(2), 27.449(4) |
| $V$ [$Å^3$] | 3364.80(6) | 3365.5(1) |
| $Z$ | 6 | 6 |
| $R(Fo)$,[a] $R_w(Fo^2)$,[b] GOF (obs. data) | 0.037, 0.085, 1.04 | 0.038, 0.085, 1.04 |
| Min., max. residual electron density [e $Å^{-3}$] | -2.30, 4.48 | -2.29, 4.26 |

[a] $R(F_o) = \Sigma||F_o|-|F_c|| / \Sigma|F_o|$; [b] $R_w(F_o^2) = [\ \Sigma[w(F_o^2 - F_c^2)^2] / \Sigma[w(F_o^2)^2]\ ]^{1/2}$, with $F_o$ and $F_c$ being the observed and calculated structure factors, respectively.

Table 4.2 Fractional atomic coordinates and equivalent isotropic displacement parameters and occupancies of "$Ba_3Cu_{15.1}S_{8.5}Te_{2.5}$"; I) before hot pressing; II) after the electrical transport property measurements.

| | x | y | z | I) $U_{eq}$/Å$^2$ | I) occ. | II) $U_{eq}$/Å$^2$ | II) occ. |
|---|---|---|---|---|---|---|---|
| Ba1 | 0.47177(3) | 0.52823(3) | 0.08655(2) | 0.0161(2) | 1 | 0.0165(2) | 1 |
| Cu1 | 0.2325(2) | 0.01334(1) | 0.13515(6) | 0.0391(6) | 0.816(6) | 0.0414(7) | 0.816(7) |
| Cu1B | 0.0175(1) | 0.1548(9) | 0.1503(3) | 0.046(4) | 0.138(6) | 0.041(4) | 0.135(6) |
| Cu2 | 0.757(1) | 0.2429(1) | 0.01852(9) | 0.0586(9) | 0.945(9) | 0.060(1) | 0.968(9) |
| Cu3 | 0.52396(8) | 0.47604(8) | 0.28215(5) | 0.0243(5) | 0.996(7) | 0.0248(5) | 0.991(8) |
| Cu4 | 0.54640(9) | 0.45360(9) | 0.37995(6) | 0.0339(6) | 0.961(8) | 0.0348(7) | 0.970(8) |
| Cu5 | 0 | 0 | 0.1688(2) | 0.042(2) | 0.63(2) | 0.045(2) | 0.66(2) |
| Cu6 | 0 | 0 | 0.2327(6) | 0.033(5) | 0.20(1) | 0.035(5) | 0.23(1) |
| *Q1*(S, Te) | 0.77521(4) | 0.22479(4) | 0.11060(3) | 0.0124(3) | 0.435(6), 0.565(6) | 0.0129(3) | 0.451(6), 0.549(6) |
| Te2 | 0 | 0 | 0.07669(4) | 0.0168(2) | 1 | 0.0170(3) | 1 |
| S3 | 0.3197(2) | 0 | 0 | 0.0135(4) | 1 | 0.0144(5) | 1 |
| S4 | 0 | 0 | 0.3595(2) | 0.0162(8) | 1 | 0.0172(9) | 1 |
| S5 | 0.4781(1) | 0.5219(1) | 0.20550(8) | 0.0170(5) | 1 | 0.0180(5) | 1 |

### 4.3.2 Thermoelectric Properties

The physical properties of the phase pure samples were determined for x = 0.7 and 0.9 and y = 2.5, 3, and 3.5. The temperature dependence of the electrical conductivity, $\sigma$, is depicted in Figure 4.5. The measured samples have very comparable values, ranging from 120 $\Omega^{-1}cm^{-1}$ to 143 $\Omega^{-1}cm^{-1}$ at the lowest temperatures measured. At 690 K, $\sigma$ values are between 104 $\Omega^{-1}cm^{-1}$ and 131 $\Omega^{-1}cm^{-1}$, with the sample with the highest Te concentration, $Ba_3Cu_{15.3}S_{7.5}Te_{3.5}$, having the highest conductivity. As previously discussed for the selenides in chapter 3, this can be understood by the less ionic Ba–Te and Cu–Te interactions, compared

to Ba–S and Cu–S, resulting in higher mobility. The small differences in the nominal Cu deficiency appear to be negligible for the transport properties.

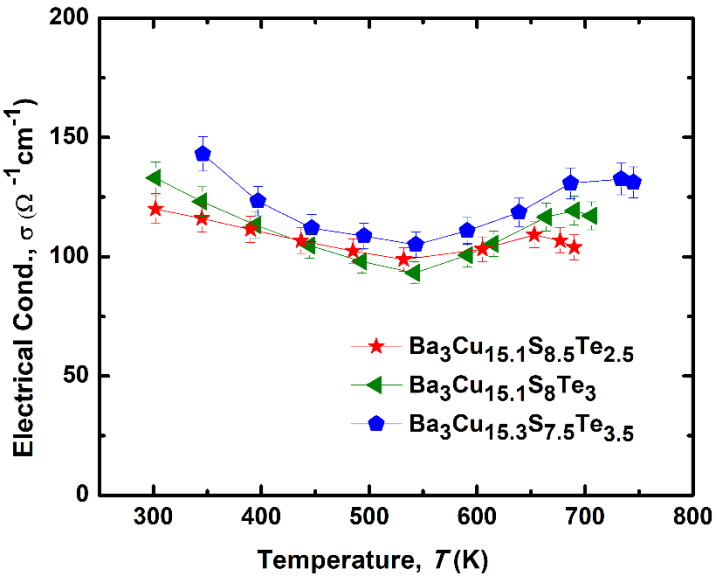


Figure 4.5 Temperature dependence of the electrical conductivity of $Ba_3Cu_{16-x}S_{11-y}Te_y$.

The temperature dependence of the electrical conductivity is typical for extrinsic semiconductors. Due to the proportionality of conductivity to the mobility, $\sigma$ decreases with temperature. On the other hand, the exponential increase of the intrinsic carrier concentration results in an enhancement of $\sigma$ with increasing temperature around 535 K. The increase in $\sigma$ after the turnaround around 535 K continues to 690 K for $Ba_3Cu_{15.1}S_8Te_3$ and to 653 K for $Ba_3Cu_{15.1}S_{8.5}Te_{2.5}$. However, after the mentioned temperatures, the last data point of $Ba_3Cu_{15.1}S_8Te_3$ and the last two data points of $Ba_3Cu_{15.1}S_{8.5}Te_{2.5}$ exhibit a slight decrease. This

may be due to these materials reaching the softening point, around 300 K below the melting point of 970 K.

The positive $\alpha$ values along with the (previously calculated) small band gap of 0.12 eV[157] suggest heavily doped *p*-type semiconducting behavior of this material (Figure 4.6). Similar to the calculated $\sigma$, the measured $\alpha$ is comparable for $Ba_3Cu_{15.1}S_8Te_3$ and $Ba_3Cu_{15.1}S_{8.5}Te_{2.5}$, with a maximal difference of 6%, which is equal to the sum of the estimated experimental errors. However, below 680 K, the measured $\alpha$ of the more Te-rich material, $Ba_3Cu_{15.3}S_{7.5}Te_{3.5}$ is consistently larger than $\alpha$ of the other two materials.

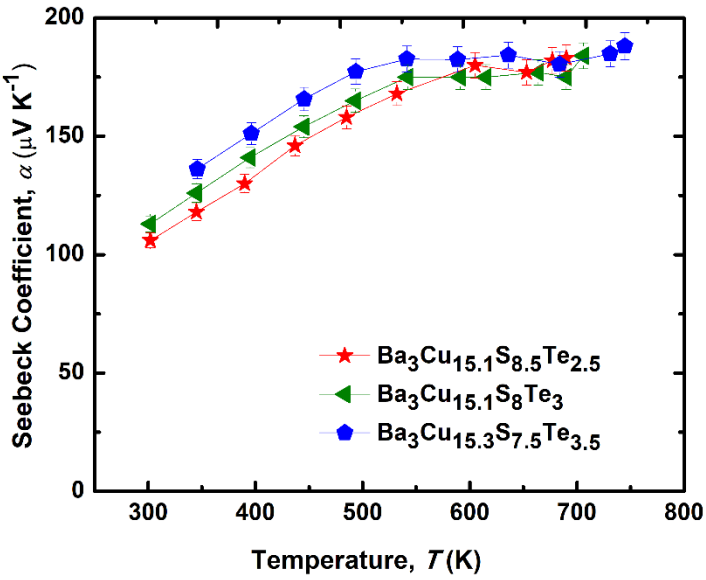


Figure 4.6 Temperature dependence of the Seebeck coefficient of $Ba_3Cu_{16-x}S_{11-y}Te_y$.

Typically, the sample with the higher electrical conductivity exhibits a lower Seebeck coefficient, so this situation is relatively rare but has been previously observed in cases with significant changes in the band structure. Examples include the occurrence of band degeneracies upon changing the Si/Sn ratio in *n*-doped $Mg_2(Si,Sn)$[159,160] and the co-existence of flat and steep bands when going from $Tl_2Ag_{12}Se_7$[151] to $Tl_2Ag_{12}Te_{7+x}$.[122]

The power factor, *PF*, of 4.6 $\mu$W cm$^{-1}$K$^{-2}$ for $Ba_3Cu_{15.3}S_{7.5}Te_{3.5}$ at 690 K is a product of the $\sigma$ value of 131 $\Omega^{-1}$cm$^{-1}$ and the square of the $\alpha$ value of 188 $\mu$V K$^{-1}$ at that temperature. As illustrated in Figure 4.7 (within ±7% estimated error), *PF* shows a general increase throughout the measured temperature range. The highest calculated *PF* of 2.4 $\mu$W cm$^{-1}$K$^{-2}$ at 700 K for the cold-pressed $Ba_3Cu_{16}S_9Te_2$[157] is almost 50% lower than the *PF* of the hot-pressed $Ba_3Cu_{15.3}S_{7.5}Te_{3.5}$. This confirms the expected high impact of hot-pressing on the transport properties.

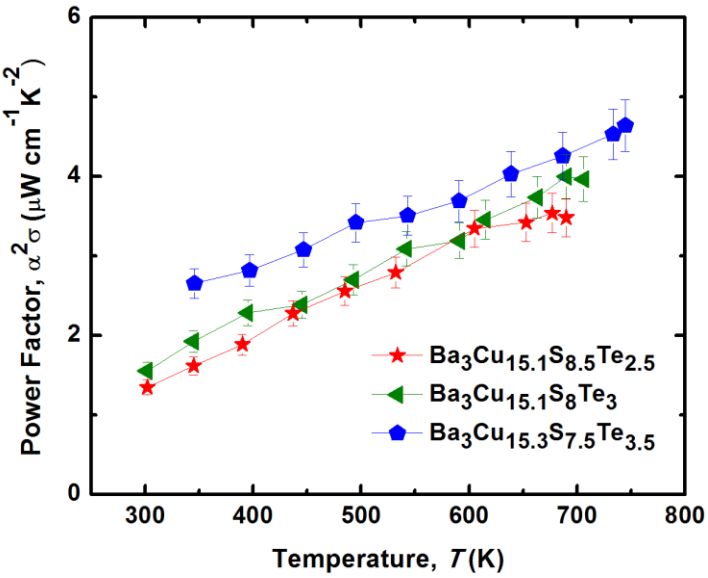


Figure 4.7 Temperature dependence of the power factor of $Ba_3Cu_{16-x}S_{11-y}Te_y$.

In contrast to the selenides, the measured electrical transport properties upon three heating measurements with the $T_{max}$ = 690 K and the applied current density of 0.084 A cm$^{-2}$ appeared to be reproducible (Figure 4.8). The reproducibility of these data as compared to the non-reproducible data of the discussed selenides in chapter 3 reveals a higher stability of sulfides under the same measured conditions as the selenides.

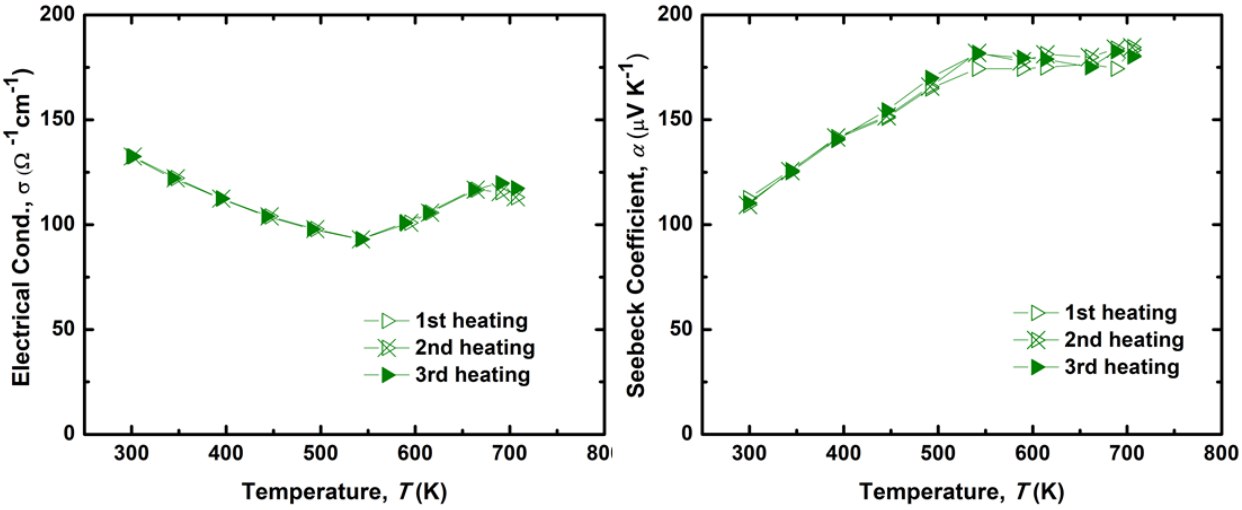


Figure 4.8 Stability of the electrical transport properties of $Ba_3Cu_{15.1}S_8Te_3$.

The powder XRD pattern after three consecutive electrical transport property measurements is depicted in Figure 4.9 in comparison to the calculated powder pattern (ICSD #261933). The purity of the sample after the stability measurements was demonstrated as no peaks related to side products could be detected.

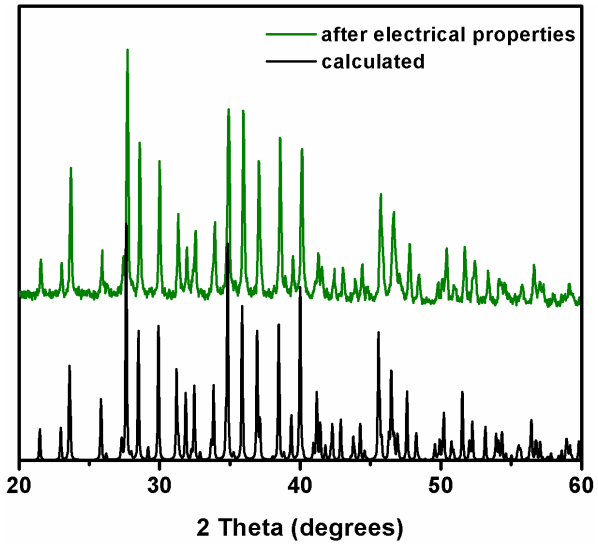


Figure 4.9 Powder XRD pattern of $Ba_3Cu_{15.1}S_8Te_3$ after three consecutive electrical transport property measurements.

The reproducibility of the electrical property measurements was furthermore demonstrated by measuring a bar prepared from the different hot-pressed sample of $Ba_3Cu_{15.3}S_{7.5}Te_{3.5}$ at DLR. The comparable results (Figure 4.10) were confirmed the reliability and reproducibility of the collected data at UW.

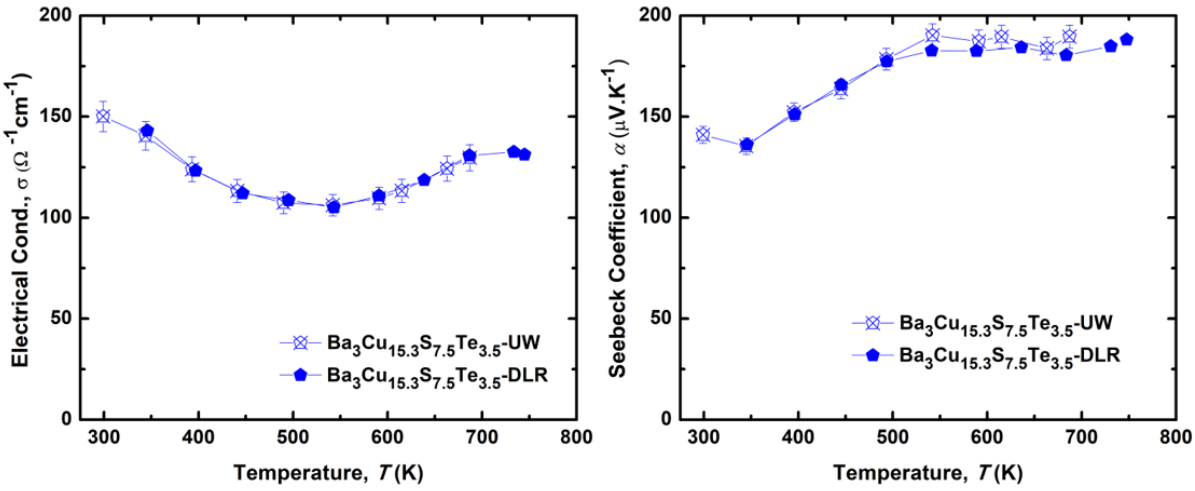


Figure 4.10 Reproducibility of the electrical transport properties of two different samples of $Ba_3Cu_{15.3}S_{7.5}Te_{3.5}$. UW: measured at the University of Waterloo; DLR: measured at the German Aerospace Center.

Very low total thermal conductivity values below 0.6 W $m^{-1}K^{-1}$ were observed for all discussed materials in the measured temperature range (Figure 4.11). The thermal conductivity values are all smaller than those for the selenides. In comparison with the reported thermal conductivity for the binary materials, $Cu_{1.97}S$ (0.6 W $m^{-1}K^{-1}$ at 307 K and 0.5 W $m^{-1}K^{-1}$ at 800 K)[68] and $\beta$-$Cu_2Se$ (1.0 W $m^{-1}K^{-1}$ at 420 K and 0.9 W $m^{-1}K^{-1}$ at 750 K),[27] which owe the low thermal conductivity to the phonon scattering caused by the Cu ion disorder, the surprisingly low $\kappa$ of the reported quaternary sulfide-tellurides is quite impressive.

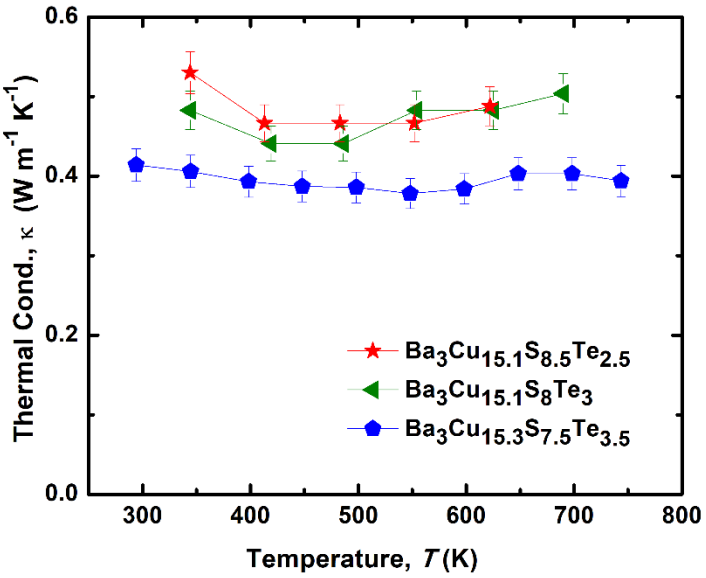


Figure 4.11 Temperature dependence of the thermal conductivity of $Ba_3Cu_{16-x}S_{11-y}Te_y$.

Thereafter, the lattice thermal conductivity, $\kappa_L$, was calculated. Figure 4.12 depicts the temperature dependent $\kappa_L$ for these quaternary barium copper chalcogenides. The ultralow lattice thermal conductivity, consistently below 0.5 W $m^{-1}K^{-1}$, for these materials is indicative of a short phonon mean free path.

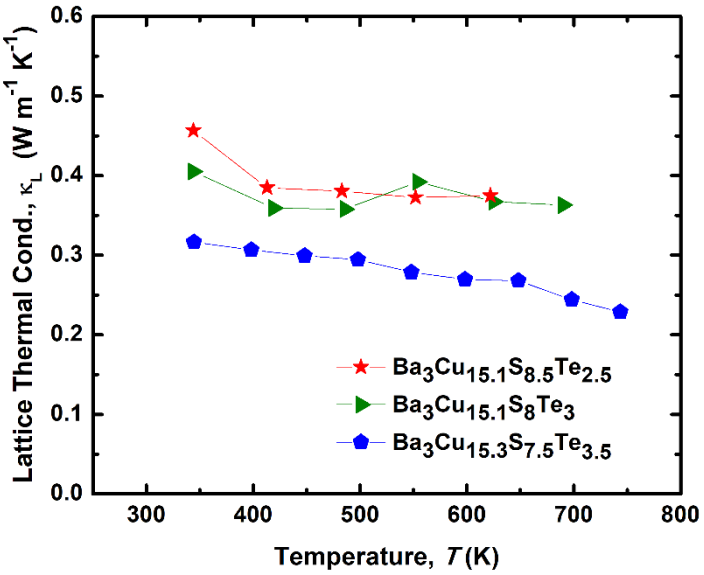


Figure 4.12 Temperature dependence of the lattice thermal conductivity of $Ba_3Cu_{16-x}S_{11-y}Te_y$.

As discussed in details in the introductory chapter of this thesis, a low lattice thermal conductivity may occur in different materials for various reasons. Here, the coherent Cu atom network along with the many deficient Cu sites may enable Cu ion mobility through the whole material. Although the diffusion of Cu ions is not comparable to that of the fast ion conductors such as $Ag_2Te$ and $Zn_4Sb_3$[39,154,155] (which in turn allows for the observed stability of this material) or even the selenide variants, it may still impact $\kappa_L$ to some extent by temporarily filling additional sites and increasing the disorder. Additional reasons contributing to the low lattice thermal conductivity are the highly complex crystal structure, combined with Cu site deficiencies and S/Te mixed occupancies. For instance, $Ba_3Cu_{15.3}S_{7.5}Te_{3.5}$ with $\kappa_L$ of 0.39 W m$^{-1}$K$^{-1}$ at around 420 K and 0.23 W m$^{-1}$K$^{-1}$ 745 K possesses a lower $\kappa_L$ than the binary $\beta$-$Cu_2Se$ with its relatively simple cubic structure, which exhibits $\kappa_L$ = 0.59 W m$^{-1}$K$^{-1}$ at those temperatures.[27]

Finally, *zT* values (Figure 4.13) were determined from the thermal conductivity and the polynomial fits of the power factor data for the whole temperature range. Throughout the measured temperature range, *zT* exhibits an overall increase, similar to *PF*, with increasing temperature for each sample. $Ba_3Cu_{15.3}S_{7.5}Te_{3.5}$, as the material with the highest *PF* and the lowest $\kappa$ here, achieves consequently the highest *zT* values, with a maximum of 0.88 at 745 K. The *zT* values of the other two materials investigated here are equivalent to each other within the estimated error of 10%.

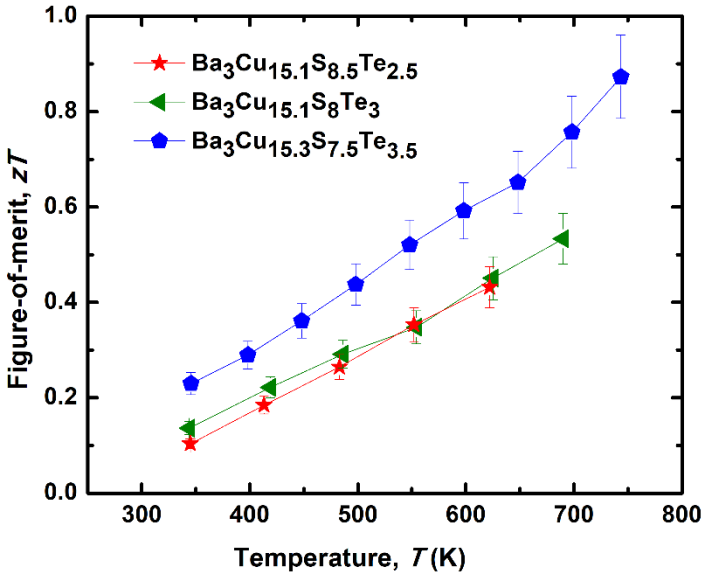


Figure 4.13 Thermoelectric figure-of-merit of $Ba_3Cu_{16-x}S_{11-y}Te_y$.

The thermoelectric figure-of-merit is comparable with the *zT* values of $Cu_2S$ and $\beta$-$Cu_2Se$. For example, $\beta$-$Cu_2Se$ shows a slightly lower *zT* value of 0.82 at 750 K,[27] while $Cu_{1.98}S$ has a higher *zT* value of 0.93 at 750 K. However, the quaternary sulfide-telluride materials

presented in this chapter appear to be more reliable for thermoelectric applications than these binary copper chalcogenides.

$Ba_3Cu_{15.3}S_{7.5}Te_{3.5}$ shows a $zT$ value of 0.59 at 600 K, which is comparable with the $zT$ of another barium copper sulfide-telluride, namely $BaCu_{5.9}STe_6$ with $zT$ = 0.53 at 581 K. While the corresponding selenide-telluride $BaCu_{5.9}SeTe_6$ with $zT$ = 0.81 at 600 K is a more efficient thermoelectric material at that temperature, it decomposes above 663 K.[109] Finally, with the $zT$ = 0.73 at 690 K, $Ba_3Cu_{15.3}S_{7.5}Te_{3.5}$ has a better performance than $Ba_3Cu_{16-x}Se_{11-y}Te_y$ at the same temperature. The thermoelectric properties of these $Ba_3Cu_{16-x}S_{11-y}Te_y$ samples are summarized in Table 4.3.

Table 4.3 Thermoelectric properties of $Ba_3Cu_{16-x}S_{11-y}Te_y$.

| Property | $Ba_3Cu_{15.1}S_8Te_3$ | $Ba_3Cu_{15.1}S_{8.5}Te_{2.5}$ | $Ba_3Cu_{15.3}S_{7.5}Te_{3.5}$ |
|---|---|---|---|
| $T$ (K) | 345 K/690 K | 345 K/690 K | 345 K/745 K |
| $\sigma$ ($\Omega^{-1}cm^{-1}$) | 123/119 | 116/104 | 143/131 |
| $\alpha$ ($\mu$V $K^{-1}$) | 126/175 | 118/183 | 136/188 |
| $PF$ ($\mu$W $cm^{-1}K^{-2}$) | 1.9/4.0 | 1.6/3.5 | 2.7/4.6 |
| $\kappa$ (W $m^{-1}K^{-1}$) | 0.48/0.50 | 0.53/0.49 (622 K)* | 0.41/0.39 |
| $\kappa_L$(W $m^{-1}K^{-1}$) | 0.41/0.36 | 0.46/0.37 (622 K)* | 0.32/0.23 |
| $zT$ | 0.14/0.53 | 0.11/0.43 (622 K)* | 0.23/0.88 |

*Maximum of the measured temperature is 622 K.

## 4.4 Conclusions

The thermoelectric properties of *p*-type $Ba_3Cu_{16-x}S_{11-y}Te_y$ (x = 0.7, 0.9 and y = 2, 2.5, 3.5) have been investigated. Heavy doping of $Ba_3Cu_{16-x}S_{11-y}Te_y$ *via* introducing Cu deficiencies resulted in a moderate electrical conductivity and Seebeck coefficient, which led to a power factor of 4.6 $\mu$W $cm^{-1}K^{-2}$ for the best measured sample, $Ba_3Cu_{15.3}S_{7.5}Te_{3.5}$. What causes the good thermoelectric performance of these materials in high temperatures, is not their moderate power factor but their outstanding low thermal conductivity. The latter is a consequence of their complex crystal structure, Cu atom deficiencies, and S/Te mixing. Ultimately, a maximum figure-of-merit value of $zT$ = 0.88 was found at 745 K for the compound with the largest Te content, namely $Ba_3Cu_{15.3}S_{7.5}Te_{3.5}$. With $Ba_3Cu_{15.3}S_{7.5}Te_{3.5}$ exhibiting $zT$ = 0.73 at 690 K for sulfides outperform the selenides discussed in chapter 3, whose highest $zT$ is 0.49 at 690 K.

In contrast to the selenides, which exhibit stability only in measurements up to 580 K, sulfides are stable in a significantly larger temperature range, up to the maximum measured temperature of 745 K. The higher stability of the sulfides appears to be a consequence of the lower Cu ion mobility compared to the selenides, which is likely related to the higher hardness and lower polarizability of the $S^{2-}$ atoms as compared to the $Se^{2-}$.

Below 750 K, $Ba_3Cu_{15.3}S_{7.5}Te_{3.5}$ has a $zT$ value comparable with promising thermoelectric materials such as $\beta$-$Cu_2Se$ and $Cu_{1.98}S$ at these temperatures. In contrast to these binary copper chalcogenides, the here reported materials are potentially more applicable for

thermoelectric devices because of their stability during the measurements performed so far. However, in order to utilize these materials in device fabrication, more investigations about the ionic diffusivity through other stability measurements such as applying larger currents at different temperatures with different measurement times should be performed.

# 5. Effect of Mixed Occupancies on the Thermoelectric Properties of $BaCu_{6-x}Se_{1-y}Te_{6+y}$ Polychalcogenides

## 5.1 Introduction

Electronic structure calculations revealed a narrow band gap of 0.05 eV for the charge balanced quaternary copper chalcogenide, $BaCu_6SeTe_6$.[98] Previously, "$BaCu_{5.9}SeTe_6$" with statistically 74% occupied Cu sites was reported to attain a $zT$ of 0.81 at 600 K.[109] The combination of a moderate electrical conductivity, $\sigma$ = 131 $\Omega^{-1}cm^{-1}$, and a moderate Seebeck coefficient, $\alpha$ = 213 $\mu$V $K^{-1}$, with the thermal conductivity being consistently below 0.6 W $m^{-1}K^{-1}$ allowed this $zT$ value to be achieved. Hence, "$BaCu_{5.9}SeTe_6$" is a better thermoelectric material than $\beta$-$Cu_2Se$ with $zT$ = 0.57 at around 600 K.[27] A higher power factor due to the larger electrical conductivity values of the Se variant leads to the larger $zT$ value of "$BaCu_{5.9}SeTe_6$" compared to "$BaCu_{5.9}STe_6$", while "$BaCu_{5.9}STe_6$" exhibits the lower $\kappa$ in the studied temperature range. Therefore, decreasing the thermal conductivity of $BaCu_{5.9}SeTe_6$ to the benefit of increasing the $zT$ value was considered. Here, we studied the effect of the mass fluctuation by varying the amount of the chalcogen atoms Se and Te on one crystallographic site on the thermoelectric properties of $BaCu_{6-x}Se_{1-y}Te_{6+y}$. Increasing the Te content should also occur with more covalent interactions, as Te is more metallic and electropositive than Se. The influence of mixing Se and Te atoms in different ratios in this material is discussed in this chapter, and was published in 2019.[161]

## 5.2 Experimental Procedure

All compounds were synthesized from the following elements (Ba pieces, 99.7%, Strem Chemicals; Cu powder, 99.5%, Alfa Aesar; Se pellets, 99.9%, Alfa Aesar; Te broken ingots, 99.99%, Strem Chemicals). All elements were transferred into C-coated silica tubes, evacuated and sealed. The reactions took place in programmable furnaces through a melting and slow cooling process. Evacuated tubes were heated up to 1023 K in 12 hours, then the furnace was cooled down to 663 K in 20 hours and lastly cooled down to room temperature. In order to obtain pure products, all samples were ground and re-annealed at 663 K. The length of the annealing time was directly related to the amount of Te atom in the sample; starting from 300 hours for the sample with the smallest amount of Te as a minimum annealing time, and ending in three weeks for the samples with the maximum amount of added Te, $y = 0.4$.

Thereafter, the synthesized compounds were ground into powder and their phase purity was checked *via* powder X-ray diffraction. Figure 5.1 demonstrates the purity of the samples with ($x = 0.1, 0.26$ and $y = 0, 0.1, 0.3, 0.4, 0.54$).

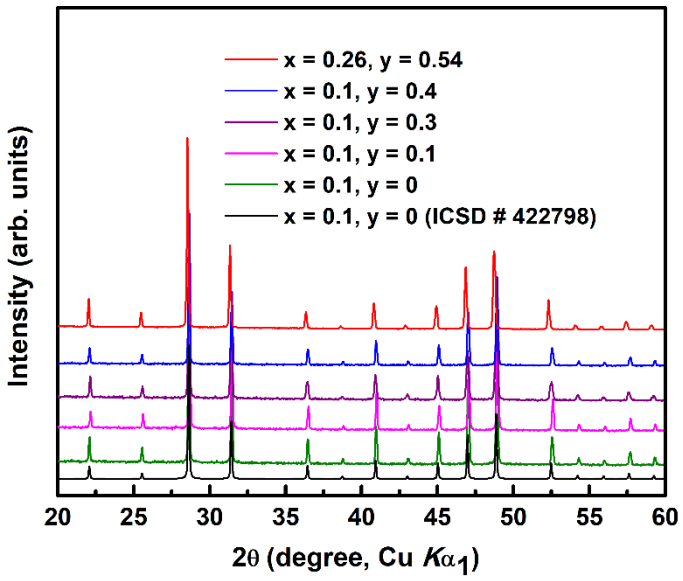


Figure 5.1 Room temperature powder XRD patterns of $BaCu_{6-x}Se_{1-y}Te_{6+y}$.

Excluding "$BaCu_{5.9}SeTe_6$", all samples were hot-pressed under a pressure of 47 MPa at temperature of 593 K for a duration of one hour. "$BaCu_{5.9}SeTe_6$" with its lower Te content was hot-pressed at the higher temperature of 623 K, under the same pressure as the other samples for one hour. Using the lower temperature to hot-press "$BaCu_{5.9}SeTe_6$" yielded lower relative density, and thus worse transport properties. These procedures resulted in relative densities of 98% – 99% of the theoretical values determined from X-ray data. Room temperature powder XRD patterns of the hot-pressed samples were depicted in Figure 5.2.

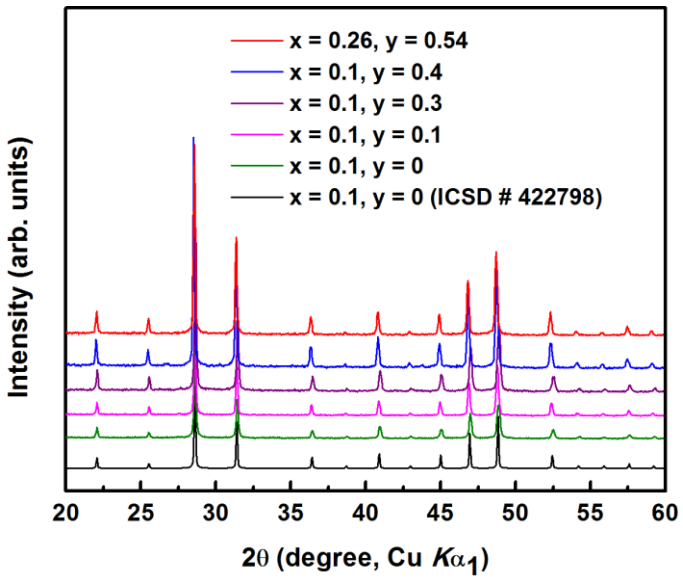


Figure 5.2 Room temperature powder XRD patterns of $BaCu_{6-x}Se_{1-y}Te_{6+y}$ after hot-pressing.

## 5.3 Results and Discussion

### 5.3.1 Crystal Structure and Crystallographic Data

By using two different chalcogen atoms such as Se and Te, $BaCu_{6-x}Se_{1-y}Te_{6+y}$ crystallizing in the cubic space group $Pm\bar{3}$ was uncovered.[98] In this structure, Ba and Cu atoms occupy the Wyckoff positions of 1*b* and 8*i* respectively. Te atoms fully occupy the 6*f* (Te1) and share the 1*a* Wyckoff position with the Se atom (*Q*2 = Se2/Te2) when y > 0.

The structure is composed of $Cu_{8-x}$ cubes centered by $Q2^{2-}$ atoms, interconnected *via* bonds to $Te_2^{2-}$ pairs and the Ba cations to a three-dimensional network (Figure 5.3). Such $Te_2^{2-}$ dumbbells also occur in $K_2BaCu_8Te_{10}$ and $Cs_2BaCu_8Te_{10}$.[162]

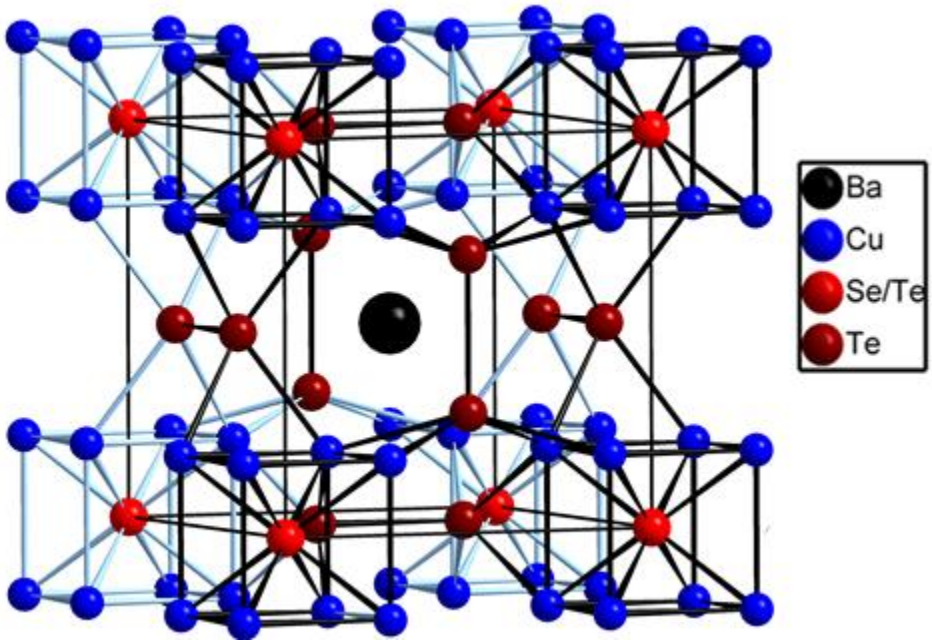


Figure 5.3 Crystal structure of $BaCu_{6-x}Se_{1-y}Te_{6+y}$.

For an electron precise formula, the Cu content is six per formula unit, as expressed in $Ba^{2+}(Cu^{+})_6Se^{2-}(Te_2^{2-})_3$, corresponding to a 75% occupancy of the Cu site. Noting that Cu chalcogenides, including $Cu_{2-x}Se$ and $Cu_{2-x}Te$,[163,164] are rather Cu-deficient than Cu-rich, at least two of the eight corners of the $Cu_{8-x}Q2$ cubes will be unoccupied corresponding to $BaCu_{6-x}SeTe_6$ with $x \geq 0$.

Along the edges of the cubes, $d^{10}$–$d^{10}$ Cu–Cu bonds occur with lengths of 2.78 Å in case of $BaCu_{5.9}SeTe_6$, and 2.80 Å in case of $BaCu_{5.74(2)}Se_{0.43(2)}Te_{6.57}$. The existence of the nonclassical $d^{10}$–$d^{10}$ bonds between Cu atoms along with the Cu site deficiencies, may cause a local ionic mobility inside the $Cu_{8-x}Q2$ cages. The enlarged anisotropic displacement parameters of the Cu atom, being up to 50% higher than that of the Ba and Te atoms, may be indicative of this. In any case, the Cu ions cannot readily move from cage to cage as the path is blocked by the larger atoms, Ba and Te.

Three samples with different nominal compositions of "$BaCu_{5.4}Se_{0.6}Te_{6.4}$", "$BaCu_{5.74}Se_{0.6}Te_{6.4}$" and "$BaCu_{5.9}Se_{0.6}Te_{6.4}$" were analyzed *via* single crystal structure studies. Here, the refinement procedure is described for "$BaCu_{5.9}Se_{0.6}Te_{6.4}$", and the rest of the refinements followed the same procedure. The refinement of the fully occupied sites, which were previously published,[98] resulted in $R(F_o)$ = 0.065 with a high equivalent isotropic displacement parameter $U_{eq}$ = 0.046 Å$^2$ for the Cu atom. To reduce the highest peak of 6.9 e Å$^{-3}$ in vicinity of the Se atom on 1*a*, the 1*a* site was refined as a mixed Se/Te occupied site (Se2/Te2). The least square refinements of this model led to the $R(F_o)$ = 0.059 for all reflections. The large value of the deepest hole in vicinity of the Cu atom, 4.0 e Å$^{-3}$, was lowered to 0.7 e Å$^{-3}$ after refining the Cu atom occupancy. As a consequence, $R(F_o)$ was lowered further to 0.010, and the thermal expansion parameter $U_{eq}$ was decreased to 0.029 Å$^2$, as the occupancy of the Cu site was refined to 72%. This occupancy corresponds to 5.74(2) Cu atoms per formula unit.

Including the other two cases, the refined Cu content varied only insignificantly from 5.74(2) to 5.79(2), while the nominal Cu content changed from 5.4 to 5.9. On the other hand, crystals obtained from samples of the nominal compositions of "$BaCu_{5.4}SeTe_6$" and "$BaCu_{5.9}SeTe_6$" showed refined Cu contents around 5.9, as expressed in the formulae $BaCu_{5.89(3)}SeTe_6$ and $BaCu_{5.93(2)}SeTe_6$.[98] Therefore, it is concluded that mixing Se and Te atoms on the 1*a* site results in lower Cu contents in the target materials, compared to $BaCu_{6-x}SeTe_6$, independent of the exact starting Cu amount.

The crystallographic details of the samples with mixed Se/Te occupancies, "$BaCu_{5.4}Se_{0.6}Te_{6.4}$", "$BaCu_{5.74}Se_{0.6}Te_{6.4}$" after the physical property measurements, and "$BaCu_{5.9}Se_{0.6}Te_{6.4}$" are summarized in Table 5.1. Tables 5.2 - 5.4 contain the fractional atomic coordinates, equivalent isotropic displacement parameters and occupancies of $BaCu_{5.74(2)}Se_{0.69(1)}Te_{6.31}$, $BaCu_{5.79(2)}Se_{0.61(2)}Te_{6.39}$ and $BaCu_{5.74(2)}Se_{0.43(2)}Te_{6.57}$.

Table 5.1 Crystallographic details of $BaCu_{6-x}Se_{0.6}Te_{6.4}$.

| Refined formula | $BaCu_{5.74(2)}Se_{0.69(1)}Te_{6.31}$ | $BaCu_{5.79(2)}Se_{0.61(2)}Te_{6.39}$ | $BaCu_{5.74(2)}Se_{0.43(2)}Te_{6.57}$ |
|---|---|---|---|
| Formula weight | 1361.90 | 1369.05 | 1373.71 |
| $T$ [K] | 296(2) | 296(2) | 296(2) |
| λ [Å] | 0.71073 | 0.71073 | 0.71073 |
| Crystal System | Cubic | Cubic | Cubic |
| space group | $Pm\bar{3}$ (no. 200) | $Pm\bar{3}$ (no. 200) | $Pm\bar{3}$ (no. 200) |
| $a$ [Å] | 6.9819(6) | 6.9858(5) | 6.9966(9) |
| $V$ [Å$^3$] | 340.35(9) | 340.92(7) | 342.5(1) |
| $Z$ | 1 | 1 | 1 |
| $R(Fo)$,[a] $R_w(Fo^2)$,[b] GOF (obs. data) | 0.015, 0.025, 1.09 | 0.026, 0.036, 1.15 | 0.010, 0.024, 1.07 |
| Min., max. residual electron density [e Å$^{-3}$] | −0.49, 0.58 | −1.12, 1.04 | −0.70, 0.41 |

[a] $R(F_o) = \Sigma||F_o|-|F_c|| / \Sigma|F_o|$; [b] $R_w(F_o^2) = [\ \Sigma[w(F_o^2 - F_c^2)^2] / \Sigma[w(F_o^2)^2]\ ]^{1/2}$, with $F_o$ and $F_c$ being the observed and calculated structure factors, respectively.

Table 5.2 Fractional atomic coordinates, equivalent isotropic displacement parameters and occupancies of $BaCu_{5.74(2)}Se_{0.69(1)}Te_{6.31}$.

| | Site | x | y | z | $U_{eq}/Å^2$ | occ. |
|---|---|---|---|---|---|---|
| Ba1 | 1*b* | ½ | ½ | ½ | 0.0209(2) | 1 |
| Cu1 | 8*i* | 0.19980(7) | *x* | *x* | 0.0254(3) | 0.718(2) |
| Te1 | 6*f* | 0.30021(5) | 0 | ½ | 0.0172(1) | 1 |
| *Q*2 (Se2, Te2) | 1*a* | 0 | 0 | 0 | 0.0428(6) | 0.69(1), 0.31 |

Table 5.3 Fractional atomic coordinates, equivalent isotropic displacement parameters and occupancies of $BaCu_{5.79(2)}Se_{0.61(2)}Te_{6.39}$.

| | Site | x | y | z | $U_{eq}/Å^2$ | occ. |
|---|---|---|---|---|---|---|
| Ba1 | 1*b* | ½ | ½ | ½ | 0.0216(4) | 1 |
| Cu1 | 8*i* | 0.2001(1) | *x* | *x* | 0.0274(6) | 0.724(3) |
| Te1 | 6*f* | 0.30031(8) | 0 | ½ | 0.0183(3) | 1 |
| *Q*2 (Se2, Te2) | 1*a* | 0 | 0 | 0 | 0.046(1) | 0.61(2), 0.39 |

Table 5.4 Fractional atomic coordinates, equivalent isotropic displacement parameters and occupancies of $BaCu_{5.74(2)}Se_{0.43(2)}Te_{6.57}$.

| | Site | x | y | z | $U_{eq}/Å^2$ | occ. |
|---|---|---|---|---|---|---|
| Ba1 | 1*b* | ½ | ½ | ½ | 0.0211(2) | 1 |
| Cu1 | 8*i* | 0.20018(6) | *x* | *x* | 0.0269(2) | 0.717(2) |
| Te1 | 6*f* | 0.30031(8) | 0 | ½ | 0.0175(1) | 1 |
| *Q*2 (Se2, Te2) | 1*a* | 0 | 0 | 0 | 0.0578(5) | 0.43(2), 0.57 |

According to the crystallographic information, increasing the amount of Te atoms leads to lower Cu occupancies. This is most likely a consequence of the larger size of the Te compared to the Se atom. For example, the Slater radii are 1.40 Å and 1.15 Å, respectively. Correspondingly, the Cu–*Q*2 distances are 2.52 Å in $Cu_2Se$[165] and 2.61 Å in high temperature $Cu_2Te$.[166] The Cu–Te1 distance in $BaCu_{5.9}SeTe_6$ is 2.61 Å, while the Cu–Se2 distance is as expected significantly shorter with 2.41 Å. In case of $BaCu_{5.74(2)}Se_{0.43(2)}Te_{6.57}$, the corresponding distances are 2.62 Å and 2.43 Å, respectively, while the *Q*2 site includes 40% Se and 60% Te. Therefore, these cubes are particularly strained when centered by the larger Te atom, causing a higher Cu atom deficiency. Experimentally we observed $0.20 \leq x \leq 0.26$ in $BaCu_{6-x}Se_{1-y}Te_{6+y}$ when $y > 0.3$, compared to $0.07 \leq x \leq 0.08$ when $y = 0$.

### 5.3.2 Thermoelectric Properties

Temperature dependent electrical conductivity data are plotted in Figure 5.4. The electrical conductivity, $\sigma$, decreases with increasing temperature for all measured samples with

various Te concentrations, which is typical for heavily doped semiconductors. Increasing the amount of Te atoms generally results in higher $\sigma$ in the measured temperature range, in accord with the demonstrated higher Cu atom deficiency. For instance, at room temperature, the $\sigma$ value of the material with the largest amount of Te atoms, "$BaCu_{5.74}Se_{0.46}Te_{6.54}$", is 685 $\Omega^{-1}cm^{-1}$, which is almost three times larger than the measured $\sigma$ value of 242 $\Omega^{-1}cm^{-1}$ for "$BaCu_{5.9}SeTe_6$".

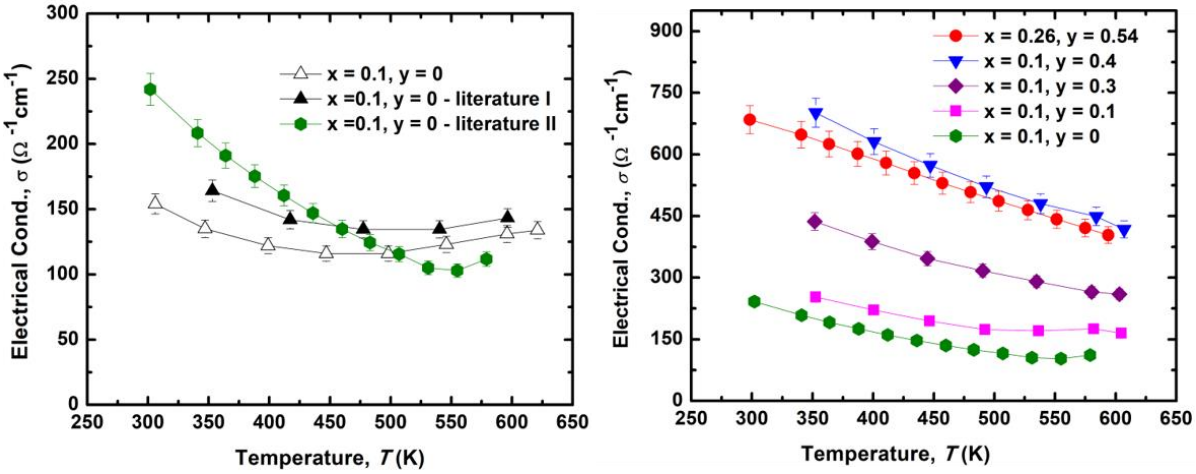


Figure 5.4 Temperature dependence of the electrical conductivity of $BaCu_{6-x}Se_{1-y}Te_{6+y}$. Literature data were "Adapted with permission from ref.[109] Copyright (2019) American Chemical Society."

In order to find the carrier concentration, Hall measurements were carried out on both "$BaCu_{5.74}Se_{0.46}Te_{6.54}$" and "$BaCu_{5.9}SeTe_6$" at room temperature. The positive $R_H$ indicates these materials to be semiconductors with holes as major charge carriers. The hole concentrations at room temperature, $n = 1/(R_H e)$ with the elementary charge as $e$, are $6.5 \times 10^{20}$

$cm^{-3}$ and $7.7 \times 10^{19}$ $cm^{-3}$ for "$BaCu_{5.74}Se_{0.46}Te_{6.54}$" and "$BaCu_{5.9}SeTe_6$", respectively. Thus, the experimental data support the statement that higher Te concentrations result in larger *p*-type defects in accord with the increased Cu atom deficiencies.

Charge carrier mobility of the samples "$BaCu_{5.74}Se_{0.46}Te_{6.54}$" and "$BaCu_{5.9}SeTe_6$" was determined to be 6.6 $cm^2V^{-1}s^{-1}$ and 19.6 $cm^2V^{-1}s^{-1}$, respectively. The lower mobility of the sample with the higher carrier concentration is likely a consequence of increased carrier scattering. With the mobility of the Te-rich sample being three times lower, and the carrier concentration over eight times higher, a significantly larger electrical conductivity results as mentioned above.

The temperature dependence of the Seebeck coefficient is plotted in Figure 5.5. The positive Seebeck coefficient values, increasing with increasing temperature, confirm the *p*-type character of these heavily doped semiconductors. Increasing the amount of Te atoms, thus the Cu atom deficiencies and thereby the (hole) charge carrier concentration, results in smaller Seebeck values, $\alpha$. For instance, at room temperature, the $\alpha$ values range from +49 $\mu$V $K^{-1}$ for "$BaCu_{5.74}Se_{0.46}Te_{6.54}$" to +164 $\mu$V $K^{-1}$ for "$BaCu_{5.9}SeTe_6$".

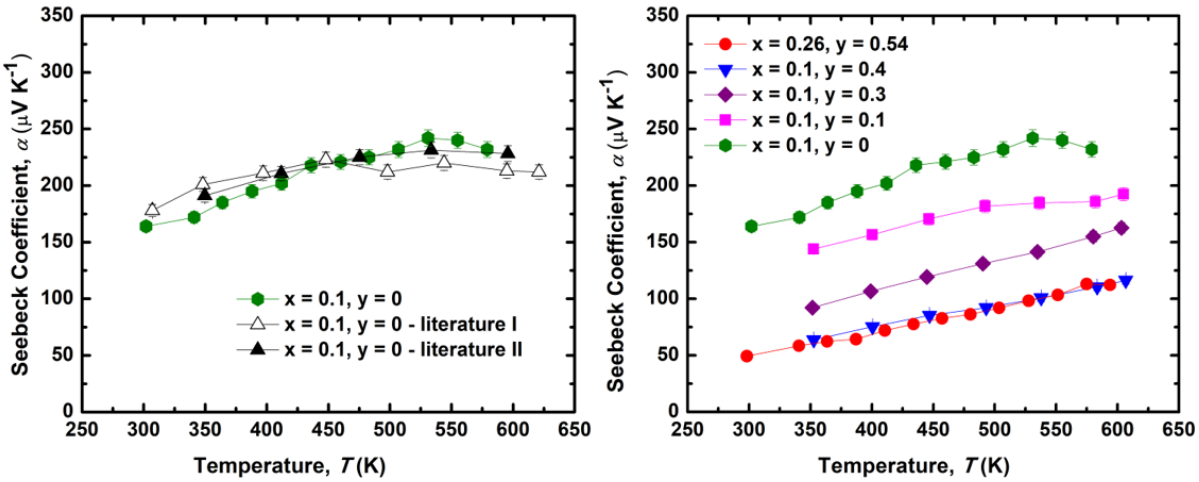


Figure 5.5 Temperature dependence of the Seebeck coefficient of $BaCu_{6-x}Se_{1-y}Te_{6+y}$. Literature data were "Adapted with permission from ref.[109] Copyright (2019) American Chemical Society."

The power factor curves for these barium copper polychalcogenides are plotted in Figure 5.6. The larger Seebeck coefficient throughout the measured temperature range for "$BaCu_{5.9}SeTe_6$" causes generally larger *PF* for this material compared to "$BaCu_{5.74}Se_{0.46}Te_{6.54}$" with the largest amount of Te atoms, (*e.g.* 6.5 $\mu$W cm$^{-1}$K$^{-2}$ compared to 1.7 $\mu$W cm$^{-1}$K$^{-2}$ at room temperature).

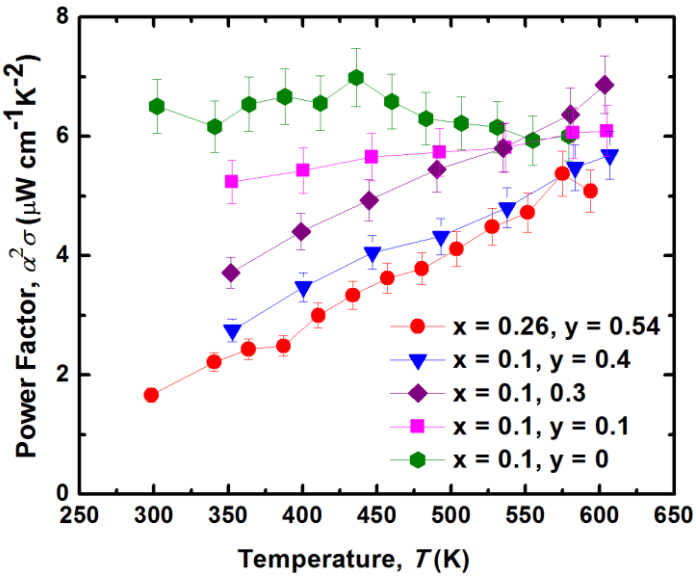


Figure 5.6 Temperature dependence of the power factor of $BaCu_{6-x}Se_{1-y}Te_{6+y}$.

As discussed in chapter 1, in order to suppress long range ion diffusion in $Cu_2Se$, some modifications were considered.[81,82,85,167] Moreover, it was previously concluded that "$BaCu_{5.9}SeTe_6$" is not suffering from a lack of stability arising from Cu ion migration, even though it likely has local Cu ion migration inside the $Cu_{8-x}Q2$ cages.[109] Here, we also demonstrated the stability of "$BaCu_{5.74}Se_{0.6}Te_{6.4}$" with higher Cu deficiencies than "$BaCu_{5.9}SeTe_6$". As revealed in Figure 5.7, the material's properties remained unchanged during five consecutive electrical property measurements.

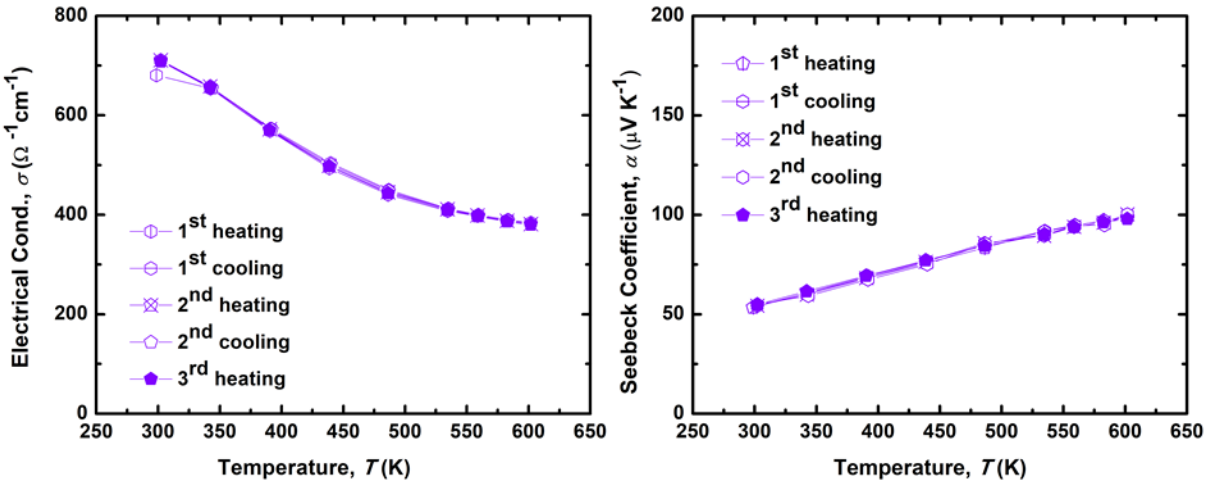


Figure 5.7 Stability of the electrical transport properties of "$BaCu_{5.74}Se_{0.6}Te_{6.4}$".

The stability of the "$BaCu_{5.74}Se_{0.46}Te_{6.54}$" after two times measurements of the transport properties was also illustrated in Figure 5.8.

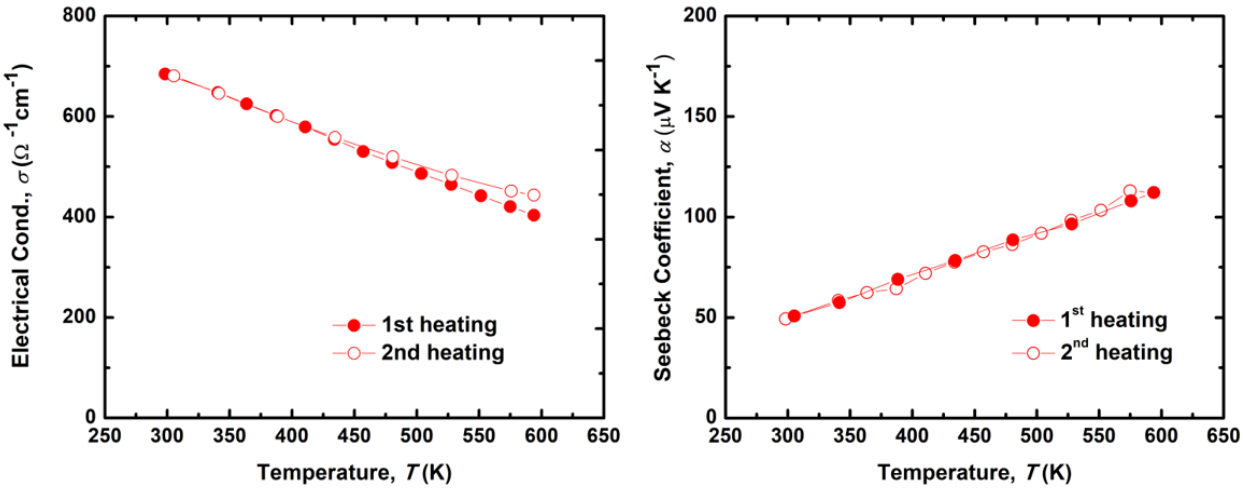


Figure 5.8 Stability of the electrical transport properties of "$BaCu_{5.74}Se_{0.46}Te_{6.54}$".

The concentration of the elements in "$BaCu_{5.74}Se_{0.46}Te_{6.54}$" after the physical property measurements was determined, *via* SEM/EDX with an applied acceleration voltage of 25 kV. The good agreement between the measured elemental atomic percentages of 7.8(2) : 41(1) : 4.7(5) : 47(3) and the nominal values of 7.3 : 41.7 : 3.3 : 47.6 indicates a reasonably homogeneous distribution of the elements in the sample with no decay after hot-pressing and subsequent property measurements. The larger deviation of the atomic-% of Se from the theoretical value may be explained as a result of a systematic difficulty in the elemental analysis of elements with low at-% *via* SEM/EDX.

All the measured materials exhibit low total thermal conductivity, $\kappa$, generally below 1 W $m^{-1}K^{-1}$ throughout the measured temperature range (Figure 5.9). Materials with larger $\sigma$ have overall higher thermal conductivity if the lattice contribution is comparable as in this case. Therefore, the samples with higher Te content have larger $\kappa$ values.

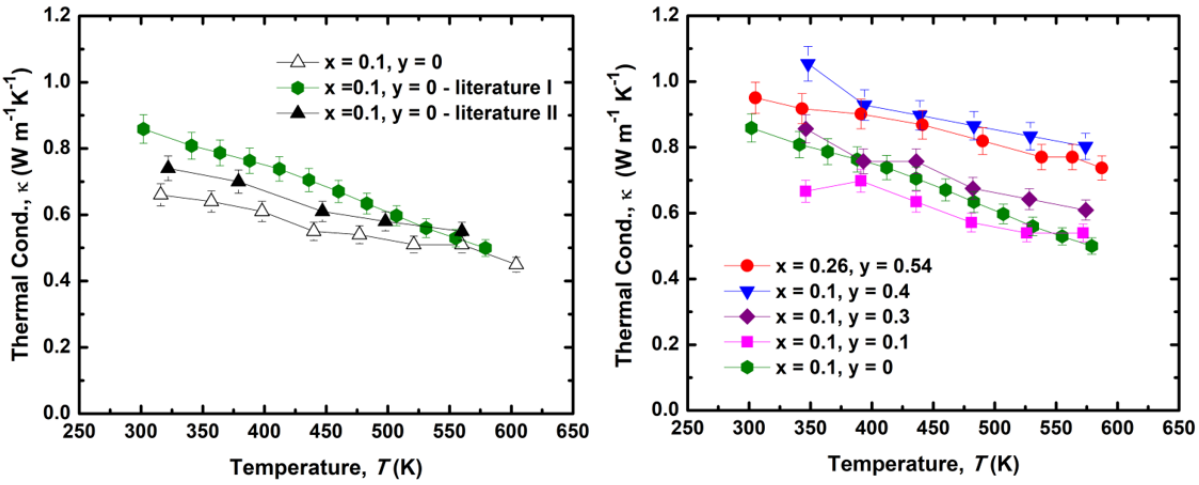


Figure 5.9 Temperature dependence of the thermal conductivity of $BaCu_{6-x}Se_{1-y}Te_{6+y}$. Literature data were "Adapted with permission from ref.[109] Copyright (2019) American Chemical Society."

As mentioned in previous chapters, a low thermal conductivity may occur for various reasons. For instance, in $\beta$-$Cu_2Se$, a disordered Cu atom sublattice results in a low lattice thermal conductivity and consequently a low thermal conductivity.[78] Here, a low $\kappa_L$ in combination with the moderate electrical conductivity, lead to the low total thermal conductivity.

All materials show very low $\kappa_L$ values, steadily below 0.8 W $m^{-1}K^{-1}$ (Figure 5.10). As expected, the sample with the highest Se/Te disorder, "$BaCu_{5.74}Se_{0.46}Te_{6.54}$", exhibits the smallest $\kappa_L$ here, while having similar values as "$BaCu_{5.9}Se_{0.6}Te_{6.4}$" within the estimated experimental error. The $\kappa_L$ values of the other materials with y = 0.1 and 0.3 do not follow a clear trend. The lattice thermal conductivity gradually decreases in all cases with the overall

smaller values for "$BaCu_{5.74}Se_{0.46}Te_{6.54}$" (0.51 W $m^{-1}K^{-1}$ at 305 K and 0.28 W $m^{-1}K^{-1}$ at 587 K). Reaching $\kappa_L$ = 0.28 W $m^{-1}K^{-1}$ at 587 K renders this material comparable or even better with respect to blocking the phonon propagation than most of the other copper chalcogenides with low $\kappa_L$: the lattice thermal conductivity of "$BaCu_{5.74}Se_{0.46}Te_{6.54}$" is lower than the $\kappa_L$ of $\beta$-$Cu_2Se$ ($\kappa_L$ = 0.59 W $m^{-1}K^{-1}$ at 352 K and 600 K) and $\beta$-$Cu_{1.98}Se$ ($\kappa_L$ = 0.59 W $m^{-1}K^{-1}$ at 352 K and 0.50 W $m^{-1}K^{-1}$ at 600 K).

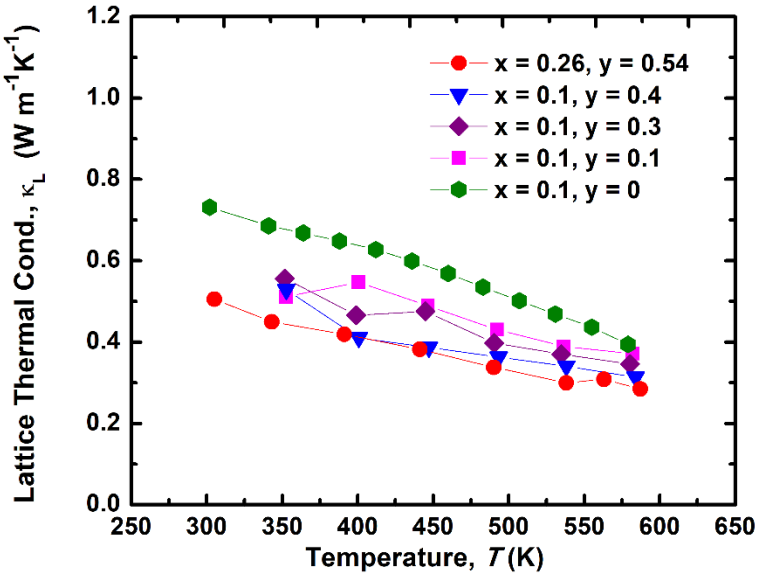


Figure 5.10 Temperature dependence of the lattice thermal conductivity of $BaCu_{6-x}Se_{1-y}Te_{6+y}$.

The figure-of-merit was plotted in Figure 5.11. This figure also reveals the reproducibility of figure-of-merit $zT$ of "$BaCu_{5.9}SeTe_6$" compared to the reported literature data. An overall increase in $zT$ with increasing temperature is observed in all the investigated samples. Among the here investigated copper polychalcogenides, "$BaCu_{5.9}SeTe_6$" and

"$BaCu_{5.9}Se_{0.9}Te_{6.1}$" exhibit the highest performance, while increasing Te beyond 6.1 per formula unit (y > 0.1) has a detrimental effect on the performance. The highest value of $zT$ = 0.39 at 580 K for "$BaCu_{5.74}Se_{0.46}Te_{6.54}$" is significantly lower than the $zT$ = 0.69 for "$BaCu_{5.9}SeTe_6$" at this temperature.

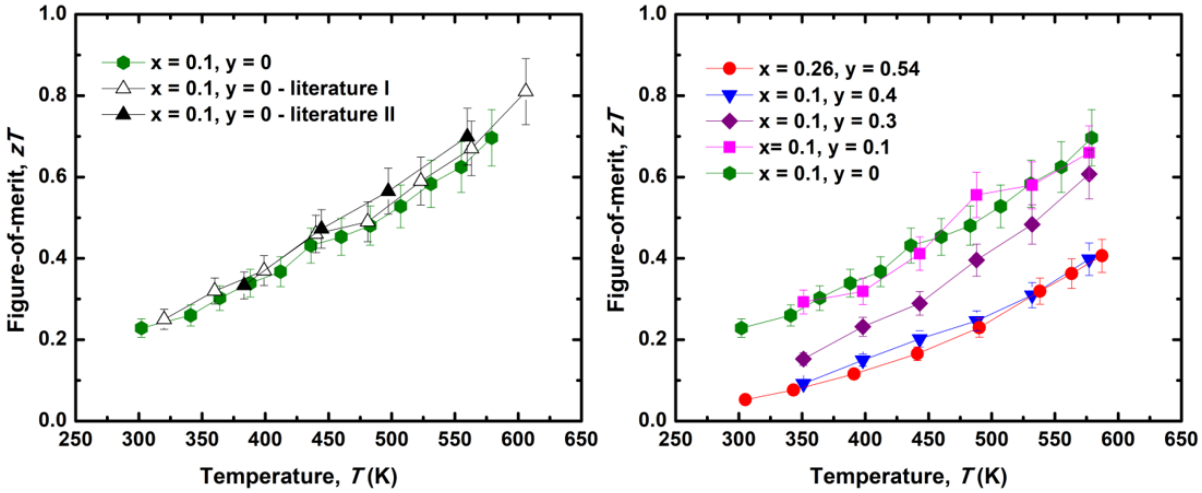


Figure 5.11 Reproducibility of the $zT$ values of "$BaCu_{5.9}SeTe_6$" (left). Thermoelectric figure-of-merit of $BaCu_{6-x}Se_{1-y}Te_{6+y}$ (right). Literature data were "Adapted with permission from ref.[109] Copyright (2019) American Chemical Society."

The thermoelectric properties of the samples with (x = 0.1, 0.26 and y = 0, 0.1, 0.3, 0.4, 0.54) measured at two different temperatures of ~ 350 K (first value) and ~ 575 K are summarized in Table 5.5.

Table 5.5 Thermoelectric properties of $BaCu_{6-x}Se_{1-y}Te_{6+y}$ at ~ 350 K (first value) and at ~ 575 K (second value).

| Property | x = 0.1, y = 0 | x = 0.1, y = 0.1 | x = 0.1, y = 0.3 | x = 0.1, y = 0.4 | x = 0.26, y = 0.54 |
|---|---|---|---|---|---|
| $\sigma$ ($\Omega^{-1}cm^{-1}$) | 202/110 | 253/176 | 437/267 | 702/454 | 640/421 |
| $\alpha$ ($\mu VK^{-1}$) | 176/234 | 144/185 | 92/153 | 64/109 | 58/113 |
| *PF* ($\mu W\ cm^{-1}K^{-2}$) | 6.3/6.0 | 5.2/6.0 | 3.7/6.3 | 2.8/5.3 | 2.1/5.4 |
| $\kappa$ ($W\ m^{-1}K^{-1}$) | 0.80/0.50 | 0.67/0.54 | 0.86/0.61 | 1.1/0.80 | 0.91/0.75 |
| $\kappa_L$($W\ m^{-1}K^{-1}$) | 0.68/0.40 | 0.51/0.37 | 0.56/0.35 | 0.53/0.31 | 0.44/0.29 |
| *zT* | 0.28/0.69 | 0.29/0.66 | 0.15/0.61 | 0.09/0.40 | 0.08/0.39 |

## 5.4 Conclusions

The effect of varying the Te content, y, on the thermoelectric properties of $BaCu_{6-x}Se_{1-y}Te_{6+y}$ was studied for the first time in comparison to $BaCu_{5.9}SeTe_6$. These polychalcogenides were synthesized with different Cu and chalcogen concentrations (x = 0.1, 0.26 and y = 0.1, 0.2, 0.3, 0.4, 0.54), then hot-pressed and the physical properties determined. The single crystal data analyses of selected samples with different nominal Cu contents of 5.4, 5.74 and 5.9, and y always being 0.4 revealed that the same nominal y results in similar Cu amounts in the target material, namely 5.74(2)–5.79(2) per formula unit, equal within two standard deviations. These Cu amounts were generally higher when y = 0, namely 5.89(3) - 5.93(2) per formula unit.

Larger mass fluctuations are often favorable for thermoelectric applications due to the shortening of the phonon propagation, causing a lower lattice thermal conductivity. Indeed, the

sample with the 46 : 54 Se/Te mixture on the *Q*2 site, "$BaCu_{5.74}Se_{0.46}Te_{6.54}$", has the smallest experimental lattice thermal conductivity among the measured samples in this article. However, as demonstrated by Hall measurements, the over eight times larger carrier concentration for "$BaCu_{5.74}Se_{0.46}Te_{6.54}$" in comparison to "$BaCu_{5.9}SeTe_6$" decreases the Seebeck values. In addition, the larger electrical conductivity of "$BaCu_{5.74}Se_{0.46}Te_{6.54}$" causes an undesired increase of the total thermal conductivity. Ultimately, the $zT$ = 0.39 for "$BaCu_{5.74}Se_{0.46}Te_{6.54}$" compared to $zT$ = 0.69 at 580 K for "$BaCu_{5.9}SeTe_6$" shows a better performance for the material with no mixed Se/Te occupancies. On a positive note, the properties of "$BaCu_{5.74}Se_{0.6}Te_{6.4}$" sample with its high Cu deficiency and Se/Te mixed occupancy remained unchanged during our repeat measurements, indicative of its high stability in contrast to e.g. $Cu_{2-x}Se$. It remains to be investigated, however, whether these materials would remain stable under the larger currents and temperature gradient applied in thermoelectric devices.

# 6. Summary and Outlook

In chapters 3 and 4 of this thesis, the thermoelectric properties of the quaternary barium copper sulfide/selenide-tellurides were studied. Samples with different concentrations of Cu and S/Se/Te were synthesized through melting and slow cooling process, hot-pressed and the physical properties were measured. Among the sulfide-tellurides, the sample with the largest amount of Te, exhibited the best thermoelectric performance with $zT$ = 0.88 at 745 K. On the other hand, the selenide-tellurides showed almost 50% smaller $zT$ values with 0.40 – 0.49 at 690 K – 697 K. A complex crystal structure and a mass fluctuation reduced the lattice thermal conductivity in both the sulfide- and the selenide-tellurides to below 0.6 W $m^{-1}K^{-1}$. For instance, $Ba_3Cu_{15.3}S_{7.5}Te_{3.5}$ with the lattice thermal conductivity of 0.23 W $m^{-1}K^{-1}$ at 745 K exhibited the lowest lattice thermal conductivity among both the measured sulfides and the selenides. This indeed is a result of a larger mass fluctuation of this material as compared to the rest of the measured samples, as it has the lowest S/Te ratio here. With such a low lattice thermal conductivity and moderate electrical transport properties for $Ba_3Cu_{15.3}S_{7.5}Te_{3.5}$, very small thermal conductivity of 0.39 W $m^{-1}K^{-1}$ at 745 K and a $zT$ = 0.88 at this temperature were attained. Further studies by increasing the Cu and Te concentrations to achieve materials with a better thermoelectric performance are suggested as a future work.

Surprisingly, repeating the physical property measurements revealed non-reproducible results for the selenide-tellurides, while the physical properties of the sulfide-tellurides were consistently stable under measurement conditions. The reliability of our data collected on the

sulfide samples was confirmed when the same results within the estimated experimental errors were obtained by our collaborator in German Aerospace Center (DLR).

Our crystallographic analyses revealed the existence of three extra Cu sites in the selenides as compared to the sulfide variants with a difference in the distribution of Cu atoms before and after the electrical transport property measurements. This proved the occurrence of the Cu ion movement either by the voltage or the temperature gradient during these measurements. The stability was investigated by applying different current densities and varying the maximum temperature. Decreasing the maximum measured temperature from 690 K to 580 K and the applied current density from 0.084 A $cm^{-2}$ to 0.005 A $cm^{-2}$ resulted in reproducibility of the data. Further investigations through SEM/EDX and the spatial resolution of the Seebeck coefficient (PSM) after the electrical transport property measurements confirmed the irreversible Cu ion movement due to the temperature gradient during the Seebeck measurement. In conclusion, with *zT* values smaller than those of the sulfides around 690 K and lack of stability around this temperature, the selenide variants are not applicable for thermoelectric materials' fabrication.

In chapter 5, the effect of the mixed chalcogen atom site occupancies on thermoelectric properties of $BaCu_{6-x}Se_{1-y}Te_{6+y}$ was studied. Phase pure samples with different Se/Te concentrations were obtained through melting and slow cooling process and further annealing. Increasing the Te atom concentration to 54% increased the electrical conductivity almost three times larger than in case of $BaCu_{5.9}SeTe_6$. As proven by Hall measurements, increasing the Te

content enhanced the number of the dominant carriers (holes) per formula unit by decreasing the Cu concentration, thereby increased the electrical conductivity and reduced the Seebeck coefficient. Increasing the concentration of the heavier Te atom also lowered the lattice thermal conductivity due to an enhanced overall mass as well as mass fluctuation. However, due to the detrimental effect of the smaller Seebeck values on the power factor, a smaller peak $zT$ as compared to $BaCu_{5.9}SeTe_6$ ($zT$ = 0.81 at 600 K) was attained with $zT$ = 0.41 at 587 K in case of $BaCu_{5.74}Se_{0.46}Te_{6.54}$.

The stability of these materials was demonstrated through repeating the electrical transport property measurements. Based on the lack of a suitable path of the Cu ions and the demonstrated stability of the electrical property measurements, these materials are more stable than the binaries, $Cu_2S$ and $\beta$-$Cu_2Se$. Other improvements to increase the $zT$ values may be tried in future including a particle size and nanostructuring study of the best sample. The thermal conductivity and the figure-of-merit of a few of the discussed materials in this thesis as compared to $\beta$-$Cu_2Se$ are depicted in Figure 6.1.

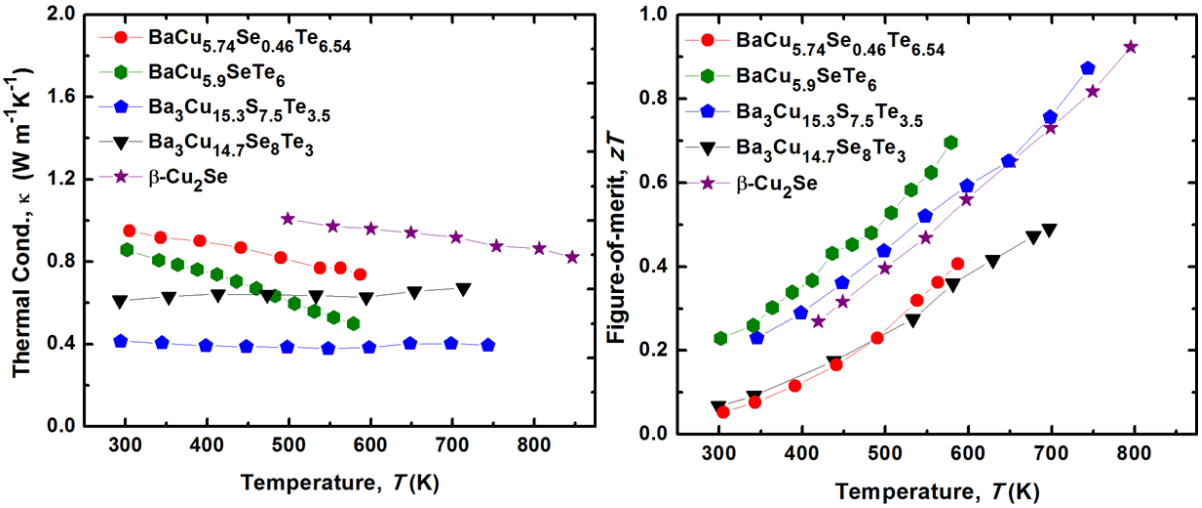


Figure 6.1 Thermal conductivity (left) and figure-of-merit (right) of the presented barium copper chalcogenides compared to the $\beta$-$Cu_2Se$. ($\beta$-$Cu_2Se$ data were reprinted with permission from ref.[27] Copyright 2019 Springer Nature).

# Bibliography

[1] J. He and T.M. Tritt, Science **357**, eaak9997 (2017).

[2] D.D. Pollock, in *CRC Handb. Thermoelectr.*, edited by D.M. Rowe (CRC Press, New York, 1995), pp. 7–17.

[3] J. Yang and F.R. Stabler, J. Electron. Mater. **38**, 1245 (2009).

[4] M. Matsumoto, M. Mori, T. Haraguchi, M. Ohtani, T. Kubo, K. Matsumoto, and H. Matsuda, SAE Int. J. Engines **8**, 1815 (2015).

[5] B. Orr, A. Akbarzadeh, M. Mochizuki, and R. Singh, Appl. Therm. Eng. **101**, 490 (2016).

[6] J. Yang and T. Caillat, MRS Bull. **31**, 224 (2006).

[7] http://www.dongfengtrucks.com/, (2015).

[8] https://www.gentherm.com/, (2019).

[9] https://www.sango.jp/en/, (2012).

[10] https://www.tenneco.com/, (2019).

[11] https://www.valeo.com/en/, (2018).

[12] R.R. Furlong and E.J. Wahlquist, Nucl. News **42**, 26 (1999).

[13] H.S. Choi, S. Yun, and K. Whang, Appl. Therm. Engin. **27**, 2841 (2007).

[14] https://www.europeanthermodynamics.com, (2015).

[15] https://www.marlow.com/, (2019).

[16] A.F. Ioffe, *Semiconductor Thermoelements, and Thermoelectric Cooling* (Infosearch, ltd., 1957).

[17] D. Zhao and G. Tan, Appl. Therm. Eng. **66**, 15 (2014).

[18] W. Jones and N.H. March, *Theoretical Solid State Physics* (Dover Publications, New York, 1985).

[19] G.J. Snyder and E.S. Toberer, Nat. Mater. **7**, 105 (2008).

[20] G.D. Mahan and J.O. Sofo, Proc. Natl. Acad. Sci. **93**, 7436 (1996).

[21] N.W. Ashcroft and N.D. Mermin, in *Solid State Phys.*, edited by D.G. Crane (Holt, Rinehart and Winston, Philadelphia, 1976), pp. 2–27.

[22] N.W. Ashcroft and N.D. Mermin, in *Solid State Phys.*, edited by D.G. Crane (Holt, Rinehart and Winston, Philadelphia, 1976), pp. 30–53.

[23] G.S. Kumar, G. Prasad, and R.O. Pohl, J. Mater. Sci. **28**, (1993).

[24] G.A. Slack, *Solid State Physics* (Academic Press, New York, 1979).

[25] E. Grüneisen, Ann. Phys. **344**, 257 (1912).

[26] G.A. Slack, in *CRC Handb. Thermoelectr.*, edited by D.M. Rowe (CRC Press, New York, 1995), pp. 407–440.

[27] H. Liu, X. Shi, F. Xu, L. Zhang, W. Zhang, L. Chen, Q. Li, C. Uher, T. Day, and G.J. Snyder, Nat. Mater. **11**, 422 (2012).

[28] A. Saramat, G. Svensson, A.E.C. Palmqvist, C. Stiewe, E. Müller, D. Platzek, S.G.K. Williams, D.M. Rowe, J.D. Bryan, and G.D. Stucky, J. Appl. Phys. **99**, 023708/1 (2006).

[29] B.C. Sales, D. Mandrus, and R.K. Williams, Science **272**, 1325 (1996).

[30] J. Corbett, J. Chem. Rev. **85**, 385 (1985).

[31] E.S. Toberer, A.F. May, and G.J. Snyder, Chem. Mater. **22**, 624 (2010).

[32] V. Keppens, D. Mandrus, C. Sales, B, B.C. Chakoumakos, P. Dai, R. Coldea, M.B. Maple, D.A. Gajewski, E.J. Freeman, and S. Bennington, Nature **395**, 876 (1998).

[33] B.B. Iversen, A.E.C. Palmqvist, D.E. Cox, G.S. Nolas, G.D. Stucky, N.P. Blake, and H.J. Metiu, J. Solid State Chem. **149**, 455 (2000).

[34] H. Kleinke, Chem. Mater. **22**, 604 (2010).

[35] H. Anno, M. Hokozano, M. Kawamura, J. Nagro, and K. Matsubara, in *Twenty First Int. Conf. Thermoelectr.* (2002), pp. 77–80.

[36] T. Takabatake, K. Suekuni, T. Nakayama, and E. Kaneshita, Rev. Mod. Phys. **86**, 669 (2014).

[37] M. Christensen, S. Johnsen, and B.B. Iversen, Dalt. Trans. **39**, 978 (2010).

[38] D.J. Braun and W. Jeitschko, J. Less-Common Met. **72**, 147 (1980).

[39] G.J. Snyder, M. Christensen, E. Nishibori, T. Caillat, and B.B. Iversen, Nat. Mater. **3**, 458 (2004).

[40] J. Xu and H. Kleinke, J. Comput. Chem. **29**, 2134 (2008).

[41] S.-G. Kim, I.I. Mazin, and D.J. Singh, J. Phys. Rev. B **57**, 6199 (1998).

[42] Y. Mozharivskyj, Y. Janssen, J.L. Harringa, A. Kracher, A.O. Tsokol, and G.J. Miller, Chem. Mater. **18**, 822 (2006).

[43] T. Caillat, J.P. Fleurial, and A. Borshchevsky, J. Phys. Chem. Solids **58**, 1119 (1997).

[44] M. Chitroub, F. Besse, and H. Scherrer, J. Alloy. Compd. **460**, 90 (2008).

[45] G. Cordier, H. Schäfer, and M.Z. Stelter, Anorg. Allg. Chem. **519**, 183 (1984).

[46] S.R. Brown, S.M. Kauzlarich, F. Gascoin, and G.J. Snyder, Chem. Mater. **18**, 1873 (2006).

[47] V. Fano, in *CRC Handb. Thermoelectr.*, edited by D.M. Rowe (CRC Press, New York, 1995), pp. 257–266.

[48] A.D. Lalonde, Y. Pei, and G.J. Snyder, Energy Environ. Sci. **4**, 2090 (2011).

[49] Y. Pei, A. Lalonde, S. Iwanaga, and G.J. Snyder, Energy Environ. Sci. **4**, 2085 (2011).

[50] H. Wang, Y. Pei, A.D. Lalonde, and G.J. Snyder, Adv. Mater. **23**, 1366 (2011).

[51] D.T. Morelli, V. Jovovic, and J.P. Heremans, Phys. Rev. Lett. **101**, 035901 (2008).

[52] L.D. Zhao, C. Chang, G. Tan, and M.G. Kanatzidis, Energy Environ. Sci. **9**, 3044 (2016).

[53] L.. Zhao, S.H. Lo, Y.S. Zhang, H. Sun, G.J. Tan, C. Uher, C. Wolverton, V.P. Dravid, and M.G. Kanatzidis, Nature **508**, 373 (2014).

[54] T.M. Tritt and M.A. Subramanian, MRS Bull. **31**, 188 (2006).

[55] C.M. Bhandari, in *CRC Handb. Thermoelectr.*, edited by D. Rowe (CRC Press, New York, 1995), pp. 1–11.

[56] C. Wood, Rep. Prog. Phys. **51**, 459 (1988).

[57] C.B. Vining and J.P. Fleurial, in *X Int. Confr. Thermoelectr.* (USA, 1991), pp. 1–14.

[58] M. Zebarjadi, K. Esfarjani, A. Shakouri, J.H. Bahk, Z. Bian, G. Zeng, J. Bowers, H. Lu, J. Zide, and A. Gossard, Appl. Phys. Lett. **94**, 202105 (2009).

[59] M.S. Dresselhaus, G. Chen, M.Y. Tang, R.G. Yang, H. Lee, D.Z. Wang, Z.F. Ren, J.P. Fleurial, and P. Gogna, Adv. Mater. **19**, 1043 (2007).

[60] S. V Faleev and F. Léonard, Phys. Rev. B **77**, 214304 (2008).

[61] C. Sturm, P. Jafarzadeh, and H. Kleinke, in *Compr. Nanosci. Nanotechnol.*, edited by D.L. Andrews, R.H. Lipson, and T. Nann, second ed. (Elsevier B.V, 2019), pp. 349–358.

[62] K. Hsu, S. Loo, F. Guo, W. Chen, J. Dyck, C. Uher, T. Hogan, E. Polychroniadis, and M.G. Kanatzidis, Science **303**, 818 (2004).

[63] Y.H. Oh and T.S. Yeo, Mater. Res. Bull. **58**, 54 (2014).

[64] R. Venkatasubramanian, E. Slivola, T. Colpitts, and B. O'Quinn, Nature **413**, 597 (2001).

[65] W. Xie, J. He, H.J. Kang, X. Tang, S. Zhu, M. Laver, S. Wang, J.R.D. Copley, C.M. Brown, Q. Zhang, and T.M. Tritt, Nano Lett. **10**, 3283 (2010).

[66] W.C. Pilgrim and C. Morkel, J. Phys. Condens. Matter **18**, R585 (2006).

[67] K. Trachenko, Phys. Rev. B **78**, 104021 (2008).

[68] Y. He, T. Day, T. Zhang, H. Liu, X. Shi, L. Chen, and G.J. Snyder, Adv. Mater. **26**, 3974 (2014).

[69] K. Zhao, A.B. Blichfeld, E. Eikeland, P. Qiu, D. Ren, B.B. Iversen, X. Shi, and L. Chen, J. Mater. Chem. A **5**, 18148 (2017).

[70] K. Zhao, A.B. Blichfeld, H. Chen, Q. Song, T. Zhang, C. Zhu, D. Ren, R. Hanus, P. Qiu, B.B. Iversen, F. Xu, G.J. Snyder, X. Shi, and L. Chen, Chem. Mater. **29**, 6367 (2017).

[71] S. Ballikaya, H. Chi, J.R. Salvador, and C. Uher, J. Mater. Chem. A **1**, 12478 (2013).

[72] Y. He, P. Lu, X. Shi, F. Xu, T. Zhang, G.J. Snyder, C. Uher, and L. Chen, Adv. Mater. **27**, 3639 (2015).

[73] B. Gahtori, S. Bathula, K. Tyagi, M. Jayasimhadri, A.K. Srivastava, S. Singh, R.C. Budhani, and A. Dhar, Nano Energy **13**, 36 (2015).

[74] S. Bhattacharya, R. Basu, R. Bhatt, S. Pitale, A. Singh, D.K. Aswal, S.K. Gupta, M. Navaneethan, and Y. Hayakawa, J. Mater. Chem. A **1**, 11289 (2013).

[75] S. Bhattacharya, A. Bohra, R. Basu, R. Bhatt, S. Ahmad, K.N. Meshram, A.K. Debnath, A. Singh, S.K. Sarkar, M. Navneethan, Y. Hayakawa, D.K. Aswal, and S.K. Gupta, J. Mater. Chem. A **2**, 17122 (2014).

[76] P. Qiu, T. Zhang, Y. Qiu, X. Shi, and L. Chen, Energy Environ. Sci. **7**, 4000 (2014).

[77] B. Jiang, P. Qiu, E. Eikeland, H. Chen, Q. Song, D. Ren, T. Zhang, J. Yang, B.B. Iversen, X. Shi,

and L. Chen, J. Mater. Chem. C **5**, 943 (2017).

[78] D.R. Brown, T. Day, T. Caillat, and G.J. Snyder, J. Electron. Mater. **42**, 2014 (2013).

[79] L. Zhao, X. Wang, F.Y. Fei, J. Wang, Z. Cheng, S. Dou, J. Wang, and G.J. Snyder, J. Mater. Chem. A **3**, 9432 (2015).

[80] F. Baumer and T. Nilges, Z. Anorg. Allg. Chem. **644**, 1519 (2018).

[81] A.A. Olvera, N.A. Moroz, P. Sahoo, P. Ren, T.P. Bailey, A.A. Page, C. Uher, and P.F.P. Poudeu, Energy Environ. Sci. **10**, 1668 (2017).

[82] T.P. Bailey, S. Hui, H. Xie, A. Olvera, P.F.P. Poudeu, X. Tang, and C. Uher, J. Mater. Chem. A **4**, 17225 (2016).

[83] H.J. Goldsmid, *Introduction to Thermoelectricity* (Springer-Verlag, Berlin, 2010).

[84] M.K. Balapanov, I.B. Zinnurov, and U.K. Mukhamed'yanov, Russ. J. Electrochem. **43**, 585 (2007).

[85] S.D. Kang, J.-H. Pöhls, U. Aydemir, P. Qiu, C.C. Stoumpos, R. Hanus, M.A. White, X. Shi, L. Chen, M.G. Kanatzidis, and G.J. Snyder, Mater. Today Phys **1**, 7 (2017).

[86] P. Qiu, X. Shi, and L. Chen, Energy Storage Mater. **3**, 85 (2016).

[87] P. Qiu, M.T. Agne, Y. Liu, Y. Zhu, H. Chen, T. Mao, J. Yang, W. Zhang, S.M. Haile, W.G. Zeier, J. Janek, C. Uher, X. Shi, L. Chen, and G.J. Snyder, Nat. Commun. **9**, 4 (2018).

[88] K. Kurosaki, H. Uneda, H. Muta, and S. Yamanaka, J. Alloys Compd. **385**, 312 (2004).

[89] K. Kurosaki, H. Uneda, H. Muta, and S. Yamanaka, J. Appl. Phys. **97**, 053705/1 (2005).

[90] M.A. McGuire, A.F. May, D.J. Singh, M.H. Du, and G.E. Jellison, J Solid State Chem. **184**, 2744 (2011).

[91] J. Li, L.-D. Zhao, J. Sui, D. Berardan, W. Cai, and N. Dragoe, Dalt. Trans. **44**, 2285 (2015).

[92] Y.C. Wang and F.J. DiSalvo, J Solid State Chem. **156**, 44 (2001).

[93] C. Yang, K. Guo, X. Yang, J. Xing, K. Wang, J. Luo, and J.T. Zhao, ACS Appl. Energy Mater. **2**, 889 (2019).

[94] A. Assoud, S. Thomas, B. Sutherland, H. Zhang, T.M. Tritt, and H. Kleinke, Chem. Mater. **18**, 3866 (2006).

[95] Y. Cui, A. Assoud, J. Xu, and H. Kleinke, Inorg. Chem. **46**, 1215 (2007).

[96] O. Mayasree, Y. Cui, A. Assoud, and H. Kleinke, Inorg. Chem. **49**, 6518 (2010).

[97] O. Mayasree, C.R. Sankar, A. Assoud, and H. Kleinke, Inorg. Chem. **50**, 4580 (2011).

[98] O. Mayasree, C.R. Sankar, Y. Cui, A. Assoud, and H. Kleinke, Eur. J. Inorg. Chem. **2011**, 4037 (2011).

[99] B. Kuropatwa, Y. Cui, A. Assoud, and H. Kleinke, Chem. Mater. **21**, 88 (2009).

[100] B.A. Kuropatwa, A. Assoud, and H. Kleinke, Inorg. Chem. **51**, 5299 (2012).

[101] B.A. Kuropatwa, A. Assoud, and H. Kleinke, Inorg. Chem. **50**, 7831 (2011).

[102] X. Su, F. Fu, Y. Yan, G. Zheng, T. Liang, Q. Zhang, X. Cheng, D. Yang, H. Chi, X. Tang, Q. Zhang, and C. Uher, Nat. Commun. **5**, 4908 (2014).

[103] S. Ballikaya, H. Chi, J.R. Salvador, and C. Uher, J. Mater. Chem. A **1**, 12478 (2013).

[104] K. Zhao, P. Qiu, Q. Song, A.B. Blichfeld, E. Eikeland, D. Ren, B. Ge, B.B. Iversen, X. Shi, and L. Chen, Mater. Today Phys. **1**, 14 (2017).

[105] T. Plirdpring, K. Kurosaki, A. Kosuga, T. Day, S. Firdosy, V. Ravi, G.J. Snyder, A. Harnwunggmoung, T. Sugahara, Y. Ohishi, H. Muta, and S. Yamanaka, Adv. Mater. **24**, 3622 (2012).

[106] R. Liu, L. Xi, H. Liu, X. Shi, W. Zhang, and L. Chen, Chem. Commun. **48**, 3818 (2012).

[107] S.O.J. Long, A. V Powell, P. Vaqueiro, and S. Hull, Chem. Mater. **30**, 456 (2018).

[108] A.J. Hong, L. Li, H.X. Zhu, X.H. Zhou, Q.Y. He, W.S. Liu, Z.B. Yan, J.M. Liu, and Z.F. Ren, Solid State Ionics **261**, 21 (2014).

[109] M. Oudah, K.M. Kleinke, and H. Kleinke, Inorg. Chem. **54**, 845 (2015).

[110] X. Shi, L. Xi, J. Fan, W. Zhang, and L. Chen, Chem. Mater. **22**, 6029 (2010).

[111] Y. Liu, G. García, S. Ortega, D. Cadavid, P. Palacios, J. Lu, M. Ibáñez, L. Xi, J. De Roo, A.M. López, S. Martí-Sánchez, I. Cabezas, M. de la Mata, Z. Luo, C. Dun, O. Dobrozhan, D.L. Carroll, W. Zhang, J. Martins, M. V Kovalenko, J. Arbiol, G. Noriega, J. Song, P. Wahnón, and A. Cabot, J. Mater. Chem. A **5**, 2592 (2017).

[112] J. Heo, G. Laurita, S. Muir, M.A. Subramanian, and D.A. Keszler, Chem. Mater. **26**, 2047 (2014).

[113] Y. Bouyrie, M. Ohta, K. Suekuni, Y. Kikuchi, P. Jood, A. Yamamoto, and T. Takabatake, J. Mater. Chem. C **5**, 4174 (2017).

[114] D. Li, X.Y. Qin, T.H. Zou, J. Zhang, B.J. Ren, C.J. Song, Y.F. Liu, L. Wang, H.X. Xin, and J.C. Li, J. Alloys Compd. **635**, 87 (2015).

[115] E. Quarez, K. Hsu, R. Pcionek, N. Frangis, E.K. Polychroniadis, and M.G. Kanatzidis, J. Am. Chem. Soc. **127**, 9177 (2005).

[116] J. Davidow and Y. Gelbstein, J. Electron. Mater. **42**, 1542 (2013).

[117] L.-D. Zhao, J. He, C.-I. Wu, T.P. Hogan, X. Zhou, C. Uher, V.P. Dravid, and M.G. Kanatzidis, J. Am. Chem. Soc **134**, 7902 (2012).

[118] K. Biswas, J. He, I.D. Blum, C.-I. Wu, T.P. Hogan, D.N. Seidman, V.P. Dravid, and M.G. Kanatzidis, Nature **489**, 414 (2012).

[119] B. Wölfing, C. Kloc, J. Teubner, and E. Bucher, Phys. Rev. Lett. **86**, 4350 (2001).

[120] Q. Guo, M. Chan, B.A. Kuropatwa, and H. Kleinke, Chem.Mater **25**, 4097 (2013).

[121] Q. Guo, A. Assoud, and H. Kleinke, Adv. Energy Mater. **4**, 1400348/1 (2014).

[122] Y. Shi, A. Assoud, S. Ponou, S. Lidin, and H. Kleinke, J. Am. Chem. Soc. **140**, 8578 (2018).

[123] J.P. Heremans, V. Jovovic, E.S. Toberer, A. Saramat, K. Kurosaki, A. Charoenphakdee, S. Yamanaka, and G.J. Snyder, Science **321**, 554 (2008).

[124] K. Kurosaki, A. Kosuga, H. Muta, M. Uno, and S. Yamanaka, Appl. Phys. Lett. **87**, 061919 (2005).

[125] X. Shi, J. Yang, S. Bai, J. Yang, H. Wang, M. Chi, J.R. Salvador, W. Zhang, L. Chen, and W. Wong-Ng, Adv. Funct. Mater. **20**, 755 (2010).

[126] E.S. Toberer, C.A. Cox, S.R. Brown, T. Ikeda, A.F. May, S.M. Kauzlarich, and G.J. Snyder, Adv. Funct. Mater. **18**, 2795 (2008).

[127] L. Zhao, J. He, D. Berardan, Y. Lin, J. Li, C.-W. Nan, and N. Dragoe, Energy Environ. Sci. **7**, 2900 (2014).

[128] J. Sui, J. Li, J. He, Y.-L. Pei, D. Berardan, H. Wu, N. Dragoe, W. Cai, and L.-D. Zhao, Energy Environ. Sci. **6**, 2916 (2013).

[129] G.H. Stout and L.H. Jensen, *X-Ray Structure Determination*, 2nd ed. (Wiley & Sons, New York, 1989).

[130] W. FRIEDRICH, P. KNIPPING, and M. von LAUE, *Sitz. Math.-Phys. Klasse Bayer Akad. Wiss* (München, 1912).

[131] W.L. Bragg, Proc. Cambridge Phil. Soc. **17**, 43 (1913).

[132] W.L. Bragg, Proc. Roy. Soc. London **88**, 43 (1913).

[133]*M86-Exx078 APEX2 User Manual* (Bruker AXS Inc., Madison, WI, 2006).

[134] G.M. Sheldrick, Acta Crystallogr. A **64**, 112 (2008).

[135] A.L. Spek, Acta Cryst. **D65**, 148 (2009).

[136] W. Zhou, R.P. Apkarian, Z.L. Wang, and D. Joy, in *Scanning Microsc. Nanotechnol. Tech. Appl.*, edited by W. Zhou and Z.L. Wang (Springer New York, New York, 2007), pp. 1–40.

[137] O. Guillon, J. Gonzalez-Julian, B. Dargatz, T. Kessel, G. Schierning, J. Räthel, and M. Herrmann, Adv. Eng. Mater. **16**, 830 (2014).

[138] H. Wang, W.D. Porter, H. Böttner, J. König, L. Chen, S. Bai, T.M. Tritt, A. Mayolet, J. Senawiratne, C. Smith, F. Harris, P. Gilbert, J. Sharp, J. Lo, H. Kleinke, and L. Kiss, J. Electron. Mater. **42**, 1073 (2013).

[139] T.M. Tritt and D. Weston, in *Therm. Conduct. Theory, Prop. Appl.*, edited by T.M. Tritt (Springer Science & Business Media, 2004), p. 197.

[140] F.I. Chu, R.E. Taylor, and A.B. Donaldson, J. Appl. Phys. **51**, 336 (1980).

[141] W.J. Parker, R.J. Jenkins, C.P. Butler, and G.L. Abbott, J. Appl. Phys. **32**, 1679 (1961).

[142] H. Wang, W.D. Porter, H. Böttner, J. König, L. Chen, S. Bai, T.M. Tritt, A. Mayolet, J. Senawiratne, C. Smith, F. Harris, P. Gilbert, J.W. Sharp, J. Lo, H. Kleinke, and L. Kiss, J. Electron. Mater. **42**, 654 (2013).

[143] J. De Boor, C. Stiewe, P. Ziolkowski, T. Dasgupta, G. Karpinski, E. Lenz, F. Edler, and E. Müller, J. Electron. Mater. **42**, 1711 (2013).

[144] E.H. Hall, Am. J. Math. **2**, (1879).

[145] A.C. Beer, Solid-State Electron. **9**, 339 (1966).

[146] Netzsch Group, *STA 409 PC Luxx User Manual* (Selb, Germany, 1998).

[147] P. Jafarzadeh, A. Assoud, D. Ramirez, N. Farahi, T. Zou, E. Müller, J.B. Kycia, and H. Kleinke, J. Appl. Phys. **126**, 025109/1 (2019).

[148] D. Platzek, G. Karpinski, C. Stiewe, P. Ziolkowski, C. Drasar, and E. Müller, in *ICT 2005. 24th Int. Conf. Thermoelectr. 2005.* (IEEE, 2005), pp. 13–16.

[149] K.M. Merz and R. Hoffmann, Inorg. Chem. **27**, 2120 (1988).

[150] P.K. Mehrotra and R. Hoffmann, Inorg. Chem. **17**, 2187 (1978).

[151] Y. Shi, A. Assoud, C.R. Sankar, and H. Kleinke, Chem. Mater. **29**, 9565 (2017).

[152] Y. Shi, A. Assoud, S. Ponou, S. Lidin, and H. Kleinke, J. Am. Chem. Soc. **140**, 8578 (2018).

[153] G.S. Nolas, D.T. Morelli, and T.M. Tritt, Annu. Rev. Mat. Sci. **29**, 89 (1999).

[154] E. Chalfin, H. Lu, and R. Dieckmann, Solid State Ionics **178**, 447 (2007).

[155] J. Capps, F. Drymiotis, S. Lindsey, and T.M. Tritt, Philos. Mag. Lett. **90**, 677 (2010).

[156] H.-S. Kim, Z.M. Gibbs, Y. Tang, H. Wang, and G.J. Snyder, APL Mater. **3**, 041506/1 (2015).

[157] B.A. Kuropatwa, A. Assoud, and H. Kleinke, Inorg. Chem. **50**, 7831 (2011).

[158] P. Jafarzadeh, M. Oudah, A. Assoud, N. Farahi, E. Müller, and H. Kleinke, J. Mater. Chem. C **6**, 13043 (2018).

[159] W. Liu, X. Tan, K. Yin, H. Liu, X. Tang, J. Shi, Q. Zhang, and C. Uher, Phys. Rev. Lett. **108**, 1 (2012).

[160] N. Farahi, S. Prabhudev, G.A. Botton, J.R. Salvador, and H. Kleinke, ACS Appl. Mater. Interfaces **8**, 34431 (2016).

[161] P. Jafarzadeh, M.R. Rodrigues, Y. Shi, A. Assoud, T. Zou, J.B. Kycia, and H. Kleinke, Dalt. Trans. **48**, 9357 (2019).

[162] X. Zhang, Y. Park, T. Hogan, J.L. Schindler, C.R. Kannewurf, S. Seong, T. Albright, and M.G. Kanatzidis, J. Am. Chem. Soc. **117**, 10300 (1995).

[163] T.-R. Wei, Y. Qin, T. Deng, Q. Song, B. Jiang, R. Liu, P. Qiu, X. Shi, and L. Chen, Sci. China Mater. **62**, 8 (2019).

[164] T. Willhammar, K. Sentosun, S. Mourdikoudis, B. Goris, M. Kurttepeli, M. Bercx, D. Lamoen, B. Partoens, I. Pastoriza-Santos, J. Pérez-Juste, L.M. Liz-Márzan, S. Bals, and G. Van Tendeloo, Nat. Commun. **8**, 14925 (2017).

[165] K.D. Machado, J.C. de Lima, T.A. Grandi, C.E.M. Campos, C.E. Maurmann, A.A.M. Gasperini, S.M. Souza, and A.F. Pimenta, Acta Crystallogr. Sect. B Struct. Crystallogr. Cryst. Chem. **60**, 282 (2004).

[166] R. Blachnik, L. M, and U. Walbrecht, J. Solid State Chem. **48**, 431 (1983).

[167] S.M.K.N. Islam, M. Li, U. Aydemir, X. Shi, L. Chen, G.J. Snyder, and X. Wang, J. Mater. Chem. A **6**, 18409 (2018).

# Permissions

"Reproduced from [Parisa Jafarzadeh, Abdeljalil Assoud, Daniel Ramirez, Nader Farahi, Tianze Zou, Eckhard Müller, Jan B. Kycia, Holger Kleinke, Thermoelectric Properties and Stability of $Ba_3Cu_{16-x}Se_{11-y}Te_y$, J. Appl. Phys. 126, 025109/1 - 9 (2019)], with the permission of AIP Publishing").

[Parisa Jafarzadeh, Mohamed Oudah, Abdeljalil Assoud, Nader Farahi, Eckhard Müller and Holger Kleinke, High thermoelectric performance of $Ba_3Cu_{16-x}(S,Te)_{11}$, J. Mater. Chem. C, 6, 13043 – 13048 (2018)] - Reproduced by permission of The Royal Society of Chemistry.

[Parisa Jafarzadeh, Maegan R. Rodrigues, Yixuan Shi, Abdeljalil Assoud, Tianze Zou, Jan B. Kycia and Holger Kleinke, Effect of mixed occupancies on the thermoelectric properties of $BaCu_{6-x}Se_{1-y}Te_{6+y}$ polychalcogenides, Dalton Trans. 48, 9357 – 9364 (2019)] - Reproduced by permission of The Royal Society of Chemistry.

| | |
|---|---|
| Licensed Content Publisher | Elsevier |
| Licensed Content Publication | Elsevier Books |
| Licensed Content Title | Comprehensive Nanoscience and Nanotechnology |
| Licensed Content Author | Cheryl Sturm,Parisa Jafarzadeh,Holger Kleinke |
| Licensed Content Date | Jan 1, 2019 |
| Licensed Content Pages | 10 |
| Type of Use | reuse in a thesis/dissertation |
| Portion | figures/tables/illustrations |
| Number of figures/tables/illustrations | 1 |
| Format | both print and electronic |
| Are you the author of this Elsevier chapter? | Yes |
| Will you be translating? | No |
| Original figure numbers | Figure 2 |
| Title of your thesis/dissertation | Thermoelectric Properties and Stability of Copper Chalcogenides |
| Expected completion date | Sep 2019 |
| Estimated size (number of pages) | 120 |
| Requestor Location | |
| Publisher Tax ID | GB 494 6272 12 |
| Total | 0.00 CAD |



Permission from ref.[61] for Figure 1.6.

Copyright 2019 Elsevier.


Permission from ref.[109] for Figures 5.4, 5.5, 5.9, and 5.11. Copyright 2019 American Chemical Society.

printable details

| | |
|---|---|
| License Number | 4625020369577 |
| License date | Jul 09, 2019 |
| Licensed Content Publisher | Springer Nature |
| Licensed Content Publication | Nature Materials |
| Licensed Content Title | Copper ion liquid-like thermoelectrics |
| Licensed Content Author | Huili Liu, Xun Shi, Fangfang Xu, Linlin Zhang, Wenqing Zhang et al. |
| Licensed Content Date | Mar 11, 2012 |
| Licensed Content Volume | 11 |
| Licensed Content Issue | 5 |
| Type of Use | Thesis/Dissertation |
| Requestor type | academic/university or research institute |
| Format | print and electronic |
| Portion | figures/tables/illustrations |
| Number of figures/tables/illustrations | 1 |
| High-res required | no |
| Will you be translating? | no |
| Circulation/distribution | <501 |
| Author of this Springer Nature content | no |
| Title | Thermoelectric Properties and Stability of barium Copper Chalcogenides |
| Institution name | n/a |
| Expected presentation date | Sep 2019 |
| Portions | Figure 2 |
| Requestor Location | |
| Total | 0.00 USD |

ORDER MORE CLOSE WINDOW

Copyright © 2019 Copyright Clearance Center, Inc. All Rights Reserved. Privacy statement. Terms and Conditions.
Comments? We would like to hear from you. E-mail us at customercare@copyright.com

Permission from ref.[27] for Figure 6.1.

Copyright 2019 Springer Nature.